Development of Nanomaterials for High-Performance energy storage technology

A thesis presented for the award of degree of

Doctor of Philosophy

from

University of Technology, Sydney

By

Tianyi Wang, B. Sc.

June 2021

CERTIFICATE OF ORIGINAL AUTHORSHIP

I, Tianyi Wang, certify that the work presented in this thesis has not been previously submitted for a degree nor has been submitted as a part of requirements for a degree except as fully acknowledged within the text.

I also certify that the thesis has been written by me. Any help that I have received in my research work and the preparation of the thesis itself has been acknowledged. In addition, I certify that all information sources and literature used are indicated in the thesis.

This research is supported by an Australian Government Research Training Program.

Tianyi Wang

Production Note:
Signature removed prior to publication.

Sydney, Australia

June 2021

DEDICATION

This thesis is dedicated to my family. Thank you for all of your love and support.

ACKNOWLEDGEMENTS

Firstly, I am grateful to my supervisor, Professor Guoxiu Wang, for his kind and continuous support and invaluable advice throughout my Ph.D. study. I would also like to thank Prof. Andrew McDonagh and Dr. Bing Sun for their valuable guidance during my Ph.D. study.

I would like to acknowledge Dr. Jane Yao. Her kind help and support is essential to my laboratory work.

Special thanks are given to my colleagues at UTS. Dr. Jinqiang Zhang, Dr. Xin Guo, Dr. Dawei Su, Dr. Dong Zhou, Dr. Hao Tian, Dr. Xiaochun Gao, Dr. Kang Yan, Dr. Yi Chen, Dr. Xiao Tang. Their kind collaboration and assistance were helpful. Also, I want to thank my friends in Yangzhou University, Miss. Xiaoyun Sun, Mr. Jian Yang, Miss. Lu Yu, Prof. Huaiguo Xue and Prof. Jie Han. They gave me much support during the COVID-19 pandemic and my most difficult time during the Ph.D. study.

In addition, I appreciate the administrative and technical support I received from Dr. Ronald Shimmon, Dr. Linda Xiao. I would also like to thank Prof. Yi Cui and Dr. Yanbin Li at Stanford University, USA.

The final support from UTS scholarship and RMCRC project 2017 to help me finish my Ph.D. study are highly appreciated.

Last but not the least, I would like to thank my parents for supporting me spiritually throughout writing this thesis and my life in general.

Tianyi Wang

June 2021

REPSEARCH PUBLICATIONS

1. **Tianyi Wang**, Xiaoyu Sun, Xin Guo, Jinqiang Zhang, Jian Yang, Shouxuan Tao, Jun Guan, Lin Zhou, Jie Han, Chengyin Wang, Hang Yao and Guoxiu Wang, Ultraefficiently Calming Cytokine Storm Using $Ti_3C_2T_x$, ***Small methods***, 2020, DOI: 10.1002/smtd.202001108.
2. **Tianyi Wang**, Yanbin Li, Jinqiang Zhang, Kang Yan, Pauline Jaumaux, Jian Yang, Chengyin Wang, Devaraj Shanmukaraj, Bing Sun, Michel Armand, Yi Cui, Guoxiu Wang, Immunizing lithium metal anodes against dendrite growth using protein molecules to achieve high energy batteries. ***Nature Communications***, 2020, 1, 5429.
3. **Tianyi Wang**, Dawei Su, Yi Chen, Kang Yan, Lu Yu, Lin Liu, Yunhao Zhong, Peter H.L. Notten, Chengyin Wang, Guoxiu Wang, Biomimetic 3D Fe/CeO_2 decorated N-doped carbon nanotubes architectures for high performance lithium sulfur batteries. ***Chemical Engineering Journal***, 2020, 401, 126079.
4. **Tianyi Wang**, Yushu Liu, Dawei Su, Guoxiu Wang, 1D and 2D Flexible Carbon Matrix Materials for Lithium-Sulfur Batteries. ***Nanocarbon Electrochemistry***, 2020, 145-179.
5. **Tianyi Wang**, Dawei Su, Devaraj Shanmukaraj, Teoflo Rojo, Michel Armand, Guoxiu Wang, Electrode materials for sodium-ion batteries: considerations on crystal structures and sodium storage mechanisms. ***Electrochemical Energy Reviews***, 2018, 1, 200-237.
6. **Tianyi Wang**, Katja Kretschmer, Sinho Choi, Huan Pang, Huaiguo Xue, Guoxiu Wang, Fabrication methods of porous carbon materials and separator membranes for lithium-sulfur batteries: development and future perspectives. ***Small methods***, 2017, 1, 1700089.
7. Huajun Tian, **Tianyi Wang**, Fan Zhang, Shuoqing Zhao, Steven Wan, Fengrong He, Guoxiu Wang, Tunable porous carbon spheres for high-performance rechargeable batteries. ***Journal of Materials***

Chemistry A, 2018, 6, 12816-12814.

8. Jian Yang, Jiabao Li, **Tianyi Wang**, Peter H.L. Notten, Hao Ma, Zhigang Liu, Chengyin Wang, Guoxiu Wang, Novel hybrid of amorphous Sb/N-doped layered carbon for high-performance sodium-ion batteries. ***Chemical Engineering Journal***, 2020, 127169.
9. Kang Yan, Shuoqing Zhao, Jinqiang Zhang, Javad Safaei, Xingxing Yu, **Tianyi Wang**, Shijian Wang, Bing Sun, Guoxiu Wang, Dendrite-Free Sodium metal batteries Enabled by the release of Contact Strain on Flexible and Sodiophilic Matrix. NANO Letters, 2020, 20, 6112-6119.
10. Pauline Jaumaux, Qi Liu, Dong Zhou, Xiaofu Xu, **Tianyi Wang**, Yizhou Wang, Feiyu Kang, Baohua Li, Guoxiu Wang, Deep-Eutectic-Solvent-Based Self-Healing Polymer Electrolyte for Safe and Long-Life Lithium-Metal Batteries. Angewandte Chemie International Edition, 2020, 59, 9134-9142.

TABLE OF CONTENTS

CERTIFICATION OF ORIGINAL AUTHORSHIP 2

DEDICATION 3

ACKNOWLEDGEMENTS 4

RESEARCH PUBLICATIONS 5

TBLE OF CONTENTS 7

LIST OF TABLES 10

LIST OF FIGURES 11

ABSTRACT 21

INTRODUCTION 22

Chapter 1 Introduction 22

Chapter 2 Literature Review 25

2.1 The Working Mechanism and Challenges of Li-S batteries 26

2.2 Flexible Cathode Hosts for Lithium-Sulfur Batteries 28

2.3 Electrolyte Membranes for Flexible Li-S Batteries 41

2.3.1 Solid Polymer Electrolyte for Flexible Li-S Batteries 43

2.3.2 Gel Polymer Electrolytes for Flexible Li-S Batteries 46

2.3.3 Composite Polymer Electrolytes for Flexible Li-S batteries 47

2.4 Separator for Flexible Li-S Batteries 51

2.5 Summary 41

Chapter 3 Experimental section 56

3.1 Overview 57

3.2 Material Preparation 60

3.2.1 Co-precipitation experiment 60

3.2.2 High temperature calcination 60

3.2.3 Melt diffusion and sulfur injection experiment 60

3.2.4 Electrospinning experiment 61

3.2.5 Finite element simulation (FES) 62

3.3 Characterization methods 62

3.3.1 X-ray powder diffraction (XRD) 62

3.3.2 X-ray photoelectron spectroscopy (XPS) 63

3.3.3 Fourier-transform infrared spectroscopy (FT-IR) 63

3.3.4 Raman spectroscopy 63

3.3.5 Thermogravimetric Analysis (TGA) 64

3.3.6 Scanning electron microscopy (SEM) 64

3.3.7 Transmission electron microscopy (TEM) 64

3.3.8 Two-photon excitation microscopy (TPEM) 64

3.3.9 Cryogenic transmission electron microscopy (Cryo-EM) 65

3.4 Preparation procedure of electrode and assembly of batteries 65

3.4.1 Preparation of electrodes 65

3.4.2 Battery assembly 66

3.5 Electrochemical performances 66

3.5.1 Cyclic Voltammetry (CV) 66

3.5.2 Galvanostatic Charge-Discharge 66

3.5.3 Electrochemical Impedance Spectroscopy (EIS) 67

Chapter 4 Biomimetic 3D Fe@CeO_2 decorated N-doped Carbon nanotubes architectures for high-performance Lithium-Sulfur batteries 67

4.1 Introduction 70

4.2 Experiment section 70

4.2.1 Synthesis of Fe/CeO_2-CNTs hybrids 70

4.2.2 Synthesis of S/Fe/CeO_2-CNTs hybrids 70

4.2.3 Structural and Physical Characterization 70

4.2.4 XPS characterization 71

4.2.5 Electrochemical Testing 71

4.3 Results and discussion 73

Chapter 5 Immunizing lithium metal anodes against dendrite growth using protein molecules to

achieve high energy batteries 94

5.1 Introduction 94

5.2 Experiment section 95

5.2.1 Materials 95

5.2.2 Characterization 96

5.2.3 Electrochemical measurements 98

5.2.4 Cryogenic TEM (Cryo-EM) characterization 98

5.2.5 COMSOL^{TM} simulation 99

5.3 Results and discussion 100

5.3.1 Self-defense mechanism of fibroin 100

5.3.2 Dense Li deposition with fibroin 109

5.3.3 Characterization of SEI with fibroin 115

5.3.4 Electrochemical performance of performance of Li anodes with fibroin 119

5.3.5 Electrochemical performance of performance of Li || $Li_4Ti_5O_{12}$ full cells 122

5.4 Conclusion 133

Chapter 6 Conclusion and future perspective 134

APPENDIX NOMENCLETURE 136

REFERENCES 136

LIST OF TABLES

Table 3.1 Chemicals details in the research project. 59

Table 5.1 Comparison of mechanical properties of fibroin interlayer before and after immersed in ether-based electrolyte..... 120

LIST OF FIGURES

Figure 2.1 (a) The fabrication process of the laminated hybrid sulfur cathode and (b) schematic image of structure of the flexible Li–S battery. (c) Comparison to explain the differences in electronic conductivity between aligned CNTs and random CNTs. [25]. Copyright 2015, John Wiley & Sons. (d) The preparation method for the S-rGO paper. (e) The rate capability of 3D–NGS with current densities ranging from 100–1500 mAh g^{-1} and the first discharge–charge profiles at different current densities [20]. Copyright 2014, Royal Society of Chemistry. (f) The preparation method for synthesizing S-CNT/G and (g) its electrochemical performance when used as flexible Li–S battery cathode. [26]. Copyright 2015, Royal Society of Chemistry. 33

Figure 2.2 (a) The preparation process of NPCFs by an electrospinning method. (b) Typical tensile stress–strain curves of the as-prepared membrane and photograph of the tensile stress–strain testing instrument. [28]. Copyright 2017, Royal Society of Chemistry. (c) The preparation process of the CNT–rGO/S composite. (d). The physical performance of CNT–rGO/S. (e) SEM image of sulfur particles and holder materials. [24]. Copyright 2015, American Chemical Society. (f) The sulfur particles that are protected by GTS. (g) The preparation process of the 3DGS hydrogel. [29]. Royal Society of Chemistry. (h) The electrochemical performance of a Li–S battery using 3DGS hydrogel as cathode material at various current densities. [30]. Copyright 2016, Royal Society of Chemistry. 37

Figure 2.3 (a) The flexible porous structure of the material and (c) the discharging capacity at various current densities. [32]. Copyright 2016, Royal Society of Chemistry. (d) Li–S battery with sandwich-structured cathode that can be curved or bent. Source: Song et al. 2014 [25]. Copyright 2014, Royal Society of Chemistry. (e) SEM view of sulfur particles that are attached on carbon foam. (f) The charge

and discharge curve of the battery.[34]. Copyright 2016, Royal Society of Chemistry. (g) The structure of 3DCNT/Graphene-Li_2S aerogel. (h) Electrochemical performance of scaffold material. [35]. Copyright 2016, American Chemical Society. 42

Figure 2.4 (a) Cycling performance of GPE-based batteries, and those of liquid-based ones at 0.1 C. (b) Rate performance of GPE-based batteries and the liquid-based ones from 0.1 to 1 C. (c) The polysulfide immobilization mechanism of GPE-based batteries and the liquid-based ones. Dendrites continually grow on the sulfur electrodes' surface in the liquid electrolyte-based batteries while the GPE-based ones can maintain a smooth morphology.[48]. Copyright 2016, Elsevier B.V. (d) With the increasing weight ratio of sucrose in the sucrose-PEO electrolyte, the ionic conductivity increases obviously. (e) Cycling performance of Li–S batteries with sucrose-PEO electrolyte and the electrochemical impedance spectroscopy (EIS) spectrum of the battery. (f) Specific capacity of cells using the sucrose-PEO electrolyte. The value remained almost constant after 200 cycles.[10]. Copyright 2017, Electrochemical Society..... 45

Figure 2.5 (a) 50PEO–50SiO_2 composite electrolyte membranes, that were flexible enough to be rolled into a tube. (b) Capacity retention of Li–S battery with (1) common liquid electrolyte and (2) the 50PEO–50SiO_2-based electrolyte.[54]. Copyright 2013, Electrochemical Society. (c) Preparation and mechanism of the flexible halloysite nano-clay electrolyte. Cast and dried after HNF, LiTFSI, and PEO were mixed to obtain a thin film and the ordered 3D channels promoted ionic conduction. (d) Photos of initial and final tension state of the halloysite nanoclay electrolyte film. (e) Discharge and charge curves of a battery with halloysite nano-clay electrolyte at 25 C. (f) Cycling performance of a battery with the halloysite nanoclay electrolyte at 25 C.[55]. Copyright 2017, Elsevier B.V. (g) Stress–strain of

GPE assisted by ETU. (h) Charge and discharge stability test of a battery with ETU-assisted GPE.[56]. Copyright 2017, Elsevier B.V. 48

Figure 2.6 (a) SEM images of electrodes with PETEA (3 right) and liquid (3 left) electrolytes' surface after 2 and 50 charge and discharge cycles. (b) The PETEA-based GPE under serious deformation could power a light-emitting diode (LED) lamp while the liquid one could not. Compared with liquid electrolyte, PETEA-based GPE could maintain its stability when bent and had the same specific capacity as before when returned to a flat shape. Source: Liu et al. 2016 [48]. Copyright 2016, Elsevier B.V. (c) How the charge capacity of TiO_2–SiO_2-modified CPE depends on the number of cycles. (d) SEM images of the porous structure of TiO_2–SiO_2-modified CPE. [61]. Copyright 2015, Springer Nature. 51

Figure 2.7 (a) Schematic of electrode configuration illustrating the process of combining sulfur and graphene@PP membrane to form an integrated electrode–separator structure. (b) Cross-section SEM image of sulfur electrode and corresponding EDS spectrum. (c) Stability of electrode–separator combination in terms of conductivity after 5000 bending cycles. (d) Rate performance of the S-G@PP separator, G- + PP separator and Al foil-S + PP separator batteries at different current densities. [74]. Copyright 2015, Wiley. (e) Cross section of MoS_2-Celgard layer. (f) Schematic Li–S battery configuration of MoS_2 Celgard™ separator. (g) The cycling performance for Celgard™, GO/Celgard™, and MoS_2/Celgard™ separators at 0.5 C. [31]. Copyright 2017, Wiley. 54

Figure 2.8 (a) The porous structure of a graphene-modified separator [75]. (b) The flexibility of a Li–S battery using the separator and metal Li as anode material. (c) The flexibility of the separator. (d) Schematic diagram of a modified Celgard™ separator restricting the polysulfide migration while

maintaining good lithium ion transportation. (d) Comparison of hydrophilic separator (before and after modification).[76]. Copyright 2015, Royal Society of Chemistry. (g, h) The structure of the modified membrane [10]. (i) The schematic diagram of the experimental battery.[77]. Copyright 2015, Elsevier B. V. 57

Figure 3.1 The diagram that demonstrates procedures of the experiment. 59

Figure 4.1. **(a)** Illustration of the synthesis process for preparing Fe/CeO_2-CNTs hybrids. (**b)** SEM images of precursor Prussian blue analog nanosheets. (**c)** SEM images of the typical Fe/CeO_2-CNTs structure after annealing at 900 ºC. 74

Figure 4.2 SEM images of $Ce[Fe(CN)_6]$ precursor nanoplates before calcination. 75

Figure 4.3 The pattern of X-ray diffraction data of Fe/CeO_2-CNTs hybrids... 76

Figure 4.4 Comparison of 3D Fe/CeO_2-CNTs hollow structures by changing the ratio of PBA to melamine. (a & b) Seaweed-like, (d & e) sea anemone-like, (g & h) sea cucumber-like and j & k rocky seabed-like Fe/CeO_2-CNTs, corresponding to different ratios of PBA : melamine (3 : 1, 2 : 1, 1 : 1 and 1 : 2). 78

Figure 4.5 Comparison of 3D morphologies of Fe/CeO_2-CNT hybrids calcinated at various temperature: (a) 850 ºC, (b) 900 ºC and (c) 950 ºC. 80

Figure 4.6 (a) HR-TEM image of Fe/CeO_2-CNTs and the specific feature of its catalyst particle. (b) HR-TEM image of one CNT growing by two different growth schemes. (c) A cluster of sea anemone-like CNTs catalyst particles of which have been marked in red color. (d) The TEM image of one sea anemone-like Fe/CeO_2-CNTs. 80

Figure 4.7 (a) The HR-EM image of Fe/CeO_2-CNT and the specific feature of its catalyst particle. b

HR-TEM image of conjunction between catalyst and carbon nanotube. (c) One TEM image of a hollow CNT (PBA : melamine is 2 : 1). (d) A broken CNT (PBA : melamine is 1 : 1) (yellow) of which its catalyst is exposed (red). (e) The inset is the schematic diagram of CNT growth. 81

Figure 4.8 (a) Comparison of Raman spectra of Fe/CeO_2-CNTs synthesized with different proportion of melamine. (b) XPS N1s spectrum of Fe/CeO_2-CNTs. (c) C 1s XPS spectrum of Fe/CeO_2-CNTs. (d) XRD patterns of Fe/CeO_2-CNTs, Sulfur and S/Fe/CeO_2-CNT. 82

Figure 4.9 (a) EDS spectrum mapping revealing uniform distribution of (b) Ce, (c) S and (d) Fe elementals. 83

Figure 4.10 TEM images of S contained CNTs. 61

Figure 4.11 (a) The 1^{st}-5^{th} CV curves of S/Fe/CeO_2-CNTs electrode at a scan rate of 0.1 mV s^{-1}. (b) Typical charge and discharge profiles for the 1^{st}, 20^{th}, 60^{th}, and 100^{th} cycles at 0.2 C. (c) Typical charge and discharge profiles of S/Fe/CeO_2-CNTs with different percentages of N-dopant. (d) Rate performance of S/Fe/CeO_2-CNTs hybrids at varied current rates (0.2, 0.5, 1, 2 and 5 C). (e) EIS comparison of Li-S batteries after 10 cycles employing Fe/CeO_2 CNT and traditional CNT as sulfur holder materials. (f) The adsorption experiment of Li_2S_6, Li_2S_6 + CNTs and Li_2S_6 + Fe/CeO_2 CNTs (1 : 1) after 10 min absorption time (H_2O < 0.1 ppm, O_2 < 0.1 ppm). 84

Figure 4.12. TGA curve of S/Fe/CeO_2 CNTs (1 : 1) hybrid. 88

Figure 4.13. (a) Discharge/charge curve of Li-S battery with high sulfur loading at the first, 5^{th}, 10^{th} and 50^{th} cycle at 0.2 C. (b) Cycling stability of high sulfur loading Li-S battery at the current density of 0.2 C. 88

Figure 4.14. Comparison of SEM images of Li metal foils after 15 cycles at the current density of 0.2 C using high sulfur loading S/CNTs (a & b) and (c & d) S/Fe/CeO_2 CNT as cathodes. 89

Figure 4.15 The *ex-situ* XPS of (a) Li, (b) Fe, (c) S and (d) Ce of electrodes discharged down to 1.7 V. (e) Cycling performances of S/Fe/CeO_2-CNTs electrode at 1 C rate. (f) Comparison of stability of batteries using CNT, Fe/CNT and Fe/CeO_2-CNT as cathode sulfur holder and cycled for 500 cycles at the current density fo 1 C. 91

Figure 4.16. The consistency of cycling performances of S/Fe/CeO_2 CNTs (1 : 1) cathodes when cycled at the current density of 1 C. 92

Figure 4.17. *Ex-situ* XPS results of nitrogen of electrode materials after the 100^{th} cycle. 93

Figure 5.1 Schematic diagram of the self-defense mechanism of fibroin. (a) Illustration of the secondary structural transformation of fibroin molecules and the self-defense mechanism of immunizing Li metal anode against Li dendrite growth. ("R" groups are known as side chains of amino acids (-H to Glycine residue, -CH_2OH to Serine residue, and -CH_3 to Alanine residue)). (b, c) CD spectra (b) and ATR-FT-IR spectra (c) of pristine fibroin and recovered fibroin from the cycled cell after 100 cycles. (d) A fluorescent image of fibroin molecule distribution around the edges and protrusions on a Li metal foil under UV-light. The corresponding 2D (e) and 2.5 D (f) simulations of fluorescence intensity. The scale bars on the top in (e) and (f) correspond to the intensity increase from blue to red. Scale bars, (d, e) 100 μm. 105

Figure 5.2 Digital photo of Tyndall effect in ether-based electrolytes with and without fibroin**.**..... 106

Figure 5.3 Tyndall effect of fibroin dispersed electrolyte during Li | Li plating/stripping process.

Tyndall effect can be observed in a transparent Li | Li symmetric cell during plating/stripping process at a current density of 1 mA cm^{-2}, which confirms that fibroin molecules are dispersed homogeneously in the electrolyte during cycling. 107

Figure 5.4 Comparison of FT-IR curves of fibroin before and after immersed in the ether-based electrolyte for 1 month. 108

Figure 5.5 COMSOL™ simulation of the change of electric field distribution around Li buds. (a) before and (b, c) after covered by fibroin molecules with the height ratio of (b) 30% and (c) 100%. 109

Figure 5.6 Characterization of Li deposition in ether-based electrolyte with fibroin additive. (a, b) Top-view (a) and cross-section (b) SEM images of Li metal anodes cycling in the cells with blank (i.e. no fibroin) electrolyte. (c, d) Top-view (c) and cross-section (d) SEM images of Li metal anodes cycling in the cells with fibroin additive in the electrolyte. The insets in (a) and (b) are the corresponding high magnification SEM images. Scale bars, (a-d) 20 μm and inserts in (a, c) 5μm. (e, f) Low-resolution (e) and high-resolution (f) cryo-EM images of Li deposit in the ether-based electrolyte with fibroin. Scale bars, (e) 1 μm and (f) 20 nm. The white line delineates the boundary between metallic Li and SEI. The blue line delineates the boundary between adsorbed fibroin and SEI. The yellow line delineates the boundary between adsorbed fibroin and electrolyte. g, h *In situ* observations of Li deposition behavior in the glass capillaries filled with the blank electrolyte (g) and the electrolyte with fibroin (h) at a current density of 3 mA cm^{-2}. Scale bars, (g, h) 500 μm. 111

Figure 5.7 SEM images of Li metal surface after 100 cycles. (a, b) In the electrolyte with fibroin. (c,

d) In the electrolyte without fibroin. The current density is 1 mA cm^{-2} and the capacity limitation is 1 mAh cm^{-2}. Scale bar, (a, c) 10 μm and (b, d) 2 μm. 112

Figure 5.8 Schematic illustration of the configuration of Li | Li symmetric cells assembled in a homemade glass capillary. 113

Figure 5.9 X-ray photoelectron spectroscopy (XPS) characterization of SEI formed in ether-based electrolyte with and without fibroin. Li deposition was carried out at a current density of 1mA cm^{-2} and a capacity of 1 mAh cm^{-2} on Cu foil for 10 cycles. (a) N1s spectra, (b) C1s spectra, (c) O1s spectra and (d) F1s spectra. 115

Figure 5.10 XPS spectra of pristine fibroin. (a) Survey spectrum. (b) C1*s* spectra. (c) N1*s* spectra. (d) O1*s* spectra. 116

Figure 5.11 XPS spectra of cycled Li metal anode. XPS survey spectra of the SEI after different degrees of etching by Ar-ion sputtering (a) with and (b) without fibroin additive in the ether-based electrolyte. 117

Figure 5.12 In-depth XPS profiles of the SEI formed in ether-based electrolyte without fibroin. Li deposition was carried out at a current density of 1mA cm^{-2} and a capacity of 1 mAh cm^{-2} on Cu foil for 10 cycles. 118

Figure 5.13 In-depth XPS profiles of the SEI formed in ether-based electrolyte with fibroin. Li deposition was carried out at a current density of 1mA cm^{-2} and a capacity of 1 mAh cm^{-2} on Cu foil for 10 cycles. 119

Figure 5.14 Comparison of Coulombic efficiencies of Li | Cu cells using electrolyte containing different concentrations of fibroin. 123

Figure 5.15 Schematic illustration of the synthesis process of fibroin interlayer. (a-d) Schematic illustration of electrospinning system for preparing a non-woven fibroin interlayer. (e) The architecture of Li metal battery using $Li_4Ti_5O_{12}$ (LTO) as cathode, one piece of fibroin interlayer between the Celgard^{TM} separator and Li metal anode. 123

Figure 5.16 Digital photos of fibroin interlayer. (a) A piece of flat fibroin interlayer. (b) A piece of flexible fibroin interlayer wrap around a pencil. 124

Figure 5.17 SEM observation of fibroin interlays. (a) Low magnification and (b) high magnification SEM images of an electrospun fibroin interlayer. The SEM images of the interconnected structure of fibroin interlayers show rich pore structure, contributing to its excellent flexibility and excellent wettability towards electrolyte. Scale bars, 10 μm. 125

Figure 5.18 Stability test of fibroin interlayer in ether-based electrolyte. (a, b) Digital photos of (a) the pristine fibroin interlayer and (b) the fibroin interlayer retrieved from electrolyte after immersed for 3 days. 126

Figure 5.19 The electrochemical performance of Li anode in ether-based electrolyte with or without a fibroin interlayer. (a) Galvanostatic cycling of symmetric Li | Li cells with (blue line) or without (red line) a fibroin interlayer. The current density is fixed at 3 mA cm^{-2} with a plating/stripping capacity of 1 mAh cm^{-2}. Insets: The blow-up of voltage profiles during 0-2 h, 200-202 h, 800-802 h and 1000-1002 h, respectively. The y-axis scale of the insets is shown on the left. (b) Comparison of cycling

performances of Li | Cu half cells with or without a fibroin interlayer between Cu foil and separator. The amount of Li deposited in each cycle is 1 mAh cm^{-2} and the current density is 1 mA cm^{-2}. (c) The corresponding voltage profiles at the 100^{th} cycle of the Li plating/stripping processes on Cu foil with or without a fibroin interlayer. (d) Comparison of the hysteresis of Li plating/stripping for cells with or without interlayers. (e) Long-term cycling stability of the Li || LTO full cells with or without a fibroin interlayer at a current density of 2 C (1C =175 mA g^{-1}). (f) Rate capabilities from 0.2 C to 10 C of the Li | LTO cells with or without fibroin additive in the electrolytes. 127

Figure 5.20 The cycling stability of Li | Li symmetrical cells at a high current density. A current density of 5 mA cm^{-2} and a capacity of 1 mAh cm^{-2} were applied. 128

Figure 5.21 Comparison of the cycling stability of Li | Li symmetrical cells at high capacities. (a) The capacity limitation is 3 mAh cm^{-2} and the current density is 1 mA cm^{-2}. (b) The capacity limitation is 5 mAh cm^{-2} and the current density is 1 mA cm^{-2}. 129

Figure 5.22. Comparison of the cycling performances of Li | Cu half cells. (a, b) The voltage profiles of Li plating/striping on Cu foils at different cycles (a) without and (b) with fibroin interlayer. 130

Figure 5.23 The EIS measurement of Li | Cu half cells at different cycles. (a) without and (b) with the fibroin interlayer at the current density of 1 mA cm^{-2} with the capacity imitation of 1 mAh cm^{-2}. .. 131

Figure 5.24 Cycling performance of Li || LTO full cells. (a, b) Galvanostatic charge/discharge curves of Li || LTO full cells (a) with and (b) without fibroin interlayer. 132

ABSTRACT

Entering the 21st century, with the continuous energy crisis and the aggravation of environmental pollution, energy storage technologies of renewable energy has become the focus of whole human society. Compared with other energy storage systems, lithium-sulfur (Li-S) batteries have been regarded as one of the most promising systems for next-generation rechargeable batteries owing to their high energy density and low cost. However, both cathode and anode materials encounter serious bottleneck defects in practical applications. For cathode materials, the “Shuttle effect” and the loss of cathode active materials caused by volumetric expansion during cycling are often considered as the main reasons for the energy decline of lithium sulfur batteries. For anode materials, the failure to inhibit the growth of lithium dendrite often leads to the internal short circuit of the battery, resulting in the serious thermal runaway of the battery. At the same time, the rapid development of nanotechnology has brought technological breakthroughs to various scientific fields. In this thesis, some latest nanotechnologies which have been systematically applied for largely improving the electrochemical performances of lithium sulfur batteries have been reviewed. Moreover, we rationally designed some strategies to alleviate the negative effects from “Shuttle effects” and suppress the growth of lithium dendrites. The usage of nanotechnologies can effectively enhance discharge capacity, improve cycling stability and increase the safety of high energy density lithium sulfur batteries. This thesis may provide an insight into the development of nanotechnologies for large scale energy storage.

Chapter 1. Introduction

Climate change is a major challenge facing humanity in the 21st century, which is well recognized as being caused by the burning of fossil fuels. This is forcing us to re-evaluate our dependence on fossil fuels and biomass for energy. Fossil fuels (oil, gas and coal) are mainly used for electricity generation and transportation but they are responsible for nearly 60% of global greenhouse gas emissions.[1] The global solution to this challenge is to adopt renewable energy sources such as solar and wind energies. However, renewable energies are intermittent and only generate electricity under favorable weather conditions. This means that power from these renewables must be either used immediately or stored for use on demand. Therefore, renewable energies require better and affordable energy storage technologies. Rechargeable batteries with long service life are a viable technology for large-scale energy storage.

From the 1960s, the emerge of lithium sulfur (Li-S) batteries endows people with a seemingly ideal choice for a better strategy of energy storage. Li-S batteries could deliver a compact energy storage system which was regarded as exceeding the performance of traditional lithium ion batteries due to its higher theoretical energy density and larger theoretical discharge capacity.[2] The scheme of energy storage in Li-S batteries is quite different from that of lithium ion batteries and sodium ion batteries. The energy storage of traditional lithium ion batteries is based on the intercalation of lithium ions into/out of layered electrode structures such as graphite or lithium metal oxide cathodes. Because the amount of lithium ions is limited and the ion storage sites of the layer structures is confined, the theoretical energy storage capacity of lithium ion battery is limited to ~420 Wh kg^{-1}.[3] In contrast, Li-S battery energy is based on metal plating and stripping at the lithium anode side and a conversion reaction on the sulfur side. The non-topotactic nature of these reactions gives lithium anodes and sulfur

cathodes a high theoretical specific capacity of 3860 and 1673 mAh g^{-1}.[4,6]

In addition, the average working voltage of Li-S batteries is 2.15 V, this endows them with an energy density of ~2500 Wh kg^{-1} and ~2800 Wh L^{-1}.[7] Sulfur is an inexpensive material with a rich distribution throughout the world, lower cost for commercial applications and is environmentally benign. However, in the last decades, research on Li-S batteries was rather stagnant, the safety risk and quick capacity decay had bothered the further development of Li-S batteries. Overall, for cathode materials, there are four challenges that are waiting to solve: i) Dissolution of active material. ii) "Shuttle effect" derived from the soluble long-chain polysulfides. iii) large volumetric expansion. Iv) low conductivity of sulfur. Meanwhile, challenges limiting anode materials of Li-S batteries can be classified into three categories: i) the growth of lithium dendrites. ii) instability of solid electrolyte interphase (SEI) layer and iii) infinite volumetric change of Li metal.[8]

This thesis mainly focuses on the development of nanotechnologies for next generation high performance Li-S batteries (including designing new sulfur storage materials for cathodes and dendrites suppressing strategies for Li metal anodes). Contents of chapters in this doctoral work are outlined as followed:

Chapter 2: Literature review. This chapter reviews the latest development of Li-S batteries, including the 1D and 2D flexible carbon matrix materials for Li-S batteries. We mainly discussed the influence of some new nano materials on the electrochemical performance of Li-S batteries, investigated effects of morphologies on the inhibition of the "Shuttle effect" during cycling. At the last, we compared their disadvantages/advantages of each kind of morphologies corresponding to their electrochemical performances.

Chapter 3: This chapter covers the material preparation, characterization and investigations on electrochemical performances. Particularly, manipulation on morphologies of Li-S battery cathode materials and preparing methods for protection layer on Li metal anodes. The morphologies of the as-prepared nanomaterials were characterized by field emission scanning electron microscopy (FR-SEM), Cryo-transmission electron microscopy (Cryo-EM), transmission electron microscopy (TEM), laser confocal fluorescence microscope (LCFM). The chemical composition, lattice structure and phases of the materials were investigated by X-ray diffraction (XRD), nitrogen adsorption desorption, Raman Spectroscopy, X-ray photoelectron spectroscopy (XPS), thermogravimetric analysis, Circular dichroism (CD) spectroscopy and Fourier Transform Infrared Spectrometer (FT-IR). The chapter also presents the coin cell assembly and electrochemical testing techniques.

Chapter 4. Herein, we report a series of marine organism-like hollow nanoarchitecture consisting of nitrogen (N) doped 1D carbon nanotubes (CNTs), which were derived from binary Fe@Ce Prussian blue analogs (PBAs) and melamine. This nitrogen-doped 3D hollow scaffold offers large innerspace ($\phi \approx 200$ nm) and sufficient electric conducting for insulating sulfur and provides adsorption sites for immobilizing polysulphides. The introduced double metal species enable strong chemical adsorption toward polysulfides and could facilitate the redox reaction between sulfur and polysulphides. When applied in Li-S batteries, the as-prepared materials showed a high capacity of 1241 mAh g-1 and stable cycling performance (1003 mAh g-1 after 100 cycles) at a current density of 0.2 C. The enhancement of electrochemical activity could be attributed to the 3D hollow architecture of the hybrid, in which the nitrogen-doping generates defects and active sites for improved interfacial adsorption. This work could inspire developing biomimetic architectures for high-performance Li-S batteries.

Chapter 5. Herein, we contend that the protein molecules function as a “self-defense” agent,

mitigating the formation of lithium embryos, thus mimicking natural, pathological immunization mechanisms. When added into the electrolyte, protein molecules are automatically adsorbed on the surface of lithium metal anodes, particularly on the tips of lithium buds, through spatial conformation and secondary structure transformation from α-helix to β-sheets. This effectively changes the electric field distribution around the tips of lithium buds and results in homogeneous plating and stripping of lithium metal anodes. Furthermore, we develop a slow sustained-release strategy to overcome the limited dispersibility of protein in the ether-based electrolyte and achieve a remarkably enhanced cycling performance of more than 2000 cycles for lithium metal batteries.

Chapter 2 Literature review

Since the 1960s, the concept of lithium–sulfur (Li–S) batteries has excited people as a seemingly ideal way for energy storage and conversion. Li–S batteries can deliver high energy storage density, which is almost five times that of lithium–ion batteries. Compared with lithium–ion batteries, the mechanism of energy storage in Li–S batteries is entirely different. The operation of lithium–ion batteries is based on the intercalation of lithium ions into/out of cathode and anode hosts. Because the amount of lithium ions is limited in cathode materials, the theoretical capacity of lithium–ion batteries is limited to ~420 Wh kg^{-1}[9]. In contrast, energy conversion and storage of Li–S batteries is based on the conversion reaction of sulfur to form Li_2S on the cathode and lithium stripping and plating on the anode. The nontopotactic nature of these reactions gives the lithium anode and sulfur cathode a high theoretical specific capacity of 3860 and 1673 mAh g^{-1}, respectively[11-13]. In addition, the average working voltage of Li–S batteries is 2.15 V, which endows them with an energy density of ~2500 Wh kg^{-1} and ~2800 Wh l^{-1}[14]. Sulfur is an inexpensive material with a rich distribution throughout the

world and therefore, is of low cost for commercial applications. However, the research on Li–S batteries was rather stagnant due to quick capacity decay, which impaired further development of Li–S batteries [14].

Recently, wearability and flexibility have become a new trend for electronic devices, which require to be powered by flexible power sources. In this chapter, we mainly discuss the recent development of flexible Li–S batteries, focusing on three aspects: electrode material (cathode and anode), electrolytes, and separators.

2.1 The Working Mechanism and Challenges of Li–S Batteries

The operation of Li–S batteries is based on the electrochemical reaction:

$$S_8 + 16Li \rightarrow 8Li_2S \quad (2.1)$$

During the discharge process, the lithium metal (anode material) is oxidized to lithium ions and electrons that travel through the electrolyte and outer circuit, respectively, to reduce sulfur (cathode material)[15, 16]. The discharge process usually shows two different discharge voltage plateaus[17, 18]. At the first high discharge plateau near 2.4 V, S_8 rings are opened and lithiated to intermediate or long-chain lithium polysulfides (PSs).

$$S_8 \rightarrow Li_2S_8 \rightarrow Li_2S_6 \rightarrow Li_2S_4 \quad (2.2)$$

Then, at the second (lower) discharge voltage plateau (about 2.1 V), the intermediate polysulfides are further converted to lithium sulfide.

$$Li_2S_4 \rightarrow Li_2S_2 \rightarrow Li_2S \quad (2.3)$$

The upper voltage discharge plateau contributes to about 25% of the theoretical capacity (~418 mAh g^{-1}) and the lower discharge plateau contributes to about ~75% of the theoretical capacity (about 1255 mAh g^{-1}). Because the long-chain polysulfides can be dissolved into the electrolyte easily while

sulfur and lithium sulfides are insoluble, the whole reaction undergoes a solid→ liquid → solid sequence. This complicated sequence increases the side reactions of Li–S batteries and has been hindering the practical applications of Li–S batteries[19–21].

Overall, there are four challenges facing the development of flexible lithium–sulfur batteries, which are as follows:

1. *The dissolution of active materials*. Since long-chain polysulfides are soluble in the electrolyte during the discharging process, a large amount of long-chain polysulfides may separate from the cathode. This dissolution normally causes large amount of loss of active sulfur because these long-chain polysulfides are unable to return to the cathode host even during the charging process. This phenomenon causes quick capacity decay and limits the working life span of lithium–sulfur batteries.

2. *The "Shuttle effect"*. Some of the long-chain polysulfides that are dissolved in the electrolyte, migrate through the separator to the anode side and react with the lithium anode. Because of the strong reducibility of elemental lithium, polysulfides can be reduced to Li_2S and Li_2S_2 quickly. Because of the insoluble characteristics of Li_2S_2 and Li_2S, they can passivate the anode surface. This effect is irreversible and causes severe damage to the structure of the anode.

3. *Large volume expansion*. During discharge process, the volume expansion can reach ~80%. The quick volume expansion of sulfur can break its host material and result in the collapse of the whole cathode. The volume expansion of sulfur cathode during the discharge process also decreases mechanical integrity and the stability of electrodes over long time cycling.

4. *Low electronic conductivity of sulfur*. Owing to the insulting nature of elemental sulfur, sulfur cathodes usually have a high internal resistance, leading to poor electrochemical performances.

2.2 Flexible Cathode Hosts for Lithium–Sulfur Batteries

To suppress the shuttling effect and to overcome problems arising from the insulating nature of sulfur, various carbon materials have been applied as cathode materials to improve the capacity and cycling performance of Li–S batteries[22]. The mass of sulfur in the cathode determines the total capacity of Li–S batteries. Therefore, sulfur content in the composite electrode is of vital importance to improve the energy density of the battery system[23]. Generally, achieving high sulfur loading is still a challenge that needs to be resolved in Li–S batteries. Meanwhile, during the discharging process, the volume expansion of sulfur can reach 80 %[24]. This expansion can damage the ordered structure of the cathode materials and result in irreversible capacity loss particularly for flexible cathodes. To solve these problems, many cathode modification methods have been investigated.

In general, carbon nanotubes (CNTs) and graphene can be used as the matrix materials for flexible lithium–sulfur batteries. In 2015, Sun et al. reported an aligned and laminated sulfur-absorbed carbon/CNT hybrid flexible cathode for high performance Li–S batteries (**Figure 2.1 a,b**). In this battery, mesoporous carbon materials were used as the sulfur host to hinder the diffusion of polysulfides. The capacity of the as-synthesized cathode material can reach 1226 mAh g^{-1} with a capacity retention of 75% (100 cycles at 0.1 C). In addition, they also obtained a high capacity of around 900 mAh g^{-1} at 20 mg cm^{-2}, which is the highest sulfur loading reported to date. Moreover, the aligned and laminated hybrid cathode endows the battery with high flexibility and its electrochemical performances are well maintained under bending and after being folded for 500 cycles. Furthermore, aligned CNTs provide better electronic conductivity than freestanding CNTs **(Figure 2.1 c)**[25].

Novel structures, can improve conductivity and tolerate the sulfur volume change, which are

desirable properties for impregnating sulfur and trapping the dissolved PSs during cycling. Porous carbon and porous graphene are three dimensional graphene and have high surface areas for loading sulfur. Considering the mass of aluminum foil typically used as a cathode substrate, the maximum sulfur loading is less than 30 wt% if the mass of Al substrate is taken into account [26]. However, in cases using freestanding porous carbon or porous graphene or three-dimensional graphene, the total sulfur loading can reach as high as 90 wt%. Wang et al. reported macroporous freestanding nanosulfur/graphene (S-rGO) materials, which can be directly employed as an electrode for Li–S batteries. The S-rGO flexible paper used in the batteries was fabricated through a facile freeze drying route followed by low-temperature heat treatment. The flexible S-rGO paper not only provides a conductive framework for electron transport, but also alleviates the volume change during cycling. The as-prepared S-rGO paper shows exceptional rate capability and cyclability. The specific discharge capacity is 800 mAh g^{-1} after 200 cycles at a current density of 300 mA g^{-1} and the capacity fading rate is only 0.035% per cycle. When the current density increased to 1500 mA g^{-1}, it still showed a good performance. This work ascribes the high performance of the S-rGO paper to the stable macroporous structure and strong interaction between sulfur nanoparticles and graphene [27].

Graphene with unique properties including large surface area, light weight, high electrical conductivity, and superior mechanical flexibility, is a promising material for fabrication of flexible Li–S batteries. It has been demonstrated as an effective sulfur immobilizer for Li–S batteries with high performance. Therefore, it is widely considered that graphene will play a great role in the development of flexible sulfur cathodes due to its triple functions in enhancing electronic conductivity, trapping soluble intermediates, and improving the mechanical properties. Despite some progresses, the mechanical properties of the as-fabricated flexible electrodes are still not satisfied and researchers are

making efforts to improve it. For example, Sun et al. reported the employment of super-aligned CNT/graphene (CNT/G) hybrid materials as a 3D conducting framework for sulfur accommodation (**Figure 2.1 f**)[26]. The CNT/G network acts as a skeleton to form a self-supporting cathode. Graphene with a 2D sheet structure extends in an additional dimension to provide improved restriction for sulfur/polysulfides. Moreover, the CNT/G hybrid framework enables better dispersion of sulfur and allows each sulfur particle to attach loosely to the conductive components, which greatly enhances the electrochemical conductivity and thereby approaches the full potential of the active materials. Compared with the S–CNT composite, the S–CNT/G nanocomposite exhibited enhanced mechanical performance and electrochemical characteristics. The S-CNT/G nanocomposite with a superior structure achieved a high discharge capacity of 1048 mA h g^{-1} at 1 C with a capacity fading rate as low as 0.041% per cycle over 1000 charge–discharge cycles (**Figure 2.1 g**) [26].

The electronic and chemical properties of graphene can be effectively modified by the incorporation of heteroatoms into graphene lattice. Therefore, continuous efforts have been made to fabricate doped graphene. Nitrogen-doped, boron-doped, and sulfur-doped graphene exhibit good electrochemical performances and are commonly employed in fuel cells and lithium ion batteries. The reason for the performance enhancement lies in the doped atoms, which have different electron negativities and can break the electro-neutrality of graphene to create charged active sites with increased conductivity to improve the discharging capacity of graphene in Li–S batteries [20]. Introducing 2D graphene sheets into a 3D macroscopic structure is also a unique approach for providing active sites and enough support space for stable cycling. Wang et al. found that hydrothermal and solvothermal treatment of graphene oxide (GO) is a highly efficient method for fabricating 3D–GO structures. A porous three-dimensional nitrogen-doped graphene (3D–NG) was prepared and used

as an interconnected framework for sulfur in Li–S batteries. The 3D–NG-sulfur composite (3D–NGS) with a high sulfur content of 87.6 wt% was synthesized via a facile one-pot solution method and sulfur was well dispersed (**Figure 2.1 d**). The 3D–NGS composite demonstrated excellent rate capability and cyclability. The discharge specific capacity is 792 mA h g^{-1} after 145 cycles at a current density of 600 mA g^{-1} and the capacity fading rate is 0.05% per cycle. Even at a high rate of 1500 mA g^{-1}, the composite still shows a good cycle performance with a capacity of 671 mAh g^{-1} after 200 cycles (**Figure 2.1 e**). The outstanding electrochemical performance is ascribed to the flexible porous 3D structure and N-doping in graphene. The flexible 3D–NG can provide a conductive framework for electron transport and alleviate the volume expansion during cycling. N-doping can facilitate the diffusion of Li ions across the graphene sheets and restrain sulfur due to the strong chemical bonding between S and the nearby N atoms [20].

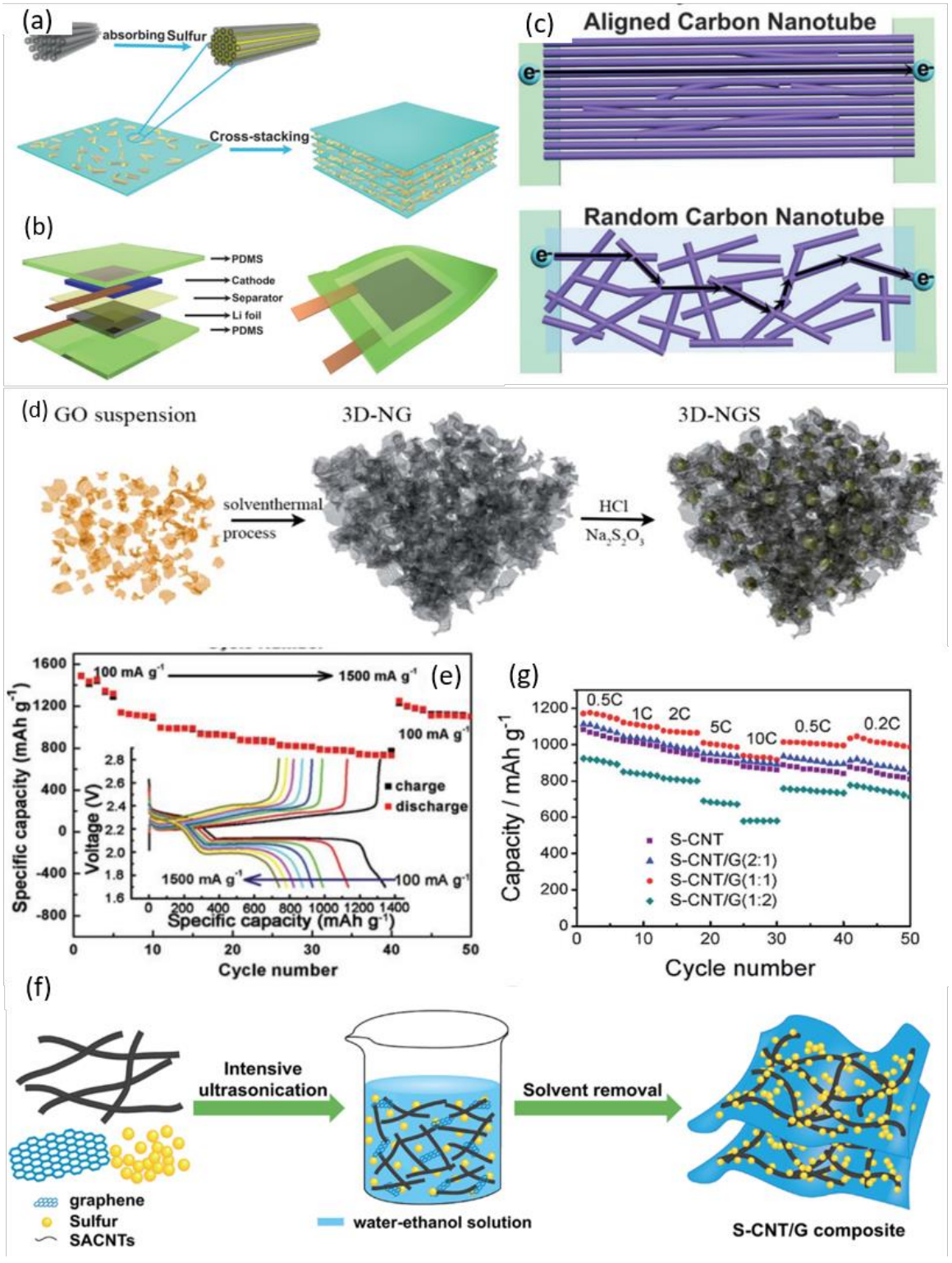

Figure 2.1 (a) The fabrication process of the laminated hybrid sulfur cathode and (b) schematic image of structure of the flexible Li–S battery. (c) Comparison to explain the differences in electronic conductivity between aligned CNTs and random CNTs.[25]. Copyright 2015, John Wiley & Sons. (d)

The preparation method for the S-rGO paper. (e) The rate capability of 3D–NGS with current densities ranging from 100–1500 mAh g^{-1} and the first discharge–charge profiles at different current densities[20]. Copyright 2014, Royal Society of Chemistry. (f) The preparation method for synthesizing S-CNT/G and (g) its electrochemical performance when used as flexible Li–S battery cathode[26]. Copyright 2015, Royal Society of Chemistry.

The key parameter for a good flexible electrode is high tensile strength. However, the poor flexibility and weak adhesion between active materials and metal foil substrates, leads to the pulverization of active materials and performance degradation during repeated bending. Thus, conventional battery electrodes fail to meet the requirements for flexibility. Carbon cloth, carbonized cellulose, and textiles have been commonly applied to construct flexible electrodes and exhibit high mechanical strength and flexibility. Particularly, CNTs and graphene films provide a flexible platform for Li–S batteries. However, until now, flexibility contradicts electrochemical performance, and compromises have to be made, such as relatively fast capacity decay and low sulfur loading, while achieving high flexibility. However, the energy density of the electrodes is lowered by a high mass of the flexible substrates with low active mass content. The energy density of flexible Li–S batteries can be effectively enhanced by employing freestanding electrodes. Vacuum filtration for the preparation of graphene or CNTs as the matrix is becoming common for fabricating flexible electrodes. On the other hand, electrospinning has also been extensively explored for the fabrication of freestanding porous carbon nanofiber films. However, these films exhibited a low breaking strength (usually lower than 2 MPa with 0.5–1.5% strain) and have failed to meet the demands of practical applications. For sulfur-based cathodes, porous carbon nanofibers have been employed to support sulfur [20]. However,

the filled sulfur tends to bond rigidly in the micropores of carbon nanofibers, which degrades the flexibility and is detrimental to the structural stability of the flexible films. Song et al. have demonstrated a novel technique to fabricate flexible and freestanding sulfur cathodes with enhanced mechanical strength using a matrix constructed from graphitized nitrogen-doped mesoporous carbon nanofibers (NPCFs) [28]. The matrix was made by electrospinning followed by carbonization at 1000 °C (**Figure 2.2 a**). Because of the unique micro/mesoporous structure and highly graphitic carbon, the NPCF film can accommodate more sulfur, and maintain substantially high mechanical strength and flexibility after high sulfur loading, compared with traditional microporous carbon nanofiber films (**Figure 2.2 b**). As a freestanding and flexible cathode for Li–S batteries, the robust composite film showed excellent rate capability (540 mAh g^{-1} at 5 C) and cycling stability (76.5 % retention after 500 cycles at 5 C) [31].

Chen et al. fabricated a robust and flexible cathode for Li–S batteries with high electrochemical performance and tensile strength (72.0 MPa) based on interpenetrative composites of carbon nanotubes−graphene/sulfur (CNTs-rGO/S) (**Figure 2.2 c**)[24]. The CNTs and graphene act as both the cathode matrix and separator to inhibit the migration of the dissolved polysulfide intermediates in the electrolyte. Consequently, the robust and flexible CNTs-rGO/S cathode with 53 wt% sulfur showed a reversible capacity of 772 mAh g^{-1} at a current rate of 0.2 C and 613 mAh g^{-1} at 1 C, respectively. It possesses a high electrode capacity of ~409 mAh g^{-1}. Meanwhile, this flexible cathode has good physical flexibility to tolerate shape changes (**Figure 2.2 d**). Such an improved rate capability and cycle stability could be attributed to the unique graphene-wrapped sulfur particles and the enhanced electrical conductivity and mechanical strength from the incorporation of CNTs. Based on the intrinsic properties of graphene, CNTs are proposed to act as an alternative carbonaceous cathode scaffold for

Li–S batteries. The inherent open topology of CNTs enables sulfur particles to be easily diffused as well as to be more efficient for in situ immobilization of sulfur and geometric confinement of polysulfides in the interior face of the tube (**Figure 2.2 e**). Moreover, the highly elastic tubular walls of CNTs is supposed to facilitate radial expansion to accommodate volume variation of enclosed sulfur particles during the lithiation process [24]. Guo et al. used a modified, facile and efficient synthesis strategy to fabricate high-quality 1D graphene nanosheets (GNS) in high yield from GO sheets through fast quenching combined with lyophilization [29]. The as-synthesized GNS have an ordered 1D CNT-like nanostructure with an excellent electronic conductivity and especially a large specific surface area (SSA) of 545 m^2 g^{-1}, which is one of the highest value among the reported GNS materials. Owning to the large SSA, the as-synthesized GNS can be employed as an ideal carrier to incorporate sulfur for cathode assembly. A very high sulfur loading of up to 81 wt% is achievable in the resultant composite cathode (denoted as S@GNS). Three-dimensional (3D) graphene sponge has a continuous conductive structure and numerous pores, which is beneficial for sulfur utilization and anchoring (**Figure 2.2 f**). However, strategies for the fabrication of 3D graphene sponges (3D GS) composited with sulfur nanoparticles are either energy consuming or involve toxic reagents [29]. Thus, a new 3DGS was fabricated via a reduction-induced self-assembly method, which is simple but facile and scalable (**Figure 2.2 g**) [30]. The 3D GS enables fast Li^+ transport, superior electrolyte absorbability, and effective electrochemical redox reactions of sulfur. Consequently, this 3D GS delivered a stable capacity of 580 mAh g^{-1} after 500 cycles at a high rate of 1.5 A g^{-1}, corresponding to a low capacity fading rate of 0.043% per cycle (**Figure 2.2 h**)[31]. According to the previous studies, it has been effectively demonstrated that 3D construction strategies are effective for fabricating flexible high performance Li–S batteries. Three-dimensional current substrates possess a high SSA compared with

the conventional two-dimensional current collectors, providing higher interfacial interaction.

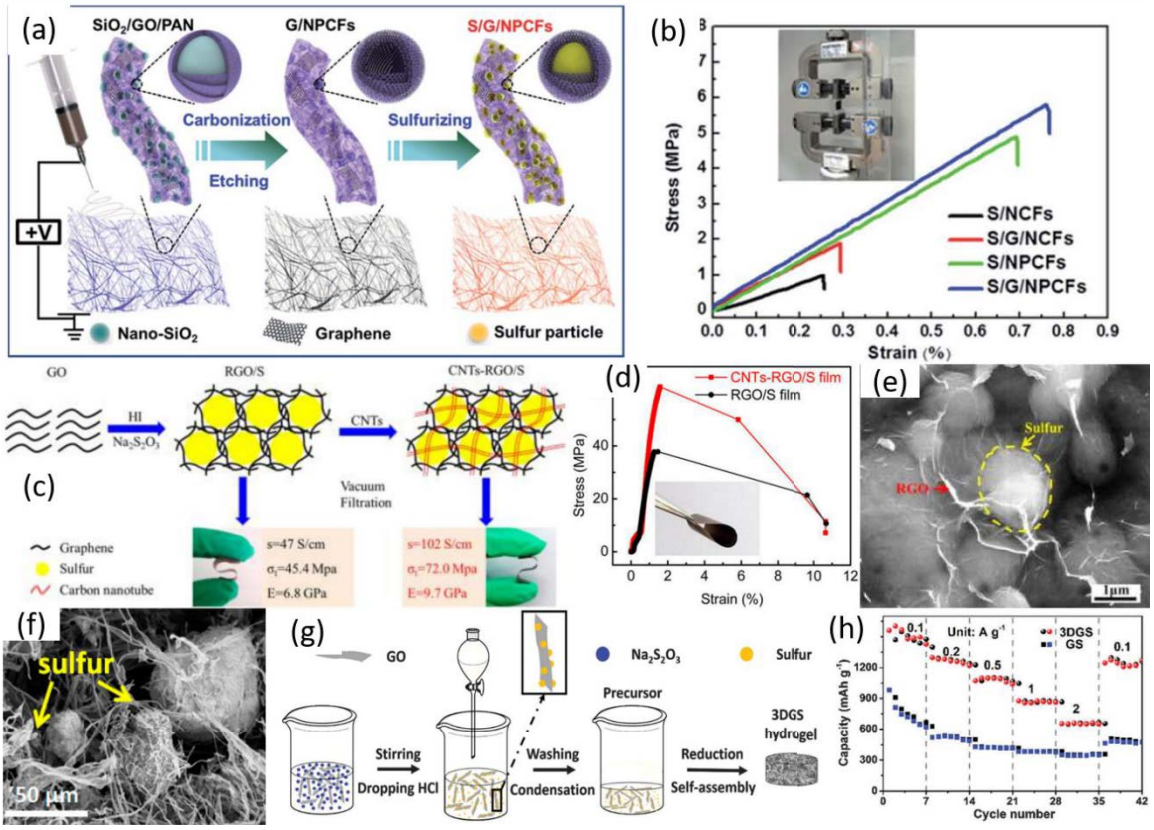

Figure 2.2 (a) The preparation process of NPCFs by an electrospinning method. (b) Typical tensile stress–strain curves of the as-prepared membrane and photograph of the tensile stress–strain testing instrument [28]. Copyright 2017, Royal Society of Chemistry. (c) The preparation process of the CNT–rGO/S composite. (d). The physical performance of CNT–rGO/S. (e) SEM image of sulfur particles and holder materials[24]. Copyright 2015, American Chemical Society. (f) The sulfur particles that are protected by GTS. (g) The preparation process of the 3DGS hydrogel[29]. Royal Society of Chemistry. (h) The electrochemical performance of a Li–S battery using 3DGS hydrogel as cathode material at various current densities[30]. Copyright 2016, Royal Society of Chemistry.

An et al. reported an ultralight flexible carbon foam (MFC) with a 3D interconnected hollow network, which was prepared through a special heat treatment program from melamine-formaldehyde

foam (**Figure 2.3 a**) [32]. The MFC can be employed as a favorable host material to obtain both ultrahigh sulfur loading and satisfactory electrochemical performance in Li–S batteries. Without conductive additive and binders, the sulfur content in the MFC-based cathode could easily reach 75 wt%. The MFC has a high content of N and O atoms, which can strongly absorb the polysulfides. The flexible and sparse skeleton can accommodate large volume changes during electrochemical reactions. GO or rGO was also used to enhance the MFC skeleton to further improve the performance of the electrode. The MFC-based electrodes also showed excellent cycling performances. The initial capacity of the MFC-S, MFC-GO-S, and MFC-rGO-S, are 1011, 1183, and 1135 mAh g^{-1} at 0.1 C, respectively (the capacities were calculated based on the mass of the whole electrodes) (**Figure 2.3 b**). After the irreversible capacity fading in the first few cycles, the capacity retention is over 95% after 100 cycles, indicating that the carbon foam may be an excellent cathode matrix for Li–S batteries for high sulfur loading [32].

Song et al. constructed a novel sulfur cathode consisting of a layer of sulfur-active materials sandwiched by two flexible porous carbon membranes [33]. Compared with the previously reported sulfur cathodes, this novel sandwich-structured cathode design shows many advantages. Firstly, the internally connected carbon foam provides large surface area and many active sites for polysulfide binding. Secondly, the charge transfer resistance is significantly decreased compared to conventional sulfur cathodes not only due to reduced contact resistance between sulfur cathodes and current collectors but also due to intimate contact between sulfur and the two layers of highly conductive carbon. Thirdly, this carbon-supported sandwich-structured cathode is flexible, which can potentially extend Li–S batteries to other applications such as wearable devices, and implantable biomedical devices[33]. Milroy and Manthiram synthesized nitrogen-doped mesoporous carbon cathode materials,

which can promote chemical adsorption between the sulfur and oxygen functional groups and effectively immobilize the sulfur species and minimize sulfur loss. They further noticed that the carbon foam calcined at 800 °C displayed the best stability, which was closely related to the foam structure [34].

Wang et al. have developed a simple drop coating method to prepare a Li_2S/rGO cathode paper for flexible Li–S batteries as a freestanding and binder-free cathode without the use of viscous slurries or metal substrates[36]. It showed both high rate capability and long cycling life. He et al. synthesized 3D CNT/graphene-Li_2S (3D CG-Li_2S) cathodes (81.4 wt% Li_2S loading) by solvothermal reaction and a subsequent liquid–infiltration–evaporation impregnation method[37]. The highly flexible and conductive 3D mesoporous interconnected network based on two-dimensional (2D) graphene nanosheets and one-dimensional (1D) CNTs provides highly efficient channels for electron transfer and ionic diffusion, leading to a low solubility of polysulfides during electrolytes in charges/discharges. Without polymeric binders or conductive additives, the freestanding 3D CG-Li_2S cathode exhibited excellent electrochemical performances including reversible discharge capacities of 1124 and 915 mAh g^{-1} at current densities of 4.5 and 3.4 mAh g^{-1}, 0.02% long-term capacity decay per cycle and a high rate capacity of 514 mAh g^{-1} at 4 C. He et al. also reported the other 3D material, 3D LG, (three-dimensional Li_2S/graphene hierarchical architecture with Li_2S nanoparticles deposited into a 3D GF network). They fabricated 3D LG via drop casting and heating. The electrode delivered a high discharge capacity of 895 mAh g^{-1} at 0.1 C and maintained 87.7% of the initial reversible capacity after 300 cycles (0.2 C) and a high rate capacity of 599 mAh g^{-1} up at 4 C. 3D LG sets a new record and has a great potential for high-performance Li–S batteries (**Figure 2.3 g**) [37, 38].

The design of flexible cathode scaffolds that can maintain good interfacial contact between all the building blocks for high-performance Li–S batteries must meet the following requirements. (i) enhancement of electronic conductivity throughout the whole cathode scaffold; (ii) a low rate of polysulfides dissolution; (iii) high utilization of active materials; and (iv) high mechanical strength to resist large volume changes during repeated charge/discharge processes. Therefore, more and more novel materials have been investigated to satisfy the needs of cathodes with good cycle life for high-performance Li–S batteries. Huang et al. have reported a flexible 3D carbonized bacterial cellulose (CBC) aerogel [39], as the sulfur support. The 3D CBC has highly nanofibrous structures with good mechanical stability and high electrical conductivity. The unique interconnection network of CBC provides satisfactory electrical conductivity as well as a solid framework, which can maintain the tension produced by volume changes of the active sulfur. This interconnected macroporous structure allows lithium ions to migrate rapidly. In addition, the ultralight CBC layers between the sulfur cathode and the separator membrane lessen the resistance of the entire electrode. More significantly, the CBC layer can effectively relieve the excess accumulation of sulfur on the cathode surface. Even at a high sulfur loading content, the CBC composite still has enough free space to accommodate the volume expansion of sulfur in the lithiation process. In addition, the CBC layers inserted between the sulfur cathode and the separator promotes active material utilization, cycle stability, and significantly improved coulombic efficiency. The CBC layer can also be used as an extra collector of sulfur to prevent the excessive concentration of insulating sulfur on the cathode surface. The good electrochemical properties can be attributed to the rational design of the battery configuration and the flexible three-dimensionally interconnected nanostructure of the carbon framework. Ghosh et al. investigated the interaction between the particle size with mechanical and electrochemical properties

(**Figure 2.3 g**) [35]. They reported a bottom-up approach, creating a unique independent type of flexible cathode matrix. It is composed of porous graphene oxide, nanosized sulfur, and Mn_3O_4 nanoparticles, which are mixed with polyaniline (PANI) with a sodium alginate (SA) matrix for three-dimensional mutual connection. A capacity of 1098 mAh g^{-1} is achieved after 200 cycles at a current rate of 2 A g^{-1} with 97.6% of the initial capacity maintained. Interestingly, at the higher current density of 5 A g^{-1}, the composite electrode still exhibited an initial capacity of 1015 mAh g^{-1} and retained 71% of the original capacity after 500 cycles. In situ Raman study confirms the polysulfide absorption capability of Mn_3O_4. The synergistic effect of each component resulted in excellent electrochemical performances including high rate capability, high specific capacity, and unprecedented cycling stability. It is believed that the simple and inexpensive electrode design concept can open new avenues for practical industrial applications of Li–S batteries with high energy density.

At present, flexible Li–S battery systems mainly use carbon-based materials to accommodate sulfur. Most research studies focus on modification of individual components of batteries, especially electrode materials. However, the fluidity of liquid electrolytes restricts the development of flexible Li–S batteries, because the bending and stretching processes make the cell more prone to leakage, resulting in corrupted safety, thus limiting its application in flexible electronics [28]. Therefore, we also summarize the development of electrolyte for flexible Li–S batteries.

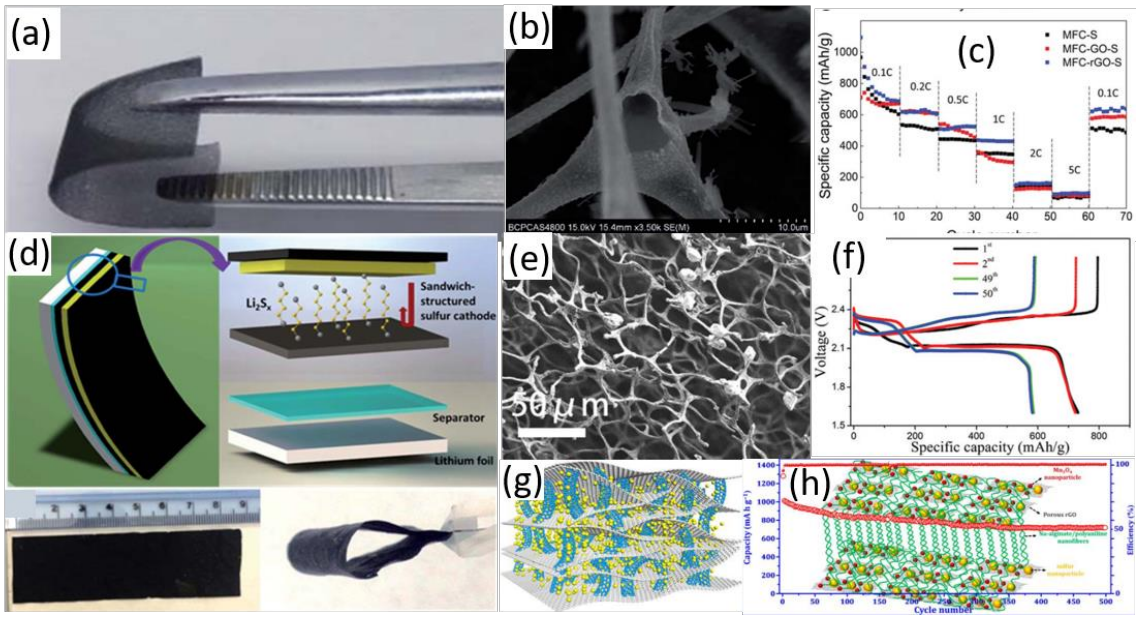

Figure 2.3 (a) The flexible porous structure of the material and (c) the discharging capacity at various current densities [32]. Copyright 2016, Royal Society of Chemistry. (d) Li–S battery with sandwich-structured cathode that can be curved or bent[25]. Copyright 2014, Royal Society of Chemistry. (e) SEM view of sulfur particles that are attached on carbon foam. (f) The charge and discharge curve of the battery [34]. Copyright 2016, Royal Society of Chemistry. (g) The structure of 3DCNT/Graphene-Li_2S aerogel. (h) Electrochemical performance of scaffold material [35]. Copyright 2016, American Chemical Society.

2.3 Electrolyte Membranes for Flexible Li–S Batteries

Conventional Li–S batteries usually consist of liquid electrolytes, which show excellent integrated properties such as high Li ionic conductivity (about 10^{-2} S cm^{-1}) and form a satisfactory contact interface with solid electrodes. However, because of their fluidity, electrolytes may leak once cells are bent or stretched in flexible batteries. Their fluidity may also distort the size and shape of the battery, which cannot meet the demands of flexible and microminiaturized electronic devices.

Therefore, the development of solid but flexible electrolytes is a focal point of research for flexible Li–S batteries. Remarkable improvements have been achieved through enormous efforts made by several groups [40, 41].

Compared with liquid electrolytes, using solid electrolytes has been recognized as one of the most promising approaches for high safety requirements because they can eliminate concerns about internal short-circuiting and leaking when facing large stresses in wearable devices [42]. Moreover, solid electrolytes can also isolate the positive and negative electrodes of a battery (working as a separator), effectively avoiding internal shorting and increasing the energy density of the battery. There are still some obstacles for solid electrolyte applications [43, 44]. Some solid electrolytes cannot achieve good contact with solid electrodes, resulting in poor cycle life. Another major disadvantage of solid electrolytes is that they exhibit low Li ionic conductivities (about 10^{-6} S cm^{-1}) at room temperature [45]. In contrast, gel polymer electrolytes (GPEs) containing liquid traditional electrolytes in polymers, exhibit high ionic conductivities, and therefore are more suitable for flexible Li–S batteries. Both composite polymer electrolytes (CPEs) and GPEs show promising properties in flexible Li–S batteries [46].

GPEs are usually prepared by immobilizing liquid electrolytes in a polymer matrix. Liquid electrolytes provide a high ionic conductivity while the polymer backbone provides good mechanical strength and flexibility [46, 47]. At the same time, GPEs can integrate with electrode materials closely after the monomer polymerization process. Thus, the flexible Li–S batteries can withstand more severe deformation and their lifespan can be extended. **Figure 2.4 a–c** shows the electrochemical performance of GPE-based batteries and their immobilization mechanisms for polysulfides during charging and discharging cycles.

2.3.1 Solid Polymer Electrolytes for Flexible Li–S Batteries

Polyethylene oxide (PEO) is one of the most popular solid polymer electrolyte (SPE) for Li–S batteries [49, 50], in which the –C–O–C– bond units facilitate ion conduction. Much enhancement has been made to improve the performances of PEO [51]. However, the ion conduction is hindered at low temperatures [52], which is a major barrier for applications.

Liu et al. studied sucrose-based electrolytes because they provide similar bonds as PEO [19]. They dissolved sucrose in pyridine and added PEO (to improve the mechanical properties and facilitate freestanding performance) and LiTFSI to the solution. The final sucrose-based electrolyte was obtained after solvent casting. They found that the electrolyte had excellent electrochemical properties and showed better chemical and mechanical properties than PEO. When sucrose is added to PEO, the ionic conductivity can be largely improved. As shown in **Figure 2.4 d**, the higher the sucrose that was added, the higher the ionic conductivity that was obtained, which suggests that sucrose had a higher ionic conductivity than PEO. The Li ionic conductivity of sucrose-based PEO reached 4.28×10^{-4} mS, which was considerably higher than SPEs. SPE modified by sucrose was uniquely advantageous to high lithium ion transference, which might be attributed to the fact that it only transferred Li ions rather than other ions. It was very stable when it was in contact with lithium at various temperatures. The cycle number in **Figure 2.4** shows its excellent stability. As shown in **Figure 2.4 f**, the capacity of the sucrose-PEO cell remained almost constant after charging and discharging 200 cycles [10].

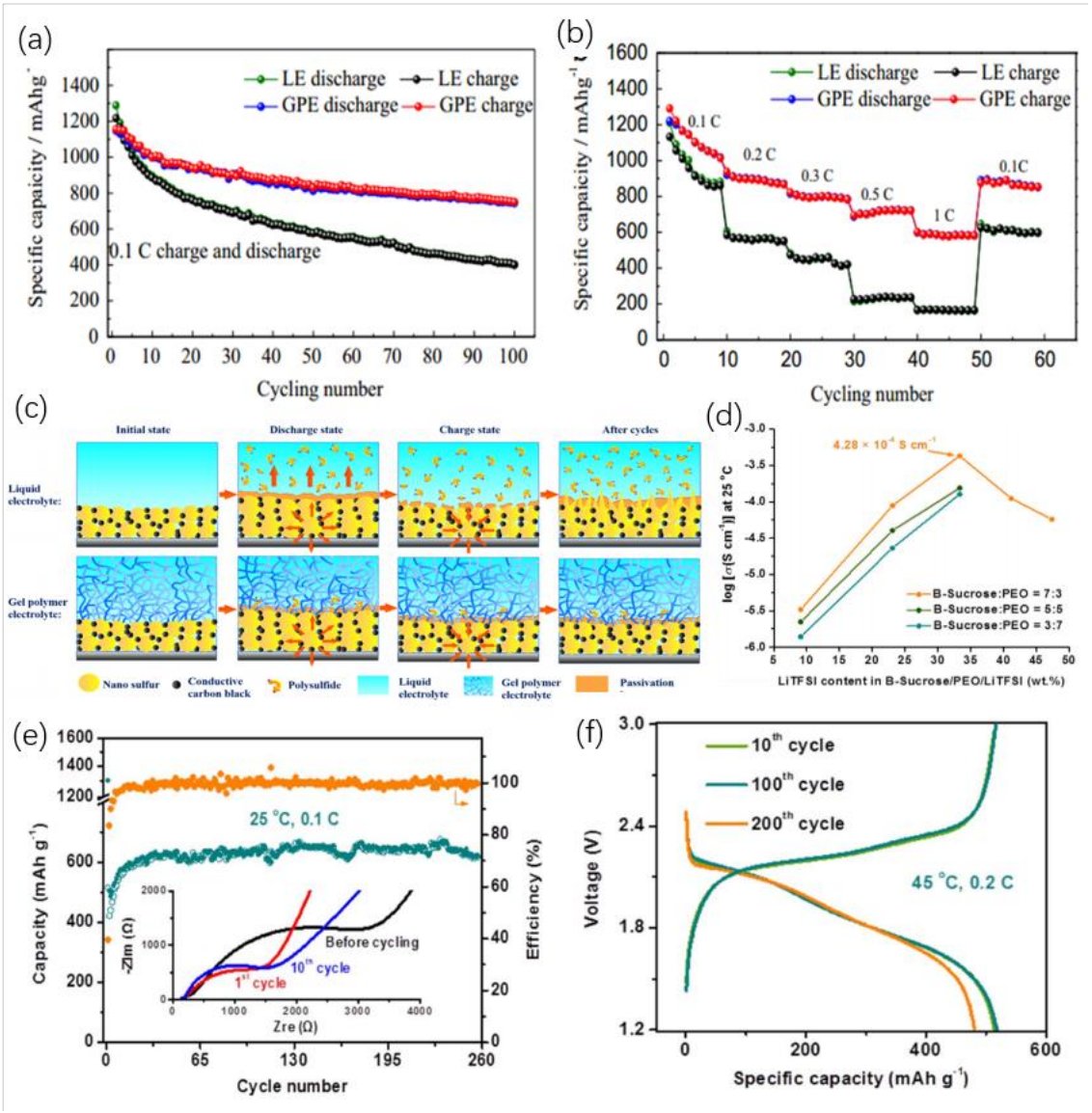

Figure 2.4 (a) Cycling performance of GPE-based batteries, and those of liquid-based ones at 0.1 C. (b) Rate performance of GPE-based batteries and the liquid-based ones from 0.1 to 1 C. (c) The polysulfide immobilization mechanism of GPE-based batteries and the liquid-based ones. Dendrites continually grow on the sulfur electrodes' surface in the liquid electrolyte-based batteries while the GPE-based ones can maintain a smooth morphology [48]. Copyright 2016, Elsevier B.V. (d) With the increasing weight ratio of sucrose in the sucrose-PEO electrolyte, the ionic conductivity increases obviously. (e) Cycling performance of Li–S batteries with sucrose-PEO electrolyte and the electrochemical impedance spectroscopy (EIS) spectrum of the battery. (f) Specific capacity of cells

using the sucrose-PEO electrolyte. The value remained almost constant after 200 cycles.[10]. Copyright 2017, Electrochemical Society.

In 2002, Professor Scrosati and Aihara firstly prepared PEO-based SPEs by immersing a PEO-SiO_2 membrane into liquid electrolyte [53]. In 2013, Zhang and Concept reported that SiO_2 can be added in situ into the PEO-50 (50% SiO_2 and 50% PEO composite) and achieved distinctive results for Li–S batteries [54]. The most notable difference between sucrose-based PEO and SiO_2-based PEO was that the latter was very flexible and could be rolled easily without any dimensional shrinkage or cracks (**Figure 2.5 a**), which is ideal for constructing flexible Li–S batteries. It also showed more satisfactory electrochemical performances with an ionic conductivity of 1.84×10^{-3} S cm^{-1} at 20 C. **Figure 2.5 b** shows the capacity retention of the liquid electrolyte and the 50% PEO–50% SiO_2 electrolyte. The liquid electrolyte took 17 cycles to reach peak performance whereas the SiO_2-based one took only 2 cycles [54].

In 2015, Choudhurry et al. reported that one-dimensional CNTs-modified PEO exhibited an ionic conductivity of 2.07×10^{-5} S cm^{-1} at 25 C [56]. Lin et al. used a natural aluminosilicate ($Al_2Si_2O_5(OH)_4$) nanoclay to fabricate the electrolyte, which is low cost and eco-friendly [55]. They mixed CNT, LiTFSI, and PEO in a solution which was cast and dried into a thin film. **Figure 2.5 c** shows the preparation and the mechanism of flexible halloysite nanoclay electrolyte. They found that the conductivity for lithium ions was greatly increased because the dissociation of Li ions was promoted by the ordered 3D channels in the electrolyte. It exhibited exceptional ionic conductivity of 1.11×10^{-4} S cm^{-1} and the lithium ion transference number was 0.4 at room temperature. Furthermore, halloysite nanoclay could address the issue of PEO's crystallinity at low temperature because it can lower transition temperature and prevent PEO from forming crystals. The halloysite nanoclay-based electrolyte also showed

distinctive thermal and mechanical stability. It remained nonfractured in a 400% strain state (**Figure 2.5 d**), which is a significant characteristic for flexible Li–S batteries. **Figure 2.5 e&f** also shows its stable cycling life. Overall, although SPEs provide high stability, the ionic conductivity is not as high as that of liquid electrolytes. Besides, the flexibility may be restricted due to their solid-state nature [53].

2.3.2 Gel Polymer Electrolytes for Flexible Li–S Batteries

GPEs are usually prepared by incorporating liquid electrolytes in a polymer gel. When a polymer contains more oxygen atoms, it will coordinate with more Li ions and its ionic conductivity will be increased significantly [57], However, in the presence of organic solvents, GPEs' mechanical strength will be decreased. Several investigations found that cross-linked polymer could improve the ionic conductivity without forming a crystalline phase [58, 59]. Furthermore, mixtures of 1,2-dimethoxyethane (DME) and 1,3-dioxolane (DOL) were used as the polymer. However, DME and DOL showed high lithium polysulfide solubility and might cause severe loss of sulfur under electrochemical cycling.

Choudhary et al. prepared a cross-linked polyepichlorohydrin GPE by dipping cross-linked polymeric films into an electrolyte to minimize active material loss [60]. With the addition of ethylene thiourea (ETU), the decomposition temperature of GPE increased and the weight loss could be minimized at room temperature. So, a wider usage temperature window could be realized. ETU showed a good balance of tensile strength and elongation in a gummy state. **Figure 2.5 g** shows the stress–strain curves of GPE assisted by ETU. With the addition of ETU, the tensile strength was enhanced. The ionic conductivity was 2.4×10^{-4} S cm^{-1} at 298 K. As shown in **Figure 2.5 h**, the

specific capacity of batteries with this kind of electrolyte decreased by 50% after 50 cycles.

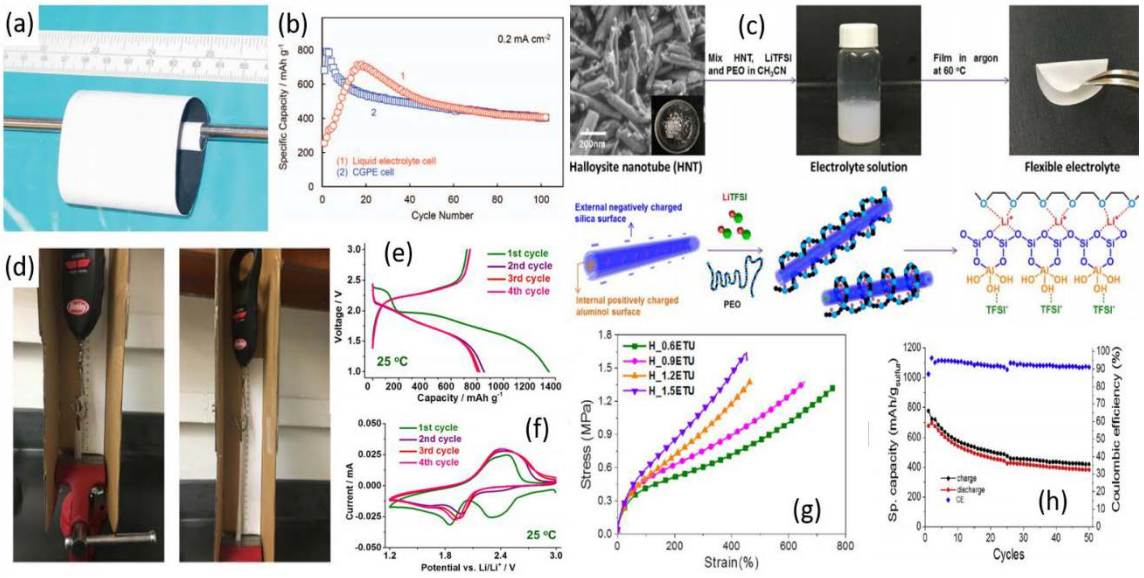

Figure 2.5 (a) 50PEO–50SiO_2 composite electrolyte membranes, that were flexible enough to be rolled into a tube. (b) Capacity retention of Li–S battery with (1) common liquid electrolyte and (2) the 50PEO–50SiO_2-based electrolyte.[54]. Copyright 2013, Electrochemical Society. (c) Preparation and mechanism of the flexible halloysite nano-clay electrolyte. Cast and dried after HNF, LiTFSI, and PEO were mixed to obtain a thin film and the ordered 3D channels promoted ionic conduction. (d) Photos of initial and final tension state of the halloysite nanoclay electrolyte film. (e) Discharge and charge curves of a battery with halloysite nano-clay electrolyte at 25 C. (f) Cycling performance of a battery with the halloysite nanoclay electrolyte at 25 C.[55]. Copyright 2017, Elsevier B.V. (g) Stress–strain of GPE assisted by ETU. (h) Charge and discharge stability test of a battery with ETU-assisted GPE.[56]. Copyright 2017, Elsevier B.V.

Liu et al. crafted a pentaerythritol tetra acrylate (PETEA)-based GPE to suppress the shuttle effects and the electrolyte showed remarkable performances [48]. Liu's group used an in situ synthetic strategy to synthesize PETEA-based GPE and enhanced the performance of the electrolyte. It showed an extremely high ionic conductivity (1.13×10^{-2} S cm^{-1}) at room temperature, which was even higher

than the conductivity of liquid electrolytes (1.19×10^{-2} S cm^{-1}) at 298 K due to the unique molecular structure of PETEA. It could strongly inhibit the polysulfide dissolution and restrain dendrite formation, which successfully suppressed the shuttle effects in Li–S batteries. As shown in **Figure 2.6 a**, PETEA-based electrodes maintained a smooth morphology after 50 cycles, whereas, dendrites usually grow on the surface of the liquid electrolyte electrodes.

In addition, the PETEA-based GPE exhibits excellent stability due to the immobilization of polysulfides. It could retain a capacity of 803.2 mAh g^{-1} (91.78% capacity retention) after 45 cycles. Remarkably, it showed an excellent stability under different shape deformations as shown in **Figure 2.6 b**. Furthermore, the synthetic route is simple, low cost, and easy to control, which may be beneficial for the further development of safe and flexible Li–S batteries. However, the relatively low conductivity and poor mechanical strength still need to be improved.

2.3.3 Composite Polymer Electrolytes for Flexible Li–S Batteries

As GPEs have stimulated tremendous research recently, several research groups have turned their attention to CPEs, because CPEs have both the mechanical strength of solid electrolytes and the high ionic conductivity of liquid electrolytes. Several groups used nano- or microsized ceramic particles such as SiO_2 [62], Al_2O_4 [63], and TiO_2 [61, 64] to obtain CPEs. Their physicochemical properties mainly depend on their modification process [65, 66]. Kurc and Jesionowski used TiO_2–SiO_2 submicron size powders as fillers in CPEs to create a more stable TiO_2–SiO_2 modified CPE. The desired ionic conduction could be attained with the combination of crystalline structured TiO_2 and amorphous SiO_2. SiO_2 increased the surface area while TiO_2 increased thermal stability and mechanical strength simultaneously [61]. The ionic conductivity of TiO_2–SiO_2 modified CPE was 9.8×10^{-4} S cm^{-1} at 298 K and also exhibited good cyclability and Coulombic efficiency. **Figure 2.6 c** shows that the cell using

this electrolyte lost only 0.02% of its capacity per cycle during cycling processes. SEM images (**Figure 2.6 d**) show the porous structure of the electrolyte, which hosts the electrolyte solution and has a flexible cell geometry [61].

Although SPEs can eliminate the safety problems associated with liquid electrolytes, their ionic conductivity is low and flexibility may be limited due to their solid state nature. GPEs, with better mechanical strength and higher ionic conductivity, can withstand more severe deformation. CPEs can achieve both high ionic conductivity and excellent mechanical strength.

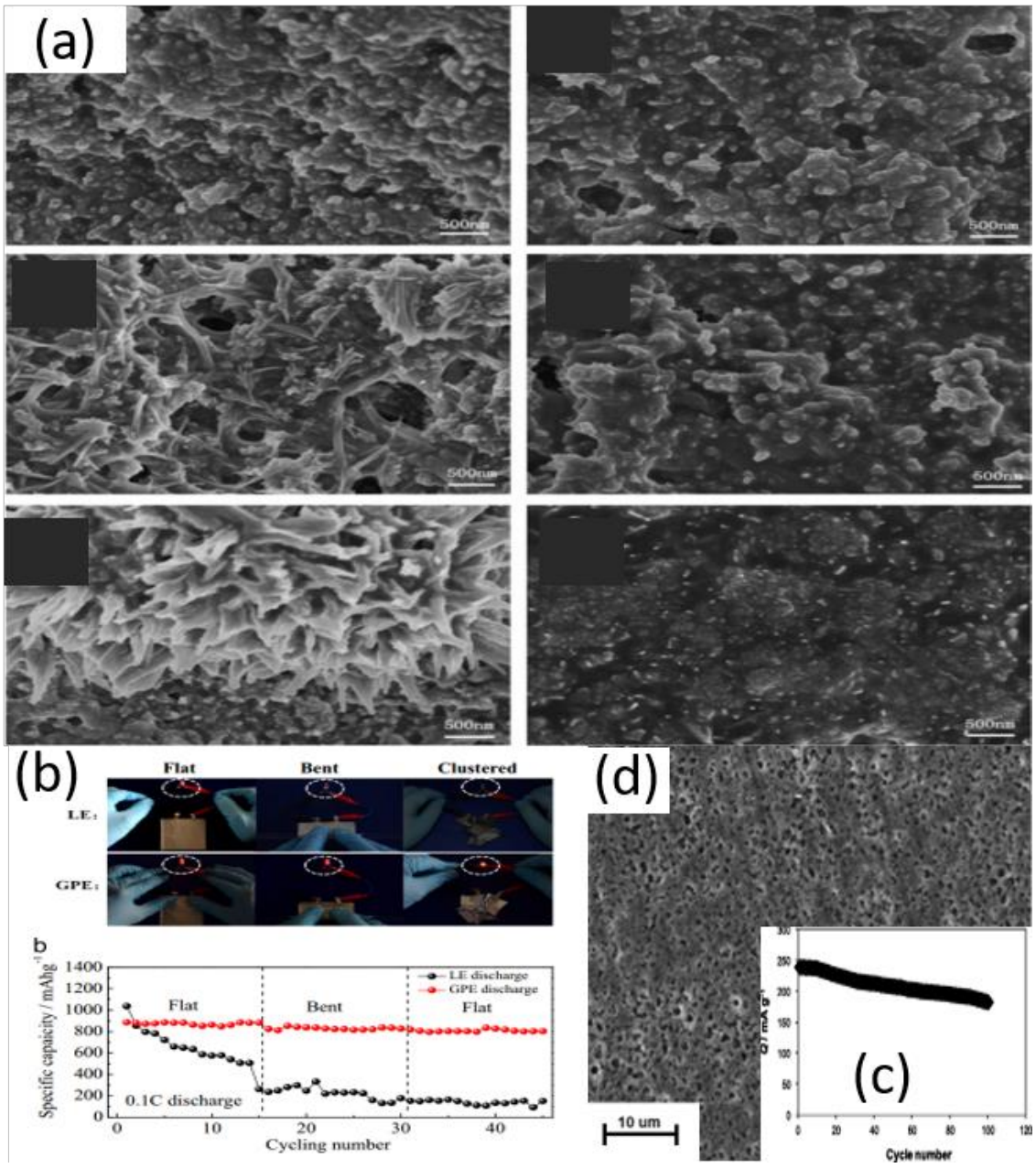

Figure 2.6 (a) SEM images of electrodes with PETEA (3 right) and liquid (3 left) electrolytes' surface after 2 and 50 charge and discharge cycles. (b) The PETEA-based GPE under serious deformation could power a light-emitting diode (LED) lamp while the liquid one could not. Compared with liquid electrolyte, PETEA-based GPE could maintain its stability when bent and had the same specific capacity as before when returned to a flat shape. Source: Liu et al. 2016 [48]. Copyright 2016, Elsevier B.V. (c) How the charge capacity of TiO_2–SiO_2-modified CPE depends on the number of cycles. (d) SEM images of the porous structure of TiO_2–SiO_2-modified CPE. [61]. Copyright 2015, Springer

Nature.

2.4 Separator for Flexible Li–S Batteries

Compared with conventional batteries, flexible batteries have more requirements on flexibility, elasticity, and chemical stability of separators, because the break of separators can cause severe damage to the entire battery system [67]. In a Li–S battery, the separator normally needs other functions and more characteristics:

1. The surface facing the cathode can limit the diffusion of polysulfide to improve the life span and reduce capacity decay [68, 69].
2. The separator surface can improve the conductivity and the cycling ability of active materials. This has been found helpful for improving columbic efficiency and working life span [70, 71].
3. The surface facing the anode material can prevent the growth of needle-like crystals (dendrites), which is recognized as a fatal problem for battery safety [72, 73].

In 2015, Zhou et al. invented a flexible sulfur–graphene–polypropylene (PP) separator integrated electrode system by combining a cathode electrode and separator together.[74] As shown in **Figure 2.7 a**, it is different from other freestanding metal or graphene collectors in that a graphene membrane was directly coated onto a commercial PP membrane. The separator not only divides the cathode and anode, but also supports graphene and sulfur. Its excellent flexibility and mechanical strength make this graphene@PP membrane dynamic and robust. The graphene in this membrane functions as an internal collector to support 70% sulfur loading. SEM image shows that the graphene coating is about 30 μm

thick (**Figure 2.7 b**). They claim that this material can replace Al foil, which always accounts for approximately 5–9% of a battery weight. Additionally, the presence of graphene can retain the dissolved polysulfides. The modified adhesion between sulfur and graphene membrane can significantly decrease polarization and the interfacial contact resistance. After being bent for many times, the flexible capacity and stable conductivity still remained (**Figure 2.7 c**). To further confirm the excellent electrical contact between sulfur and the separator, they compared S-G@PP membrane, G-S + PP membrane and Al foil-S + PP membrane batteries cycled at various current densities (**Figure 2.7 d**). The highest initial discharge capacity of the battery using the S-G@PP separator reached 1278 mAh g^{-1} at 0.3 A g^{-1} while the Li–S battery with a traditional separator battery showed a quick capacity decay [74].

Many people attempted to modify Celgard™ membranes to meet the requirements of flexibility and stronger diffusion suppression of polysulfides without losing their ion transport ability. For example, Ghazi et al. deposited a MoS_2 layer on the surface of a Celgard™ separator (**Figure 2.7 e**). MoS_2 is a kind of A–B–A sandwich-like 2D material, which has both a superior chemical stability and a higher SSA. Because of the high density of lithium ions on the MoS_2 surface, this composite separator shows fast lithium diffusion and facile lithium transference. When used in a Li–S battery, the separator is proven to be highly efficient for restricting polysulfide shuttle and increasing the service life. When the sulfur loading was 65%, the battery capacity was 808 mAh g^{-1} after 600 cycles. The coulombic efficiency remains above 99.5% during all 600 cycles (**Figure 2.7 f**). As shown in **Figure 2.7 g**, the battery with MoS_2 Celgard™ separator delivers an initial discharge capacity of 804 mAh g^{-1}, which is higher than the battery with an unmodified plain separator. They found that the diffusion coefficient

for the MoS_2 Celgard™ separator at lower voltages is higher than both GO/Celgard™ and pristine Celgard™. At lower voltages, the high-order polysulfides convert to solid lithium sulfides. These polysulfides could easily precipitate at the cathode–separator interface as an insulating layer and then hinder lithium ion diffusion. They deduced that the MoS_2 nanosheets provide voids to accommodate various redox species and prevent the formation of such an insulating layer, leading to facile lithium ion diffusion [31].

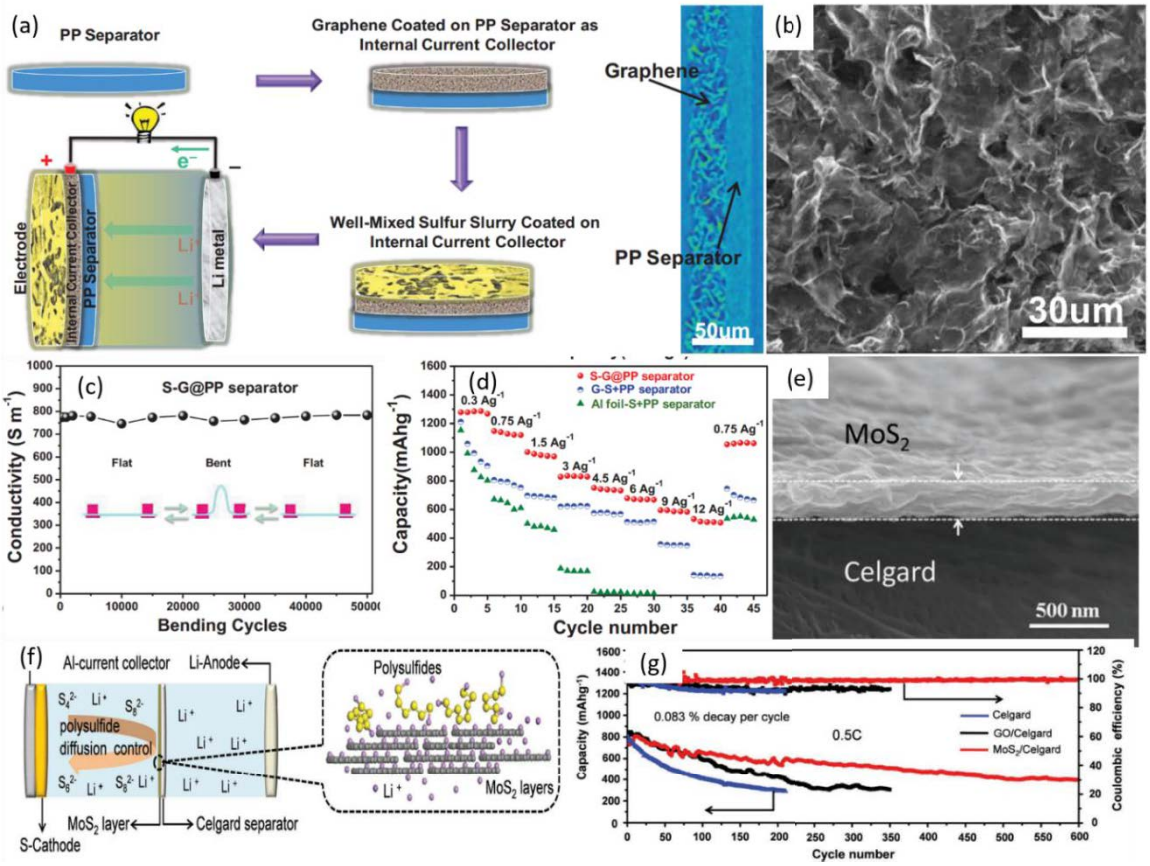

Figure 2.7 (a) Schematic of electrode configuration illustrating the process of combining sulfur and graphene@PP membrane to form an integrated electrode–separator structure. (b) Cross-section SEM image of sulfur electrode and corresponding EDS spectrum. (c) Stability of electrode–separator combination in terms of conductivity after 5000 bending cycles. (d) Rate performance of the S-G@PP separator, G-S + PP separator and Al foil-S + PP separator batteries at different current densities. [74]. Copyright 2015, Wiley. (e) Cross section of MoS_2-Celgard layer. (f) Schematic Li–S battery

configuration of MoS_2 Celgard™ separator. (g) The cycling performance for Celgard™, GO/Celgard™, and MoS_2/Celgard™ separators at 0.5 C. [31]. Copyright 2017, Wiley.

Jiang et al. attempted to inhibit the shuttle effect by coating GO on a membrane. They found that compared with pristine Celgard™ membrane, less sulfur and polysulfide species were left on the GO-coated separator membrane. The graphene oxide modification also created a three dimensional porous structure, while maintaining the ideal flexibility of pristine Celgard™ membrane (**Figure 2.8 a**). They declared that the graphene modification is a good way to construct a separator membrane with an ideal electrochemical performance [75].

Abbas et al. fabricated a bifunctional separator by spray coating poly(3,4-ethaylenedioxythiophene):poly(styrene sulfonate) (PEDOT:PSS) on the surface of the separator. They found that after the modification, the surface of the separator can transform from hydrophobic to hydrophilic, resulting in greater wettability, better electrolyte intake, and improved electrochemical performance. This structure could greatly increase the cycling stability of Li–S batteries with a capacity loss as low as 0.0364% per cycle after 1000 cycles at a current rate of 0.25 C. More importantly, this membrane has unique flexibility and can retain a stable conductivity even when bearing large structure bending (**Figure 2.8 b,c**). The modified separator has abundant sulfonate functional groups (from PSS). The stable specific capacity can be ascribed to PSSs' negative charges, which effectively suppresses the shuttle effect through mutual coulombic repulsion. Meanwhile, the PEDOT also supports chemical interactions and forms a chelated coordination structure. PSS can be considered as a dopant in PEDOT:PSS, which can facilitate lithium ion transport, and provide a “polar solvent-philic”

environment [76]. Wei et al. demonstrated another way to modify Celgard™ separators with a polyvinylidene fluoride-C (PVDF-C) layer, whereby the polysulfides generated during discharge processes can be anchored on the cathode side (**Figure 2.8 d**). Similar to Abba's discovery, the hydrophilic performance yields a large intensification (**Figure 2.8 e,f**). Li–S batteries based on this modified separator achieved a high discharge capacity of 919 mAh g^{-1} after 100 cycles at a rate of 0.5 C. Even at a current rate of 5 C, the batteries were able to maintain a discharge capacity approximately 400 mAh g^{-1}. The exceptional electrochemical performance can be attributed to the enhanced adsorption capability of the micropores. Meanwhile, the presence of C–C double bonds, and the conductivity of the carbon networks in the PVDF-C layer also compensate for the low conductivity of elemental sulfur. This economical and simple strategy to overcome polysulfide dissolution provides a commercially feasible carbon method for the development of flexible Li–S batteries [78]. Zhang et al. presented a separator with nitrogen-doped porous hollow carbon sphere coating, which showed enhanced electrochemical performance. The high initial discharge capacity of 1656 mAh g^{-1} and a low fading rate of 0.11% per cycle within 500 cycles (1 C) were achieved. This is ascribed to the chemical and physical adsorption properties of porous and nitrogen-doped NHCs. The separator demonstrated an excellent flexibility and chemical stability as shown in **Figure 2.8 g,h** [15].

Cui and Fu reported a “linear voltage” sweep method to quantitatively measure anodic (oxidization) currents of polysulfides crossing the separators. As shown in **Figure 2.8 i**, when the liquid polysulfide solution was added to the CNT paper, the polysulfides migrated through the separator to the electrode and were oxidized to form elemental sulfur. The electrical charge in Coulombs produced by the oxidation of polysulfides is linearly related to the concentration of polysulfides within a certain range (≤0.5 M). This method provides guidance for developing new separators for flexible Li–S

batteries [77].

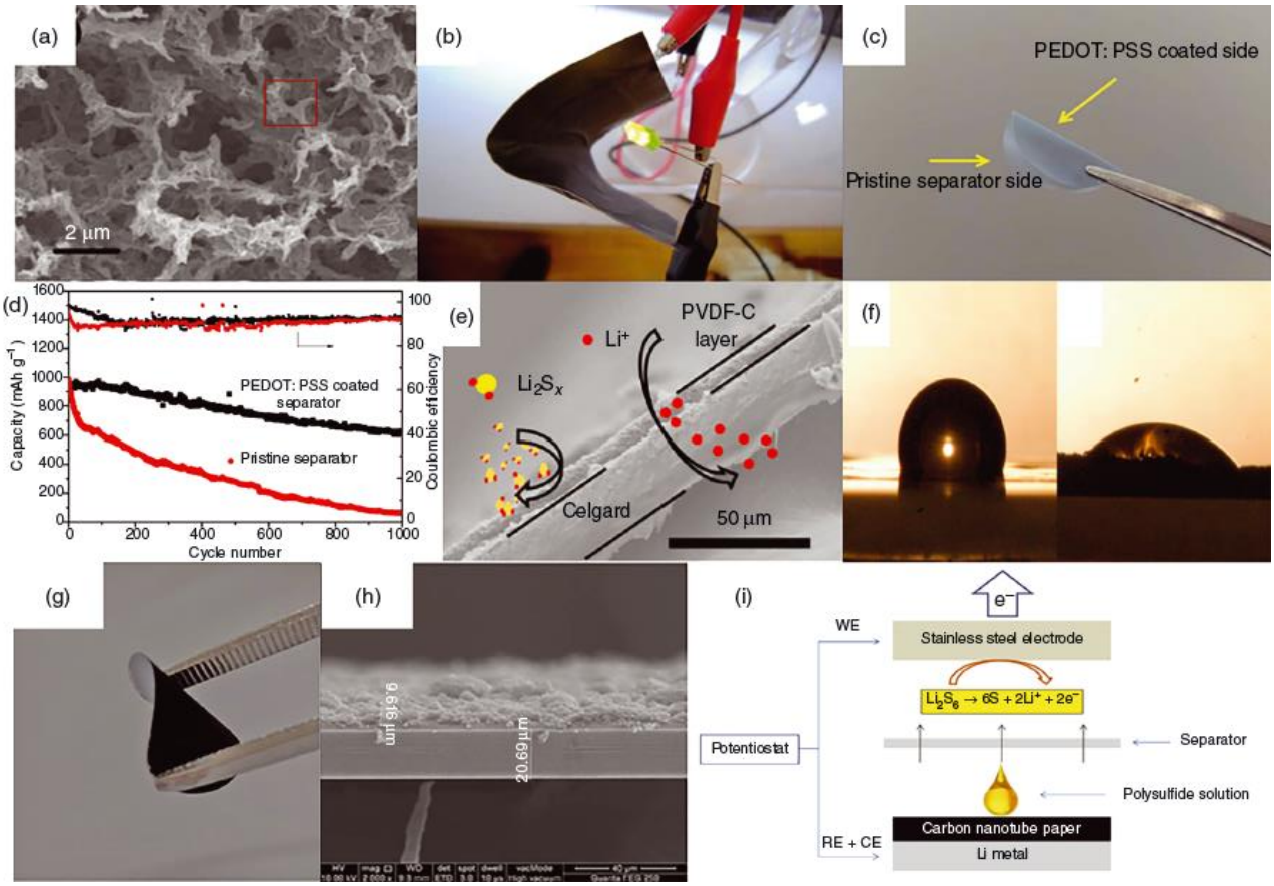

Figure 2.8 (a) The porous structure of a graphene-modified separator [75]. (b) The flexibility of a Li–S battery using the separator and metal Li as anode material. (c) The flexibility of the separator. (d) Schematic diagram of a modified Celgard™ separator restricting the polysulfide migration while maintaining good lithium ion transportation. (d) Comparison of hydrophilic separator (before and after modification).[76]. Copyright 2015, Royal Society of Chemistry. (g, h) The structure of the modified membrane [10]. (i) The schematic diagram of the experimental battery.[77]. Copyright 2015, Elsevier B. V.

2.5 Summary

In this chapter, we discussed the development of flexible Li–S batteries, including cathode

materials, electrolytes, and separators. Carbonaceous materials are widely used as cathode hosts for flexible Li–S batteries. In particular, graphene and CNTs were intensively applied as flexible cathodes for Li–S batteries. However, carbonaceous materials cannot obtain the same enhancement as lithium ion batteries because of their nonpolar characteristics. Heteroatom doping is a good approach, which can not only strengthen the affinity between sulfur and carbon materials but also provide many active sites for anchoring polysulfides. Applicable electrolytes and separators are needed for flexible Li–S batteries. In general, SPEs or GPEs are required to avoid leakage during bending for flexible Li–S batteries. The modification of separators can significantly enhance the performances of flexible Li–S batteries. With the successful fabrications of flexible sulfur cathodes, electrolyte membranes, and modified separators, high-performance flexible Li–S batteries can be fully developed for powering flexible and wearable electronic devices.

Chapter 3 Experimental section

3.1 Overview

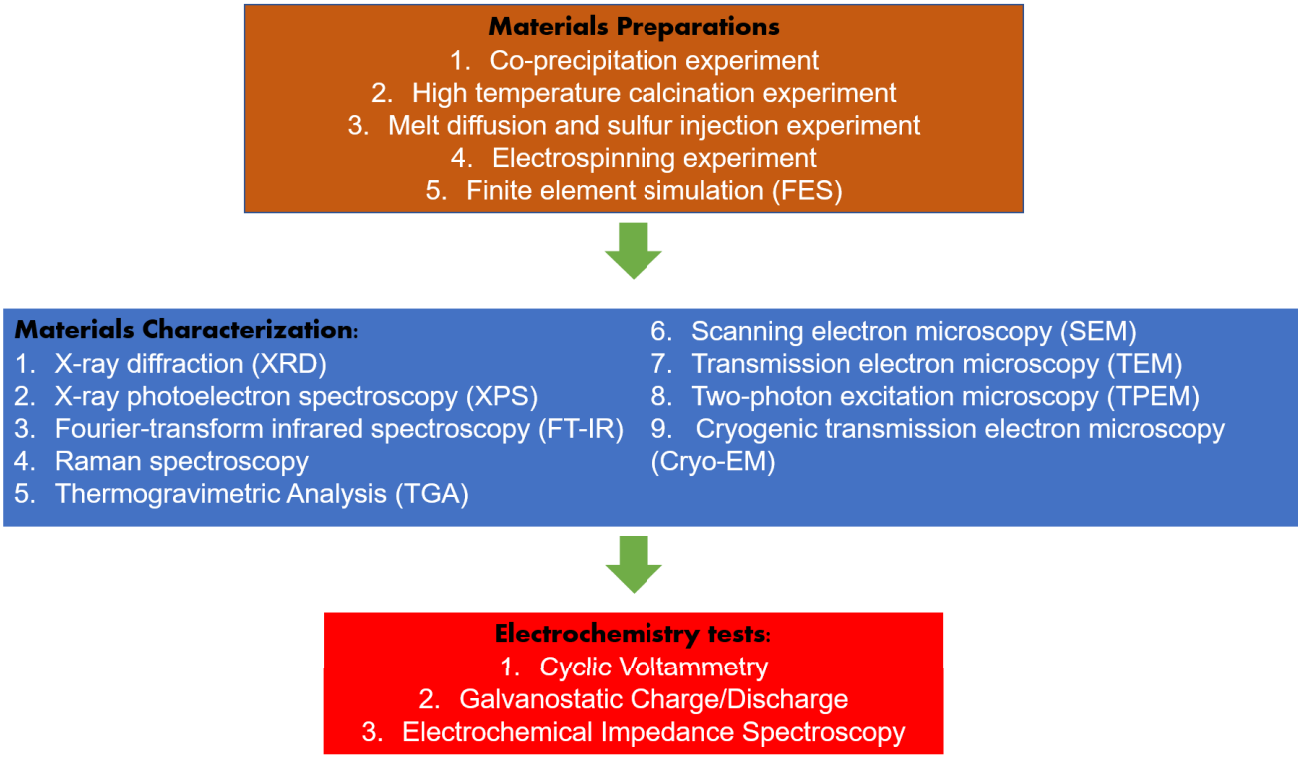

Figure 3.1 The diagram that demonstrates procedures of the experiment.

Figure 3.1 summarizes the materials preparation, materials characterization, and electrochemical test methods utilized in this thesis. Generally, the materials in this thesis are usually prepared by co-precipitation method, high temperature calcination, Sulfur loading, electrospinning methods. Additionally, all the chemicals related to this work are listed in **Table 3.1**

Table 3.1. Chemicals details in the research project.

Chemicals	Formula	Purity	Supplier
Carbon additive (carbon black)	C	100%	Sigma-Aldrich
Poly(vinylidene difluoride) (PVDF)	$(CF_2CF_2)_n$	99%	Sigma-Aldrich
Sulfur	S	99%	Sigma-Aldrich
Ethanol	CH_3CH_2OH	95%	Chem Supply

Ethlyene carbonate (EC)	$(CH_2)_2CO_3$	99%	Sigma-Aldrich
Graphite (natural flakes)	C	75%	Sigma-Aldrich
Hydrochloric Acid	HCl	37%	Fisher Scientific
N-methyl pyrrolidinone (NMP, anhydrous)	C_5H_9NO	99.50%	Sigma-Aldrich
Lithium foil	Li	100.00 %	Hohsen Corporation Japan
Polypropylene separator	-	-	Celgard
Bis(trifluoromethane)sulfonimide lithium salt (LiTFSI)	$CF_3SO_2NLiSO_2CF_3$	99%	Sigma-Aldrich
Cerium Chloride	$CeCl_3$	99%	Sigma-Aldrich
Potassiu hexacyanoferrate (II) trihydrate	$K_4Fe(CN)_6$	98%	Sigma-Aldrich
Fibroin		99%	SiMeiTe
8-Anilino-1-Naphthalenesulfonic acid	$C_{16}H_{13}NO_3S$	99%	Aladdin
Cu foil	Cu	99.90%	Miyao
Lithium titanate (LTO)	Li_2TIO_3	99.90%	Sigma-Aldrich

Most characterization of precursors and prepared materials, such as X-ray diffraction (XRD)m X-ray photo electron spectroscopy, Raman spectroscopy, thermogravimetric analysis (TGA), Scanning electron microscopy (SEM), and transmission electron microscopy (TEM), confocal laser scanning microscopy (CLSM) and cryogenic transmission electron microscopy (Cryo-EM), etc. are conducted.

Most electrochemical impedance spectroscopy are performed to investigate the electrochemical performance of the as assembled Li-S batteries. Furthermore, some samples for XPS depth profiling and Cryo-EM are conducted after the electrochemical characterization.

3.2 Material preparation

3.2.1 Co-precipitation experiment.

Co-precipitation is a kind of important method to prepare composite oxide ultrafine powder containing two or more metal elements, which contains two or more kinds of cations in the solution and exists in the solution as homogeneous phase. After the coprecipitation reaction, homogeneous precipitation of various components can be obtained by adding precipitant. In chapter 4, the precursor was prepared by coprecipitation and then aged for 48 hours to obtain homogeneous lattices.

3.2.2 High temperature calcination.

Calcination is a kind of thermal treatment process in the absence or limited supply of air or oxygen applied to prepare carbonaceous materials. During the process of high temperature, some typical metal nano crystals (such as Fe or Fe_3C) can play the role of catalyst to pyrolysis the carbon substrate. High temperature calcination in inert environment has been widely applied for preparing carbon nanotubes (CNTs), graphene and hard carbon, etc. Furthermore, adding sulfur, nitrogen or phosphorus rich additives to the precursors has been regarded as an effective doping method, which can greatly improved the electrochemical performance of carbonaceous materials. In chapter 4, high temperature calcination of employed to prepare the carbonaceous cathode materials of Li-S batteries.

3.2.3 Melt diffusion and sulfur injection experiment.

In this thesis, the sulfur loaded cathode materials are prepared by melt diffusion method. At standard atmosphereic pressure, the melting point of sulfur is 155 ºC. Specifically, the Sulfur powder

(99.99%, Sigma-Aldrich) and the prepared host material are homogenously mixed and grinded with a certain ratio. Then, the mixture is heated under a temperature of 155 ^{o}C. So that the liquid sulfur can siphoned into the nanostructure of carbonaceous structures.

3.2.4 Electrospinning experiment.

Electrospining method is a kind of universe technology for preparing ultrafine wires. This method uses electric force to draw charged threads from polymers solutions or polymer melts up to fibers, where the diameter of the fiber can be hundreds of nanometers. By changing the concentration, viscosity, propelling speed and electric field strength, the spinning thickness, micro nanostructure of fibers can be manipulated. When cooperates with calcination, electrospinning is also a popular method for preparing nanocarbon nanofibers. Until now, electrospinning method has been widely used in textile, tissue engineering, medicine biology and energy storage domains. In chapter 5, electrospinning is employed to fabricate the bio-interlayer for protecting Li-metal anodes.

3.2.5 Finite element simulation (FES)

FES is a useful tool to analyze the effect of the forming condition. FES uses the mathematical approximation method to simulate the real physical system (geometry and load cases). According to using simple and interactive elements, a real system with infinite unknows can be approximate by finite number of elements. In this thesis, COMSOL simulation was employed to conduct the FES to investigate the distribution of electric field on tips of Li dendrites (chapter 5).

3.3 Characterization methods

3.3.1 X-ray powder diffraction (XRD)

XRD is a rapid and general analytical technique employed for phase identification of a crystalline

material and specifically, support details about unit cell dimensions, phases, preferred crystal orientations and other structural parameters, such as average grain size, crystallinity, strain and crystal defects. XRD peaks are produced by constructive interference of a monochromatic beam of X-rays scattered at specific angles from each set of lattice planes in a sample. In this thesis, XRD was utilized to analysis the components and lattice structure of cathodes of Li-S batteries.

3.3.2 X-ray photoelectron spectroscopy (XPS)

XPS is an important surface chemical analysis technique that have been widely used to analyze the surface chemistry of materials, especially for measuring the element composition and determines the binding states. The average detection depth of XPS is 10 nm. In this thesis, XPS was employed to analyze the chemical environment of cathode material and electrolyte interphase layer of Li anodes.

3.3.3 Fourier-transform infrared spectroscopy (FT-IR)

FT-IR is a technique which is employed to obtain infrared spectrum of absorption, emission, and photoconductivity of slide, liquid, and gas. FT-IR uses the mathematical process (Fourier transform) to translate the raw data (interferogram) to the actual spectrum and has been widely used to analyze structure of organic material and investigate functional groups. In this thesis, FT-IR was used to characterize the secondary structure of bio-interlayer for protecting Li metal anodes.

3.3.4 Raman spectroscopy

Raman spectroscopy is an useful non-destructive analysis method which can support detailed information about phase, chemical structure, molecular interactions, polymorphy and crystallinity. The mechanism of Raman spectroscopy is based on the interaction between the light and the chemical bonds of the material. A Raman spectrum features a number of characteristic peaks, indicating the intensity and wavelength position of the Raman scattered light. Each peak corresponds to a specific

molecular bond vibration, including individual bonds and groups of bonds. In this thesis the Raman spectroscopy was used to characterize the graphitization degree of cathode materials of Li-S batteries.

3.3.5 Thermogravimetric Analysis (TGA)

TGA is an analytical technique used to investigate the material's thermal stability and its fraction of volatile components by monitoring the weight change that occurs as a sample is heated at a constant rate. In this thesis, TGA was conducted to measure the sulfur content ratio in cathode materials of Li-S batteries.

3.3.6 Scanning electron microscopy (SEM)

SEM is designed for directly study the surfaces of solid objects, that utilizes a beam of focused electron of relatively low energy as an electron probe that is scanned in a regular manner over the specimen. The action of the electron beam stimulates emission of high-energy backscattered electrons and low-energy secondary electrons from the surface of the specimen. In this thesis, SEM was conducted to monitor morphologies of cathode materials and the surfaces of electrodes and separators.

3.3.7 Transmission electron microscopy (TEM)

TEM is a microscopy technique in which a beam of electrons is transmitted through a specimen to form an image. The specimen is most often an ultrathin section less than 100 nm thickness or a suspension on a grid. HRTEM is often employed to observe the internal structure and lattice structure. In this thesis, TEM was employed to characterize the lattice structure of material and measure the interspace of sulfur loading scaffolds (chapter 4).

3.3.8 Two-photon excitation microscopy (TPEM)

TPEM is a kind of fluorescence imaging technique which allows imaging of lying tissue up to a depth of one millimeter. Be different from other traditional fluorescence microscopy, in which that

excitation wavelength is shorter than the emission wavelength, TPEM requires simultaneous excitation by two photons with longer wavelength than the emitted light. In this thesis, TPEM was employed to analyze the distribution of biomolecules immobilized on the Li metal anode (chapter 5).

3.3.9 Cryogenic transmission electron microscopy (Cryo-EM)

The Cryo-EM method applied on samples cooled to cryogenic temperatures and embedded in an environment of vitreous water. Compared with the traditional high-resolution TEM, the Cryo-EM can protect the structure of the fragile sample from high temperature damage. Cryo-EM has been widely applied in the field of biochemistry, especially in the three dimensional reconstruction of protein molecules. Recently, Cryo-EM has been also utilized in the field of other nanotechnologies. In chapter 5 of this thesis, Cryo-EM was employed to characterize the conjunction between biomolecules and Li metal surface to avoid the damage on both of them.

3.4 Preparation procedure of electrodes and assembly of batteries

3.4.1 preparation of electrodes.

In this thesis, electrodes are prepared by classic painting method. Specifically, the synthesized material, binder (PVDF for cathodes and CMC for anodes) and conductive carbon black in the mass ratio of (8:1:1). After adding corresponding solvents (NMP for cathodes and deionized water for anodes), the slurry was stirred and treated by ultrasonic alternatively for 12 h. A scraper with the thickness of 200 μm was used to simultaneously paint the slurry on the metal collector (Al foil for cathodes and Cu foil for anodes). The mass loading of active materials was about 1~2 mg cm^{-2}. The prepared electrodes are heated in high temperature (60 ºC for sulfur cathodes and 120 ºC for LTO anodes) in a vacuum environment. When the temperature of electrodes calmed down to ambient

temperature, the electrode was cut into small discs with a diameter of 12 mm. Finally, small disks were press into electrodes by tablet machine.

3.4.2 Battery assembly

The electrochemical measurement of batteries were carried out by two-electrodes system. The CR2032-type batteries were assembled in an argon filled glove box where has a high level of isolation from water and air (O_2 < 0.1ppm, H_2O < 0.1ppm). For lithium based half battery tests, the as prepared battery was assembled in the order of cathode shell, cathode electrode, Celgard 2400 separator, anode electrode, stainless steel pad, battery spring pad and anode shell. The electrolyte used in the thesis is 1 M LiTFSI in 1,2-dioxolane (DOL)/dimethoxymethane (DME) (1:1, v/v) with 1 % $LiNO_3$ as additive.

3.5 Electrochemical performances

In this thesis, electrochemical performances were investigated by cyclic voltammetry (CV), galvanostatic charge/discharge and electrochemical impedance spectroscopy (EIS) techniques.

3.5.1 Cyclic Voltammetry (CV)

CV is a typical potentiodynamic electrochemical measurement. In CV, the electrode potential ramps linearly versus time in cyclical phases. In this thesis, the electrochemical workstation (VMP3 or CHI 660D) applies a potential on the electrochemical cell and monitor the current during the test. If there are some redox reactions appeared on the surface of the electrode, the corresponding redox peaks can be found on the CV curve. CV curves can demonstrate details about the reaction process of batteries during discharge/charge cycling and reflect the stability of it at scanning rates.

3.5.2 Galvanostatic Charge/Discharge

In this thesis, galvanostatic charge/discharge is conducted on Neware battery testing system and CHI workstation. During the test, a constant current was applied within a certain voltage window. The

specific discharge/charge capacity (Q, mAh g-1) is calculated by the equation (3-1):

$$Q = I * t \tag{3-1}$$

Where t is the time of galvanostatic charge/discharge (unit: h) and I is the current density (unit: mA g-1). Rate performance was achieved by applying different current densities to find out the relationship between current and specific capacities. When the galvanostatic charge/discharge was cycled for numerous time, the cycling stability of the battery was tested. Discharge/charge capacity, rate performances, cycling stability are important for judging batteries.

3.5.3 Electrochemical Impedance Spectroscopy (EIS)

EIS is an important electrochemical characterization technique to study the transduction in batteries. The Ohmic resistance R_Ω (or bulk resistance R_b) indicates the sum of the resistances of separator, electrolyte and contact of electrodes. The RCT radius of semi-circle in the high frequency area corresponds to the resistance of solid electrolyte interface (SEI) layer (which can be broken and regenerated during the cycling) and the resistance of charge transfer at the electrolyte/electrode interface. The angle of straight line at low frequencies corresponds to the Warburg resistance (W) which represents resistance to mass transfer, or diffusion control.

Chapter 4 Biomimetic 3D Fe@CeO_2 decorated N-doped Carbon nanotubes architectures for high-performance Lithium-Sulfur batteries

4.1 Introduction

Lithium-sulfur (Li-S) batteries are widely regarded as a new generation high energy rechargeable battery system for its high theoretical specific capacity (1675 mAh g^{-1}) and low cost of sulfur [78-80]. However, the practical applications of Li-S batteries is still hindered by several challenges. These

include the poor electrical conductivity of sulfur [81, 82], large volumetric expansion (≈ 80 %) during transformation between S_8 (2.03 g cm^{-3}) and Li_2S (1.66 g cm^{-3}), and shuttle effect of dissolved polysulfides [83]. To keep both chemical and physical stabilities of cathode electrodes, sulfur-host materials must be flexible enough to bear large expansion and compression stresses [84-86]. These issues cause irreversible capacity degradation and poor cycling performance. One of the most effective approaches is to design cathode host materials with strong chemical binding interactions toward polysulfides to eliminate the shuttle effect [87-90].

In order to alleviate the large volumetric expansion (up to 80 %) during the lithiation process and improve the electric conductivity of sulfur cathodes, hollow morphologies have been widely employed to instore and immobilize sulfur [91-94]. In 2019, Husein *et al.* reported a kind of hollow multi-shelled structural TiO_{2-x} with multiple spatial confinements for long-life Li-S batteries [95]. In 2018, Mao *et al.* systematically concluded the recent progress in sequential templating approach to create hollow multishelled structures [96]. As a typical 1D material, carbon nanotubes (CNTs) show outstanding mechanical toughness, high surface-to-volume ratio, and superb electronic conductivity [97]. In 2017, Liu *et al*. synthesized a kind of CNT-treaded N-doped porous carbon film as binder-free electrode for high capacity supercapacitor and Li-S battery [98]. Zhu *et al*. prepared interconnected carbon nanotube/graphene (CNT/GE) nanosphere scaffolds as a free-standing paper electrode and found that this special morphology could keep unique stability to improve sulfur utilization rate up to 81% at 0.19 mA cm^{-2} [99]. However, due to the limited interior space and weak architecture, most original CNTs cannot guarantee a high percentage loading of sulfur in their structures and are easily collapsed due to the internal stress [100].

Biomimetic materials have been extensively investigated for many functional applications owing

to the complex structure and intriguing properties [101]. In particular, biomimetic materials can endow Li-S batteries with more benefits because they can accommodate more sulfur into their specific architecture [102]. For example, Ai *et al*. reported a category of biomimetic ant-nest electrode structure for high sulfur ratio Li-S batteries in 2016. This special interior-linked architecture achieved a high sulfur loading of 85% and promises good transportation of Li ions [103]. Thereafter, many novel biomimetic structures such as fish scale-like nanotiles morphologies start to emerge subsequently [104]. Su *et al*. achieved Fe_3C-graphene (GE)-CNTs 3D scaffold material by a simple method [105]. They figured out the existence of Fe_3C could not only catalyze the growth of CNTs but also hinder the dissolution of polysulfides when used as electrode materials in Li-S batteries. The similar 3D hollow scaffold structures have also been widely recognized as good cathode matric materials for Li-S batteries [106, 107].

Herein, we report the fabrication of a series of marine-organism-like 3D nitrogen-doped carbon nanotube architecture using Fe/Ce-PBA as the precursor. Being different from original CNTs, the as-prepared biomimetic CNTs have large interior space decorated with Fe and CeO_2 nanoparticles. To keep a high level of nitrogen doping (5%) after calcination, we purposely compensate melamine as a supplementary nitrogen source. By varying the amount of melamine and calcining temperatures, the morphologies of 3D Fe/CeO_2-CNTs scaffold can be directly controlled (from “seaweeds” to “sea anemones”, “sea cucumber” and even “rocky seabeds” respectively). When tested as a cathode material for Li-S batteries, the first discharge capacity of sea cucumber-like CNTs scaffold attained 1241 mAh g^{-1} at 0.2 C and maintained 1003 mAh g^{-1} after 100 cycles. This superior electrochemical performance could be attributed to its unique hollow architecture with the decoration of iron and cerium elements. The capacious interspace of sea cucumber-like 3D CNTs scaffold can enable high

percentage loading of sulfur and bear massive volumetric expansion during charge/discharge cycles. Furthermore, the presence of double metal elements (Fe and Ce) facilitates the redox reaction between sulfur and polysulphides as confirmed by the *ex-situ* XPS analysis. This work opens a new avenue to design novel biomimetic architecture for developing high-performance Li-S batteries.

4.2 Experiment section

4.2.1 Synthesis of Fe/CeO_2-CNTs Hybrids:

$Ce[Fe(CN)_6]$ was obtained by hybridizing $CeCl_3$ and $K_4[Fe(CN)_6]$. Specifically, 3 M $CeCl_3$ were added into 3 M $K_4[Fe(CN)_6]$ sequentially. The slurry was left undisturbed for 48 h for aging, followed by vacuum filtration. The collect powder was washed with water and ethanol 3 times. After coating with melamine, precursors were annealed at 900 ^oC (N_2 environment) for 4 h with a heating rate of 5 $^oC\ min^{-1}$. After cooling to ambient temperature (cooling rate was 5 $^oC\ min^{-1}$), the final product was obtained. To analyze the formation details, $Ce[Fe(CN)_6]$ was hybridized with melamine at different ratios (3:1, 2:1, 1:1 and 1:2).

4.2.2 Synthesis of S/Fe/CeO_2-CNTs hybrids:

The sulfur loading was realized by the melt-diffusion strategy. Typically, 20 wt% Fe/CeO_2-CNTs and 80 wt% sulfur were mixed. Then, the mixture was moved into a PTFE reactor and heated to 155 ^oC. The composition was kept at that temperature overnight.

4.2.3 Structural and Physical Characterization:

The phase and crystal details of the reaction products were characterized by XRD (Siemens D5000) using Cu Kα radiation with a scanning step of $0.01^o\ s^{-1}$. The morphology of the material was observed and characterized by SEM (Zeiss Supra 55VP). The crystal and intrinsic details were

observed by HR-TEM (JEOL JEM-2011). Elemental mapping was obtained by energy-dispersive X-ray spectroscopy (Bruker SDD EDS Quantax 400 system). Thermogravimetric/differential thermal analysis was performed at a heating rate of 50 ^{o}C min^{-1} under N_2 flow from ambient temperature to 900 ^{o}C with a 2960 SDT system (Lukens Drive New Castle DE 19720). Raman spectra were measured by Renishaw in Via Raman spectrometer system (Gloucestershire UK) equipped with a Leica DML Bmicroscope (Wetzlar, Germany) and a 17 mW at 633 nm Renishaw helium neon laser source. XPS measurements were carried out on a Kratos XSAM-800 spectrometer with an Mg Kα radiation source.

4.2.4 XPS characterization:

Before the XPS characterization, the Li-S battery was cycled for 15 cycles and discharged to 1.7 V. The coin cell was disassembled in the glove box and the electrode was washed by DOL and then dried in a vacuum chamber. During the transportation, the sample was kept in an Ar gas full-filled centrifuged tube and all XPS results have been calibrated with carbon C-C (284.8 eV).

4.2.5 Electrochemical Testing:

the active electrodes consisted of 80 wt% as-prepared composite material, 10 wt% acetylene carbon black, and 10 wt% poly(vinylidene fluoride) binder (PVDF, $(CH_2CF_2)_n$, Sigma-Aldrich) in N-methyl-2-pyrrolidone (NMP, C_5H_9NO, Sigma-Aldrich 99.5%) to form a slurry, and the slurry was then pasted onto aluminum foil and dried in a vacuum oven for 12 h, which was followed by pressing at 200 kg cm^{-2}. The mass loading of each low sulfur loading electrode was approximately 1.1 mg cm^{-2} and 4.2 mg cm^{-2} of high sulfur loading electrode. Electrochemical measurements were carried out using CR2032 coin cells with lithium foil as reference and counter electrode and a porous polypropylene (Celgard 2300) as the separator. CR2030 coin cells were assembled in an argon-filled glove box (Unilab, Mbraun, Germany) with low levels of H_2O and O_2 ($H_2O < 0.1$ ppm, $O_2 < 0.1$ ppm).

The electrolyte solution was 1 M LiTFSI and 1 wt% $LiNO_3$ in 1, 3-dioxolane and 1, 2-dimethoxyethane (volume ratio 1:1). For low sulfur loading electrodes, 30 µl electrolyte was employed and for high loading electrode, the usage of electrolyte is 50 µl. The galvanostatic charge-discharge measurements were performed at room temperature at different current densities in the voltage range from 1.7 to 2.8. CV was carried out on a CHI 660 C electrochemistry workstation with a scan rate of 0.1 mV s^{-1} from 1.7 to 2.8 V.

4.3 Results and discussion

Figure 4.1a shows the synthesis process for the Fe/Ce-CNTs composite. In the first step, $Ce[Fe(CN)_6]$ PBA nanoplates were simply prepared by a condensation procedure. Specifically, $CeCl_3$ aqueous solution was added into 3 M $K_4[Fe(CN)_6]$ solution under strong stirring. After aging for 48 h, homogeneous $Ce[Fe(CN)_6]$ nanoplate clusters were obtained. Scanning electron microscopy (SEM) images of $Ce[Fe(CN)_6]$ nanoplates (**Figure 4.1 b** and **Figure 4.2**) shows that all nanoplates are loosely bound together with an average size of 100 nm × 300 nm × 30 nm. After coating with melamine, the precursor was annealed at 900 ºC in a nitrogen gas atmosphere for 3 h. **Figure 1 c** reveals that the annealed products have a typical hierarchical architecture consisting of interconnected hollow CNTs. The average diameter of the CNTs is around 80 nm, where most catalytic Fe particles are pushed to tips of CNTs [108, 109]. According to the XRD patterns, Fe (JCPDS No. 00-043-1002) and CeO_2 (JCPDS No. 00-007-9753) can be identified and indexed (**Figure 4.3**).

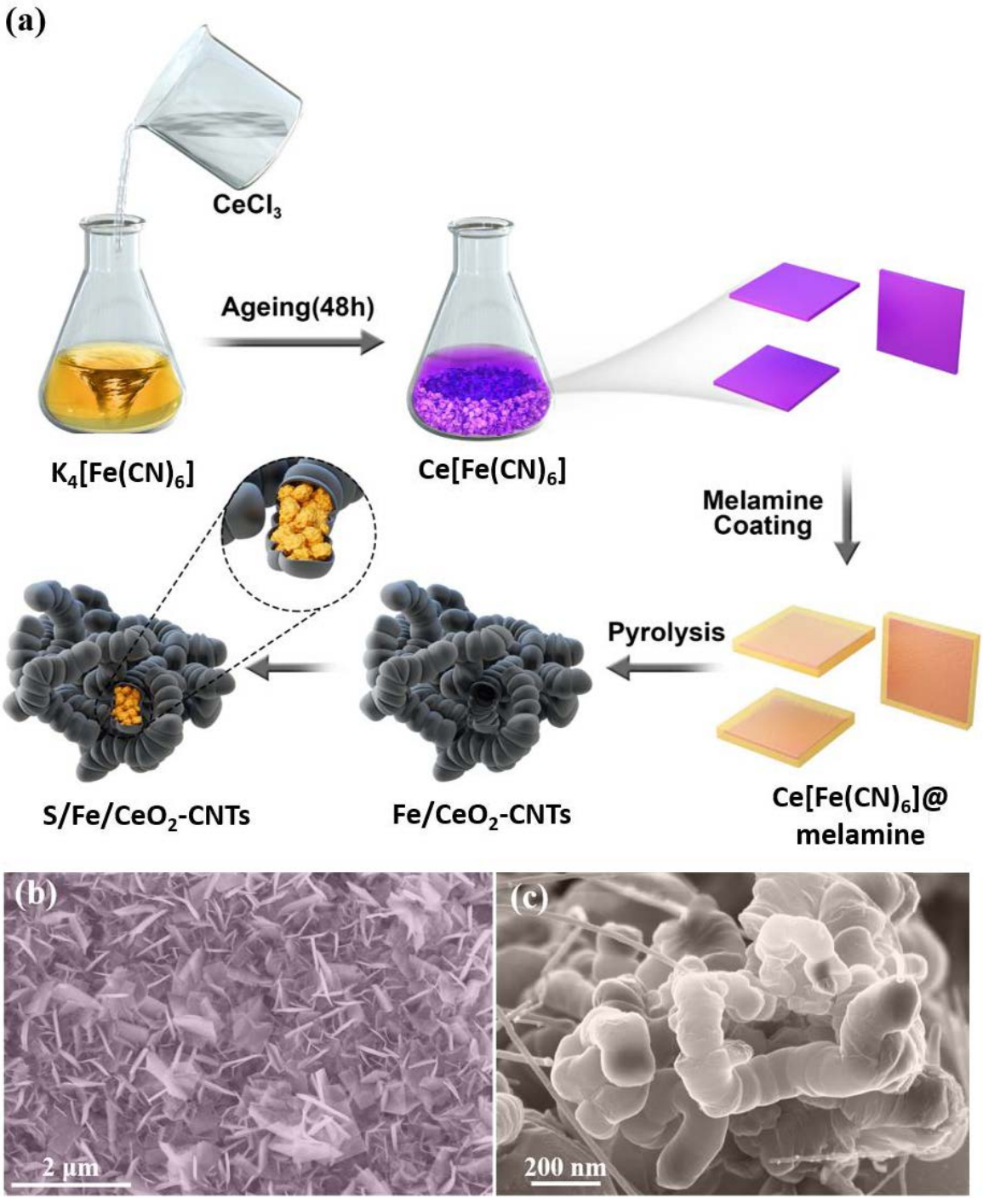

Figure 4.1. **(a)** Illustration of the synthesis process for preparing Fe/CeO_2-CNTs hybrids. (**b)** SEM images of precursor Prussian blue analog nanosheets. (**c)** SEM images of the typical Fe/CeO_2-CNTs structure after annealing at 900 ^oC.

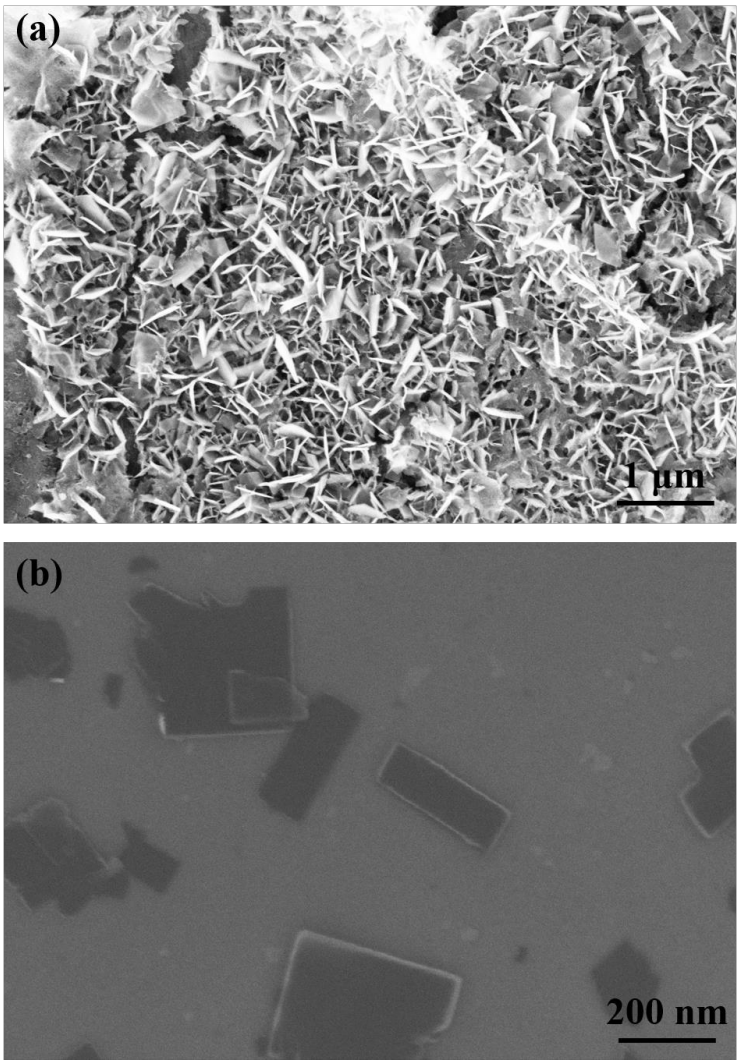

Figure 4.2 SEM images of $Ce[Fe(CN)_6]$ precursor nanoplates before calcination.

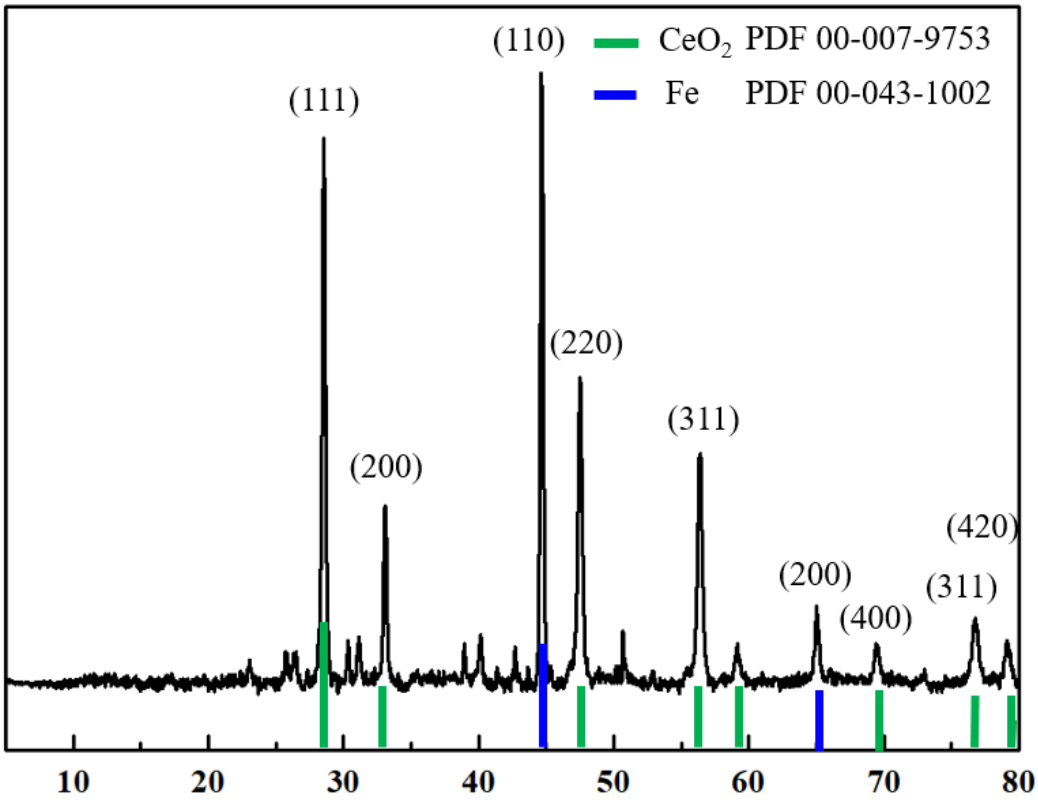

Figure 4.3 The pattern of X-ray diffraction data of Fe/CeO_2-CNTs hybrids.

By changing the ratio of PBA and melamine, the morphologies of Fe/CeO_2-CNTs could be effectively manipulated. As shown in **Figure 4.4**, when the ratio was 3 : 1, seaweed-like CNTs can be obtained. However, when we increased the proportion of melamine, the length of were CNTs shortened while the diameter increased to 200 nm (**Figure 4.4 g,h**). The annealed 3D scaffold composite was converted to 3D CNTs, which mimic the morphology of hollow sea cucumbers. Consider to sulfur loading, a large inner space is generally desired to accommodate more sulfur. It should be noted that these sea cucumber-like CNTs are wrapped around on their substrates, which are similar to real sea cucumbers attached to the rocks of the seabed (**Figure 4.4** g,h). The growing process of CNT from these PBA precursors are similar to our previous research (Fe_3C-graphene (GE)-CNTs) [105]. At high calcinating temperature (above 800 °C), the $Ce[Fe(CN)_6]$ sheet precursors start to form Fe/CeO_2 hybrid

catalyst while the graphitic lattice starts to nucleate on the surface of Fe/CeO_2 catalyst. Initially, the carbon cap appears to replicate the profile of catalyst particle, then, the carbon network extended by lifting off from the catalyst particle surface, which itself is thereby restructured. During the growing process of CNT scaffold, both PBA precursor and melamine provide source of carbon. Accompanied with carbon nanotubes catalyze process, the growing CNT forces its shape onto the Fe/CeO_2 particle, thereby constrains the particles to a more cylindrical shape. When the tangential graphitic lattice encapsulates the catalyst particle, CNT growth will be terminated. To further investigate the influence of PBA : melamine ratio to morphologies of CNTs 3D structure, we prepared composites with the different proportion of melamine (3 : 1, 2 : 1, 1 : 1 and 1 : 2). As shown in **Figure 4.4**, these composites showed various morphologies, corresponding to some marine plants such as seaweed, sea anemone, sea cucumbers and bare seabed, respectively. Accompanied by the increased proportion of melamine, the interspaces of CNTs were expanded while the length was obviously shortened. In 2012, Tuaev *et al*. reported that surface heteroatoms, such as nitrogen, can mediate the enhancement of catalyst of carbon materials and even suppress their growth. Different from the traditional chemical vapor deposition (CVD) method, the catalytic efficiency of the direct pyrolysis method is not as high as that of CVD, which can be blamed on the increase of defects caused by abundant nitrogen source from melamine.[110] When the ratio was set to the opposite extreme (1 : 2), there were almost no CNTs observed. This comparison suggested that the coating of melamine layer can largely suppress the growth of CNTs and increase their diameters. According to the previous reports, a suitable level of nitrogen doping can effectively improve the electrochemical properties of Li-S batteries due to chemical binding towards polysulfides [84, 111]. Meanwhile, the enlarged hollow architecture can maximize the sulfur loading and thus increase their specific capacity [112].

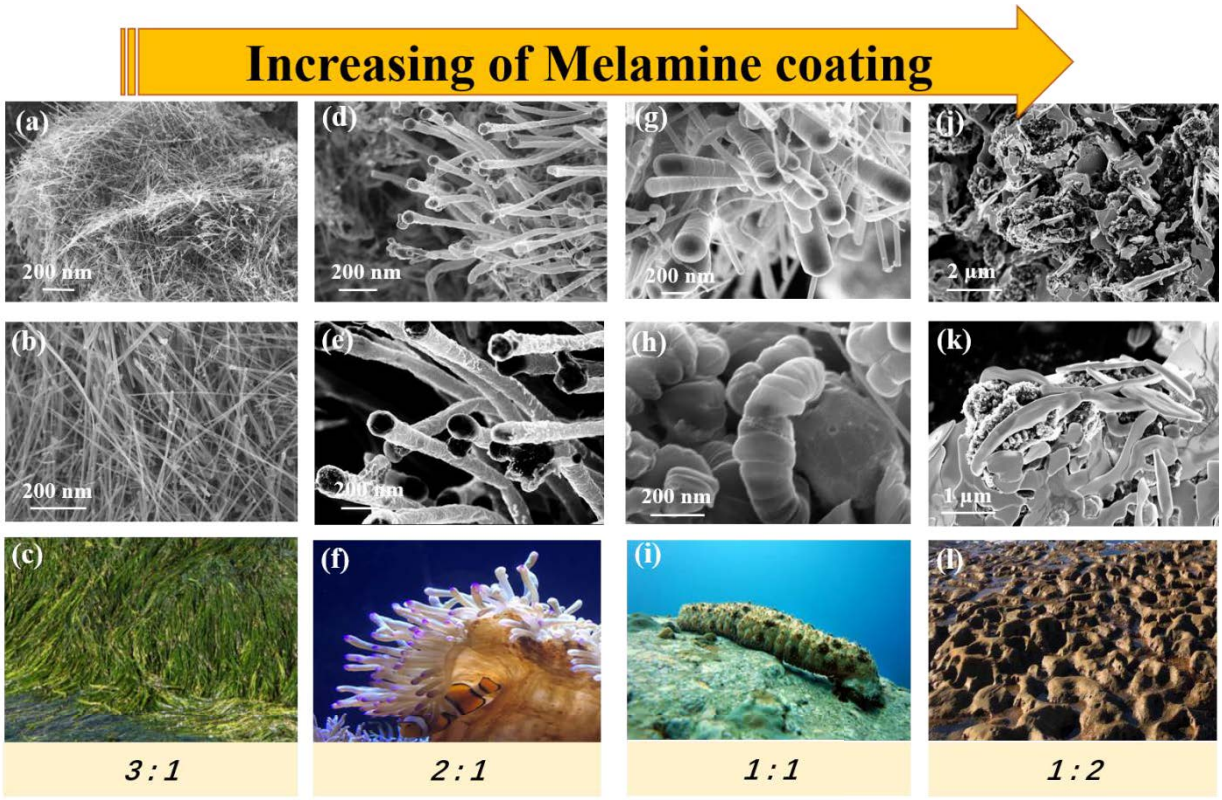

Figure 4.4 Comparison of 3D Fe/CeO_2-CNTs hollow structures by changing the ratio of PBA to melamine. (a & b) Seaweed-like, (d & e) sea anemone-like, (g & h) sea cucumber-like and (j & k) rocky seabed-like Fe/CeO_2-CNTs, corresponding to different ratios of PBA : melamine (3 : 1, 2 : 1, 1 : 1 and 1 : 2).

We also investigated the influence of annealing temperature on their morphological changes. As shown in **Figure 4.5**, when the precursor was sintered at 850 ºC, almost no CNT products were observed because the temperature is not high enough to trigger the growth of CNTs. When the temperature was increased to 900 ºC, the proportion of CNTs growth to near 50 % (**Figure 4.5 b**). When the temperature was further increased to 950 ºC, the conversion efficiency is close to 100% (**Figure 4.5 c**). At this temperature, the CNT growth rate was doubled [105]. This might be attributed to

the participation of Ce. According to previous literature, the presence of Ce can dramatically increase the catalytic efficiency of the Fe-based catalyst and therefore, significantly increase the CNT growth rate [113, 114]. To elucidate the intrinsic details of the 3D scaffold, high-resolution TEM (HR-TEM) characterization was performed. **Figure 4.7 a** shows the features of typical catalyst conjunction with root (the dark section is a catalyst particle whose outline has been drawn by the tip of the CNTs. The root of the catalyst particle (light purple area) (**Figure 4.7 b**) connects to the CNT and orients it towards a junction with root (light yellow area). Furthermore, the growth of CNTs can be illustrated in two schemes. From the typical HR-TEM image (**Figure 4.6 b**), it can be observed that one tip of the CNT has grown from the bottom up, and its catalyst particle was subsequently moved during the growth of the CNT. While on the other side, the catalyst particles remained immobile during the CNT growth. Additionally, we found that the CNTs have 6 to 8 layers and are around 10 nm in wall thickness with 80 nm outer diameter (**Figure 4.7 c**). **Figure 4.7 d** reveals one broken CNT in which the catalyst was exposed (marked in red color, PBA : Melamine = 1:1).

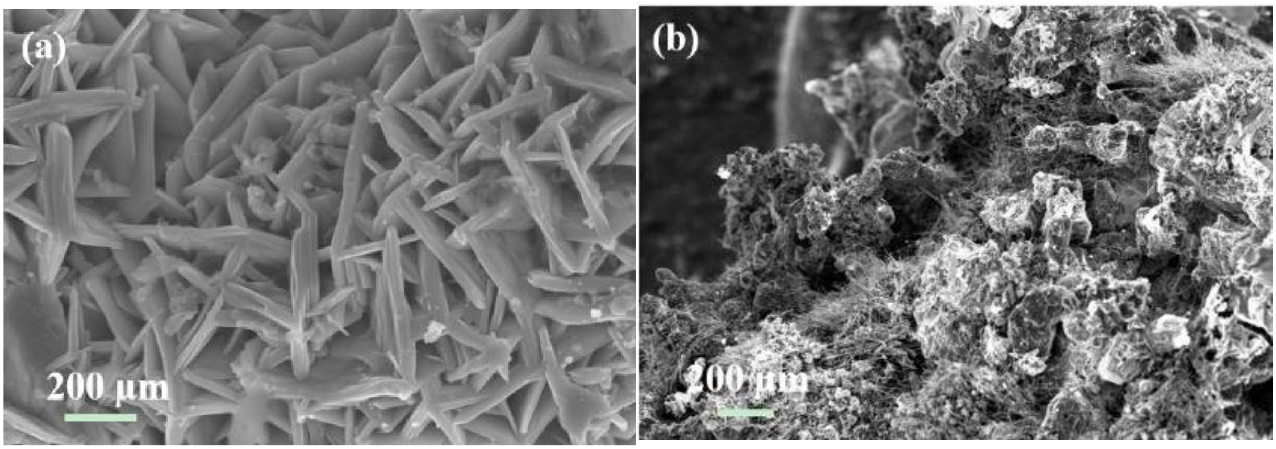

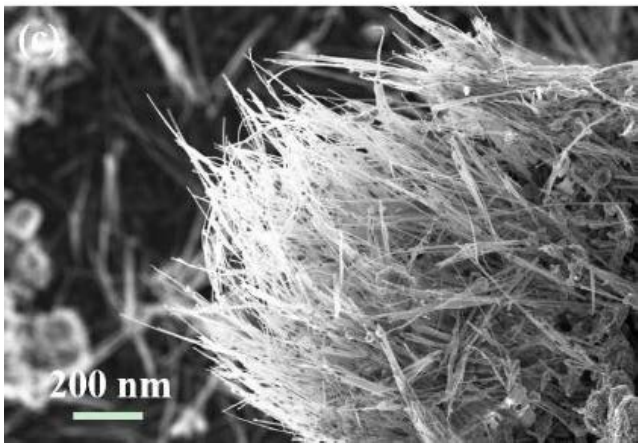

Figure 4.5 Comparison of 3D morphologies of Fe/CeO_2-CNT hybrids calcinated at various temperature: (a) 850 ºC, (b) 900 ºC and (c) 950 ºC.

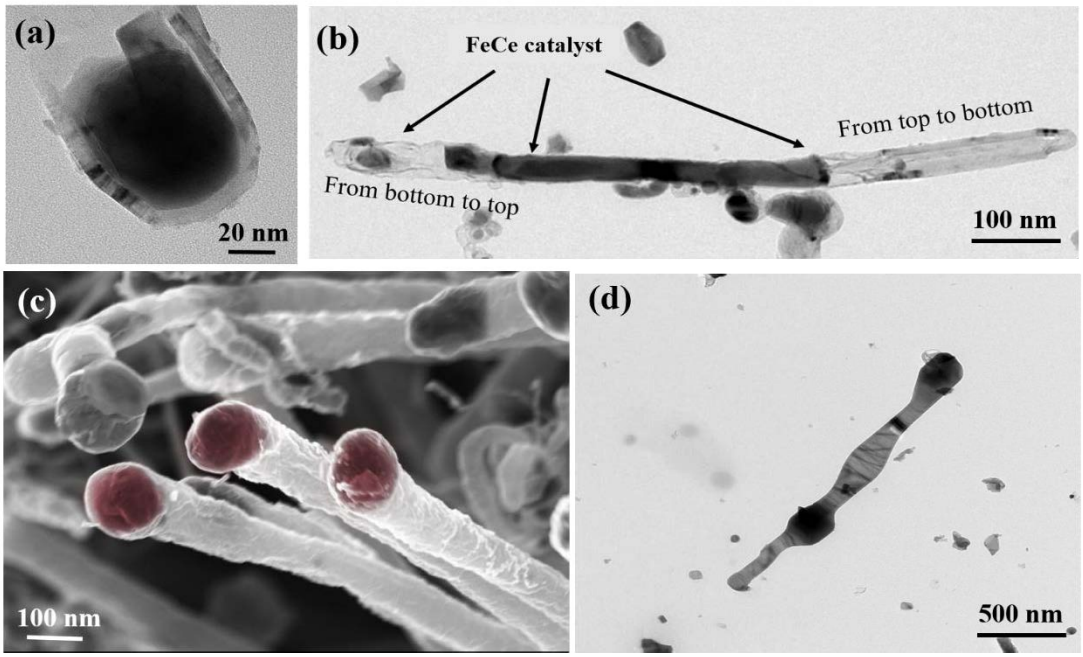

Figure 4.6 (a) HR-TEM image of Fe/CeO_2-CNTs and the specific feature of its catalyst particle. (b) HR-TEM image of one CNT growing by two different growth schemes. (c) A cluster of sea anemone-like CNTs catalyst particles of which have been marked in red color. (d) The TEM image of one sea anemone-like Fe/CeO_2-CNTs.

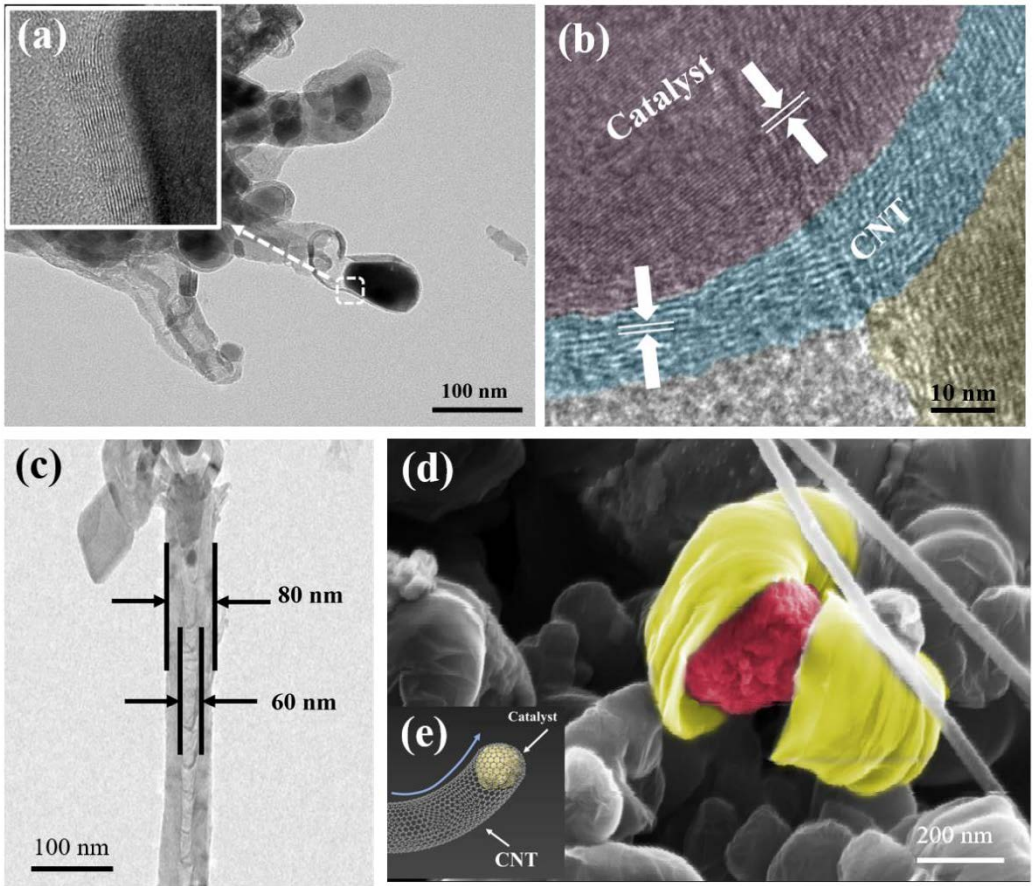

Figure 4.7 (a) The HR-EM image of Fe/CeO_2-CNT and the specific feature of its catalyst particle. (b) HR-TEM image of conjunction between catalyst and carbon nanotube. (c) One TEM image of a hollow CNT (PBA : melamine is 2 : 1). (d) A broken CNT (PBA : melamine is 1 : 1) (yellow) of which its catalyst is exposed (red). (e) The inset is the schematic diagram of CNT growth.

Figure 4.8 a shows Raman spectrum of Fe/CeO_2-CNT composites synthesized with different percentages of melamine. It can be seen that all samples display well-defined D and G bands at 1328 and 1580 cm^{-1}, respectively, indicating a hybridized vibration associated with the E_{2g} vibration of sp^2-bonded carbon atoms [105]. The intensity ratios of I_D/I_G are 0.78, 0.82 and 1.19 for the ratios of PBA: melamine 1:1, 2:1, and 1:2 respectively. This clearly indicates a decreased graphitization feature (**Figure 4.4**). The decrease of intensity also confirms that coating of melamine can extensively

suppress the graphitization, hence reduce the growth ratio of CNT scaffold. Meanwhile, the broad and asymmetric 2D peak at 2700 cm^{-1} implies that the samples mainly consist of inhomogeneous multiwalled CNT rather than single-walled CNTs, which consistent with the HR-TEM observations. Furthermore, peaks at 462 cm^{-1} can be attributed to a symmetrical stretching mode of Ce-O8 vibrational unit, which corresponds to the nanocrystalline of CeO_2 [115] and the additional peak at 660 cm^{-1} can be found in many Fe doped metal oxide which confirms the existence of Fe [106]. The high-resolution XPS spectrum of N 1s peak shows the presence of pyridinic nitrogen (398.7 eV) (**Figure 4.8 b**), confirming the nitrogen doping in the Fe/CeO_2-CNT matrix. The high-resolution XPS spectrum of C1s can be fitted to four peaks at 284.8, 285.7, 286.8 and 288.6 eV, which correspond to C-C, C=N (N-sp^2 C), C-N (N-sp^3) and O-C=O bonds, respectively (**Figure 4.8 c**).

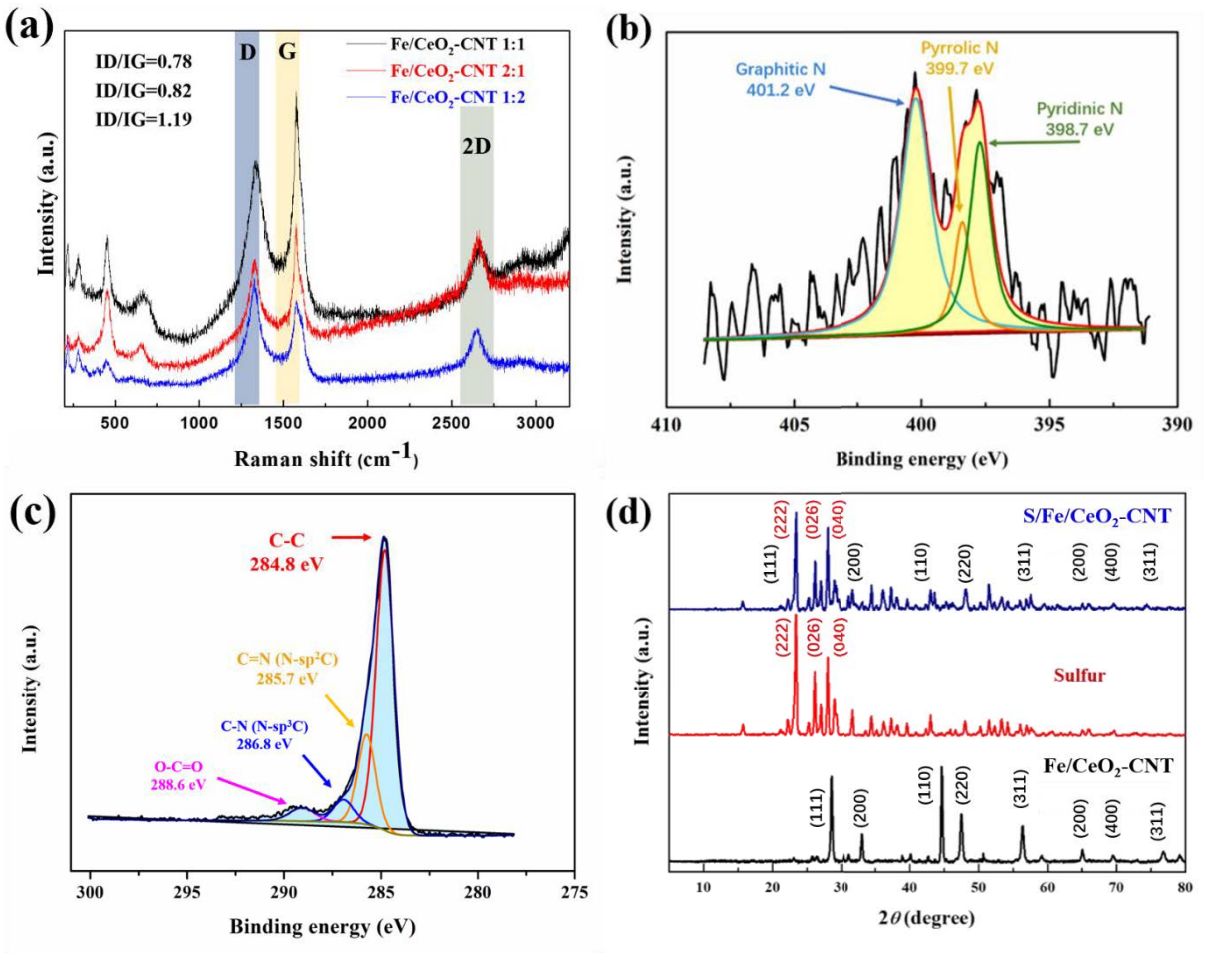

Figure 4.8 (a) Comparison of Raman spectra of Fe/CeO_2-CNTs synthesized with different proportion of melamine. (b) XPS N1s spectrum of Fe/CeO_2-CNTs. c C 1s XPS spectrum of Fe/CeO_2-CNTs. (d) XRD patterns of Fe/CeO_2-CNTs, Sulfur and S/Fe/CeO_2-CNT.

The sea cucumber-like Fe/CeO_2-CNTs were applied studied as a sulfur host material for Li-S batteries. Sulfur was loaded by the melt-diffusion method. **Figure 4.9** shows the homogeneous distribution of S, Fe and CeO_2 in Fe/CeO_2-CNT scaffold. As shown in **Figure 4.8 d**, after melting S into the as-prepared Fe/CeO_2-CNTs scaffold, the XRD pattern of the composite (blue curve) can be indexed to crystalline S (JCPDS File NO. 00-008-0247). To figure out details about storage sites of sulfur, TEM characterization was employed. As shown in **Figure 4.10**, there are much sulfur observed in CNT internal space. It is also confirmed that most sulfur loading sites are concentrated in middle of each CNT.

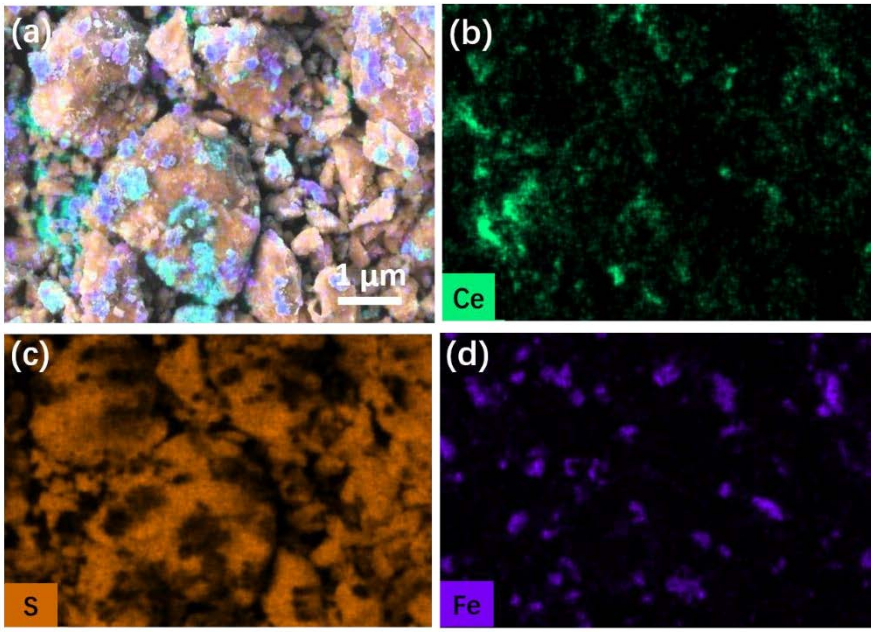

Figure 4.9 (a) EDS spectrum mapping revealing uniform distribution of (b) Ce, (c) S and (d) Fe elementals.

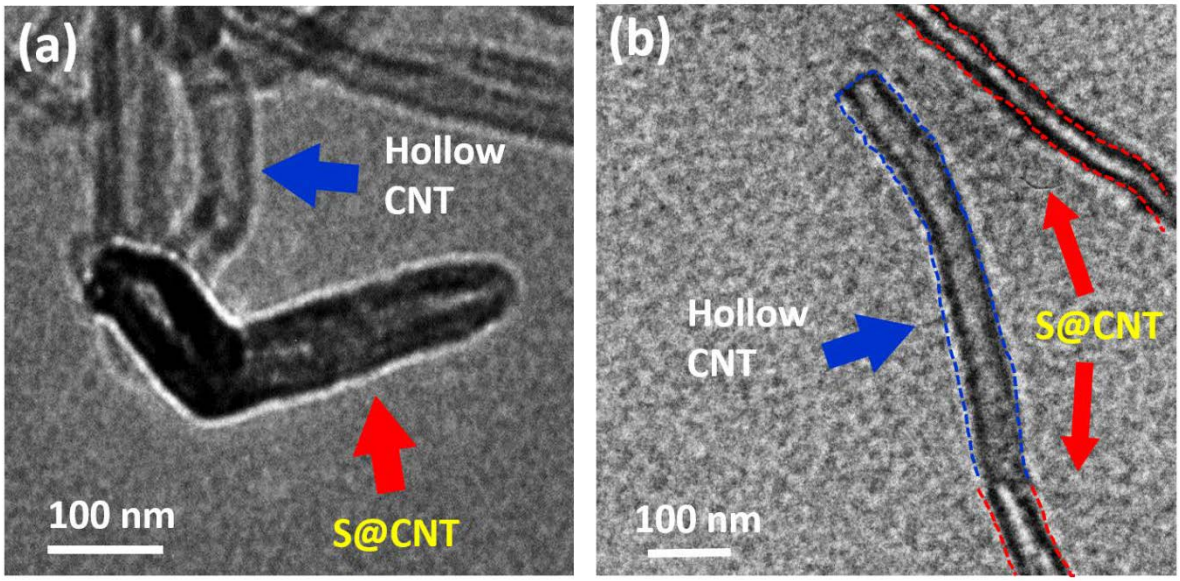

Figure 4.10 TEM images of S contained CNTs.

Li-S batteries containing 1.1 mg cm^{-2} S/Fe/CeO_2-CNTs active materials were assembled evaluated by cyclic voltammetry at a scan rate of 0.1 mV s^{-1} between 1.7 and 2.8 V. As shown in **Figure 4.11 a**, there are two sharp characteristic cathodic peaks. The peak at 2.35 V corresponds to the transformation from elementary sulfur to long-chain lithium polysulfides (Li_2S_n, $n \geq 4$) and another peak at 2.03 V corresponds to the subsequent conversion to short-chain lithium sulfides (Li_2S_n, $1<n<4$). In the anodic scan, a broader peak appeared at 2.37 V is associated with the reverse transformation of lithium polysulfides to pure sulfur. Both oxidation and reduction peaks showed a negligible shift of position from the first to the next 5 cycles, indicating good electrochemical reversibility. Furthermore, sharp curves of these redox peaks are clear evidence to confirm the high reactivity of S loaded within the Fe/CeO_2-CNT. **Figure 4.11 b** shows typical galvanostatic charge/discharge curves at 0.2 C between 1.7 - 2.8 V. There are two plateaux in the charge profiles which is consistent with the CV results. The plateaus between 2.5-2.1 V in charging profiles and 2.1-2.0 V in discharge profiles are related to the formation of long-chain lithium polysulfides and short-chain lithium polysulfides, respectively. When

the sulfur loading rate was kept at 80% (as shown in **Figure 4.12**), the S/Fe/CeO_2-CNTs (1 : 1) hybrid electrode delivered a high initial discharge specific capacity of 1241 mAh g^{-1}. At the 20^{th} and 60^{th} cycles, the electrode maintained capacities of 1115 and 1035 mAh g^{-1}, respectively. Even after 100 cycles, the electrode still had a capacity of 1003 mAh g^{-1} (81% capacity retention). Compared with previous literature, the Fe/CeO_2 CNTs 1:1 scaffold showed better electrochemical performances (CeO_2-CNTs support 1033 mAh g^{-1} at 0.2 C [40] and Fe-CNTs demonstrates 1142 mAh g^{-1} at the same rate [118]. This excellent performance can be attributed to the synergistic effect of CeO_2, Fe and N-doped CNT scaffolds.

Based on the comparison of the first discharge capacities of samples with different melamine coating amounts (**Figure 4.11 c**), it is apparent that moderate N-doping can largely improve the electrochemical performance. However, when the ratio of PBA: melamine reached 1:2, the initial discharge capacity showed a dramatic drop, which can be ascribed to the decreased specific surface area. To determine the rate performance, the electrodes were cycled from 0.2 C to 5 C and then returned to 0.2 C (**Figure 4.11 d**). It can be seen that the electrodes maintained high discharge capacities even at the higher current rate. When the current rate was reversed back to 0.2 C, a capacity of 1102 mAh g^{-1} was retained. This indicates that the S/Fe/CeO_2-CNTs electrode has a good rate capability and stability. The electrochemical impedance spectroscopy (EIS) was conducted to monitor the internal resistance of the battery after 10 cycles. As shown in **Figure 4.11 e**, it is quite obvious that Fe/CeO_2-CNTs could support a better transportation of ions and more ideal conductivity especially compared with the battery using bare CNT as sulfur holder. To study the strong chemical interaction between matrix and lithium polysulfides, a polysulfide adsorption test was performed by adding an appropriate amount of CNTs or Fe/CeO_2-CNTs powder (30 mg) into 5 mM Li_2S_6 solution. The color of Li_2S_6

Fe/CeO_2-CNTs solution faded more quickly (10 min) than pure CNTs contained Li_2S_6 solution, demonstrating the strong chemical adsorption ability of Fe/CeO_2-CNTs (**Figure 4.11 f**). In recent years, with the commercialization of Li-S batteries, higher requirements have been put forward for the improvement of sulfur loading. However, accompanied with the increase of sulfur loading, the insulaiton of pure sulfur, wettability of electrode and quick dissolution of polysulfides can also reduce the utilization efficiency of active materials during cycling [119-121]. To overcome these obstacles, the sulfur electrode of high sulfur loading is also investigated. As shown in **Figure 4.13** when the sulfur loading was improved to 4.2 mg cm^{-2}, the S/Fe/CeO_2 CNT scaffold still kept an ideal discharge capacity of 902 mAh g^{-1} at the current density of 0.2 C and maintained 412 mAh g^{-1} even after 50 cycles. In addition, the corresponding Li anodes were also observed. As shown in **Figure 4.14**, after 15 cycles, the lithium foil for the pure S@CNT cathode is considerably corroded and pulverized (**Figure 4.14 a & b**). A large number of pores are scattered on the surface of lithium electrode. In contrast, the morphology of the anode for the S@Fe/CeO_2 CNT cathode appears comparatively better for the surface of lithium foil is smoother and flatter (**Figure 4.14 c & d**). This obvious comparison confirms that sulfur can be anchored and lithium polysulfides can effectively absorbed by Fe/CeO_2 CNTs scaffold materials, hence reduce their corrosion to lithium anode surface.

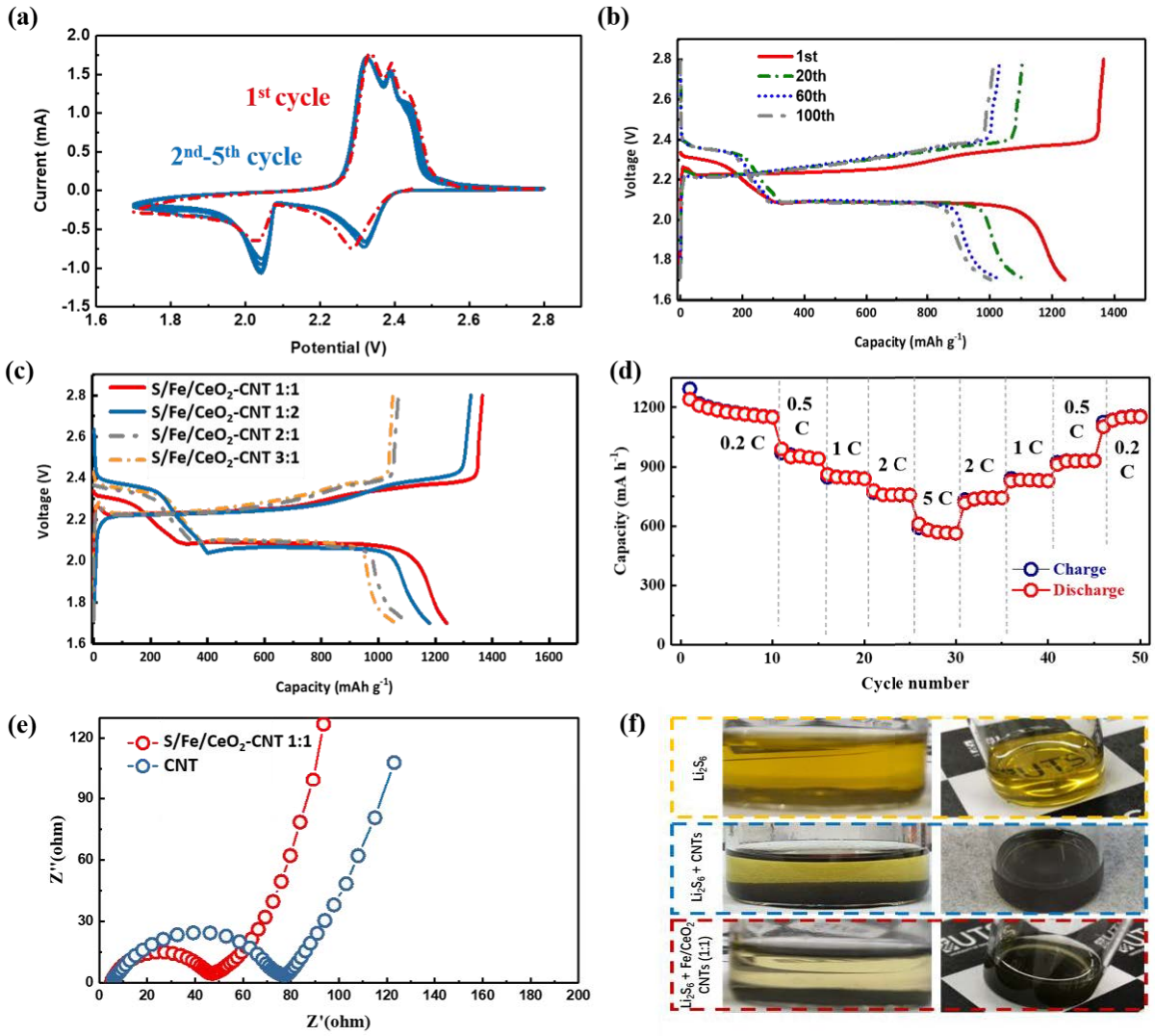

Figure 4.11 (a) The 1st-5th CV curves of S/Fe/CeO_2-CNTs electrode at a scan rate of 0.1 mV s^{-1}. (b) Typical charge and discharge profiles for the 1st, 20th, 60th, and 100th cycles at 0.2 C. (c) Typical charge and discharge profiles of S/Fe/CeO_2-CNTs with different percentages of N-dopant. (d) Rate performance of S/Fe/CeO_2-CNTs hybrids at varied current rates (0.2, 0.5, 1, 2 and 5 C). (e) EIS comparison of Li-S batteries after 10 cycles employing Fe/CeO_2 CNT and traditional CNT as sulfur holder materials. (f) The adsorption experiment of Li_2S_6, Li_2S_6 + CNTs and Li_2S_6 + Fe/CeO_2 CNTs (1 : 1) after 10 min absorption time (H_2O < 0.1 ppm, O_2 < 0.1 ppm).

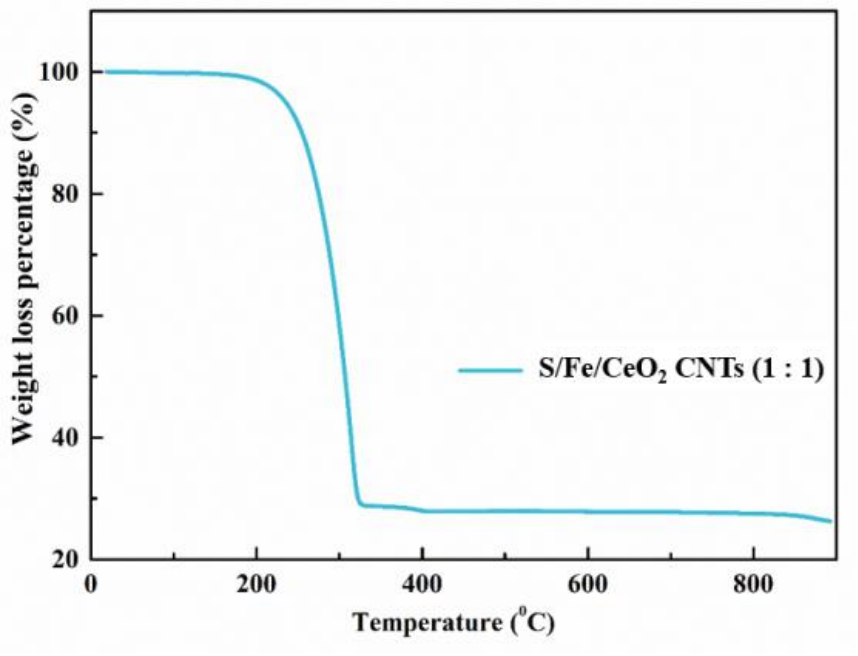

Figure 4.12. TGA curve of S/Fe/CeO_2 CNTs (1 : 1) hybrid.

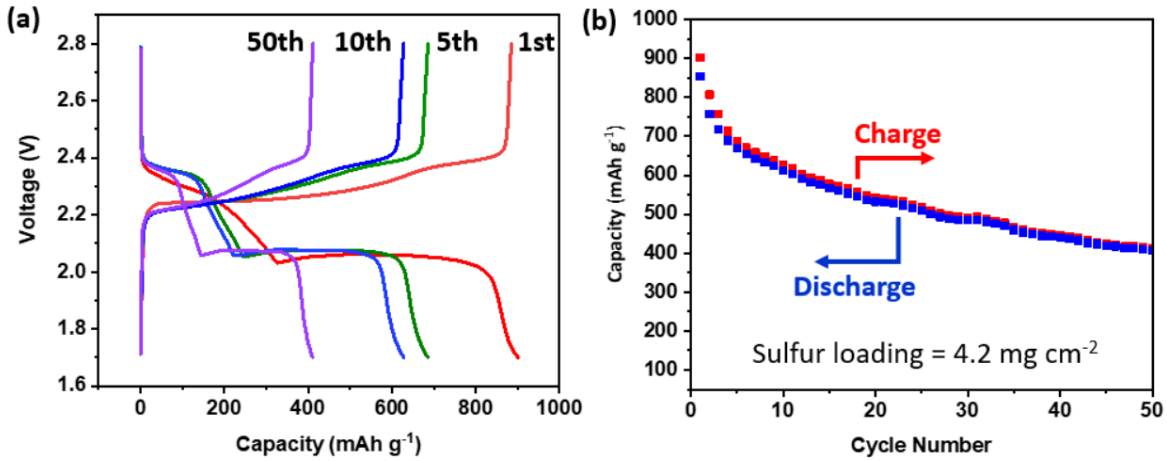

Figure 4.13. (a) Discharge/charge curve of Li-S battery with high sulfur loading at the first, 5^{th}, 10^{th} and 50^{th} cycle at 0.2 C. (b) Cycling stability of high sulfur loading Li-S battery at the current density of 0.2 C.

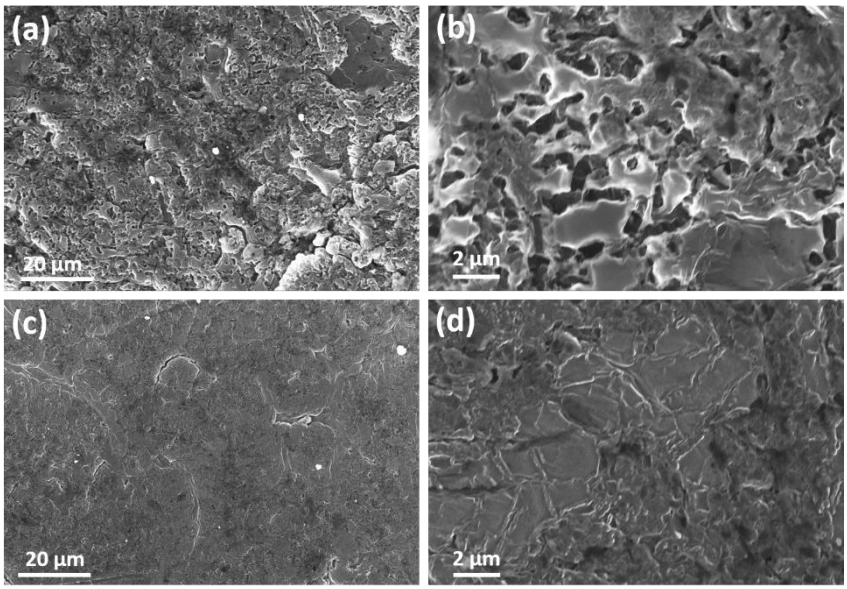

Figure 4.14. Comparison of SEM images of Li metal foils after 15 cycles at the current density of 0.2 C using high sulfur loading S/CNTs (a & b) and (c & d) S/Fe/CeO_2 CNT as cathodes.

Figure 4.15 e shows the Coulombic efficiency of the S/Fe/CeO_2-CNTs electrode at 1 C. The increase of the Coulombic efficiency during the first 10 cycles is a common phenomenon, which is due to the activationprocess of electrodes. The initial discharge capacity was 891 mAh g^{-1}, and 723 mAh g^{-1} was retained after 100 cycles. This stability has been much better than traditional CNT materials and demonstrated good consistency (**Figure 4.14**). As shown in **Figure 4.15 f**, the participation of CeO_2 could furtherly alleviate the degradation of discharge capacity illustrating the higher efficiency of CeO_2 compared with pure Fe/CNT on absorbing dissolved lithium polysulfides. To further determine the affinity between lithium polysulfide and Fe/CeO_2-CNTs, we employed *ex-situ* XPS to analyze the electrodes that have been cycled for 10 cycles and discharged to 1.7 V. It can be seen that in the XPS spectrum of element Li (**Figure 4.13 a**), an obvious single asymmetric peak is located at around 55.8 eV, which can be fitted as two peaks at 55.6 eV and 56.8 eV. The first peak at 55.8 eV corresponds to the Li-S bond derived from polysulfides. While the second one at 56.8 eV can

be assigned as the combination of Lithium polysulfide and dopant nitrogen [122]. **Figure 4.15 b** shows the shift of Fe 2p3/2 from 711.65 eV to 710.46 eV after discharging. Such an apparent shift (~ 1.21 eV) can be ascribed to the conversion of Fe to Fe (III)-S, in which 710.46 eV is a characteristic peak on the surface of initial mackinawite. Furthermore, the peak of Fe 2p1/2 was also observed with a replacement of 3.56 eV [123]. Meanwhile, **Figure 4.13 c** shows the XPS of S 2p, in which the peak at 160.4 eV corresponds to the Li_2S. The peak at 161.8, 162.1 and 163.1 eV can be ascribed to Li_2S_2, [S-SO_3]$^{2-}$ and polysulfides respectively [124]. A noticeable peak at 169.3 eV coincides in binding energy with sulfate ([SO_4]$^{2-}$, S(+VI)) due to the reaction with surface oxygen-functional-groups on Fe/CeO_2-CNTs. The remaining peak at 164 eV is attributed to the S(0) oxidation state [125]. As shown in **Figure 4.13 d**, a significant peak shift corresponding to Ce 3d5/2 was observed. After 10 cycles, the peak of Ce 3d5/2 shifted from 882.6 eV to 876.8 eV. This distinct shift (~ 5.8 eV) demonstrates the strong binding between CeO_2 and dissolved polysulphides, which is consistent with the previous report [126]. Meanwhile, it is noticed that, compared with the initial XPS results, the peaks corresponding to Ce 3d3/2 became negligible after the cycling, which could be due to the low quantity of Ce and the interference of electrolyte and/or solute coating environment (such dissolved LiTFSI in electrolyte etc.). The same change was also observed on nitrogen which is shown in **Figure 4.15**. The strong adsorption between Fe/CeO_2 particles and dissolved polysulfide confirmed effectively immobilizing ability of 3D Fe/CeO_2 CNTs scaffold composite. More importantly, because most of the Fe/CeO_2 particles are concentrated on tips of CNTs, this has greatly boost the chances of contact with lithium polysulfide. In fact, the mechanism of absorption is quite similar to predation process of sea anemones and other marine organisms preying on plankton in seawater.

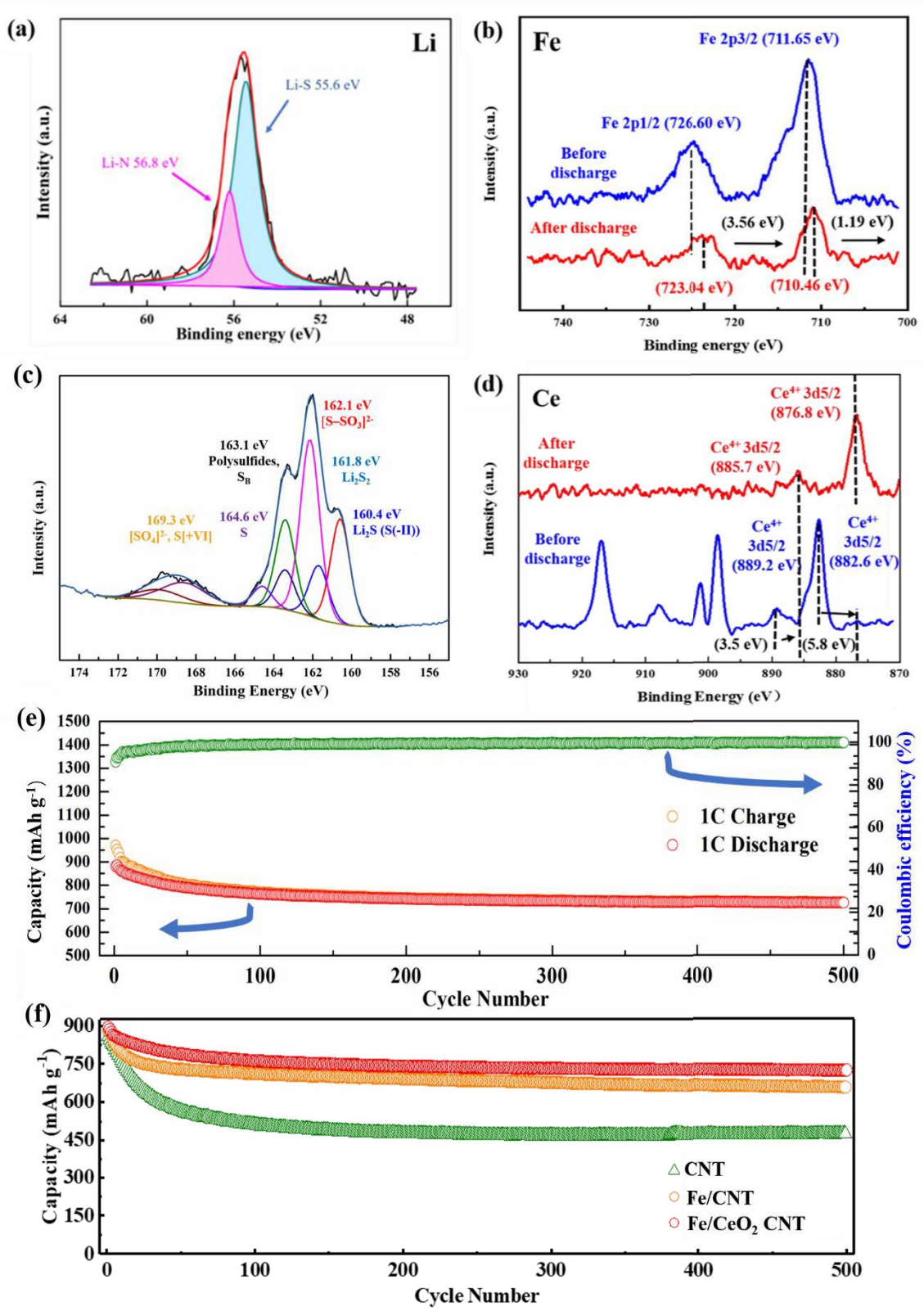

Figure 4.15 The *ex-situ* XPS of (a) Li, (b) Fe, (c) S and (d) Ce of electrodes discharged down to 1.7 V. e Cycling performances of S/Fe/CeO_2-CNTs electrode at 1 C rate. (f) Comparison of stability of

batteries using CNT, Fe/CNT and Fe/CeO_2-CNT as cathode sulfur holder and cycled for 500 cycles at the current density fo 1 C.

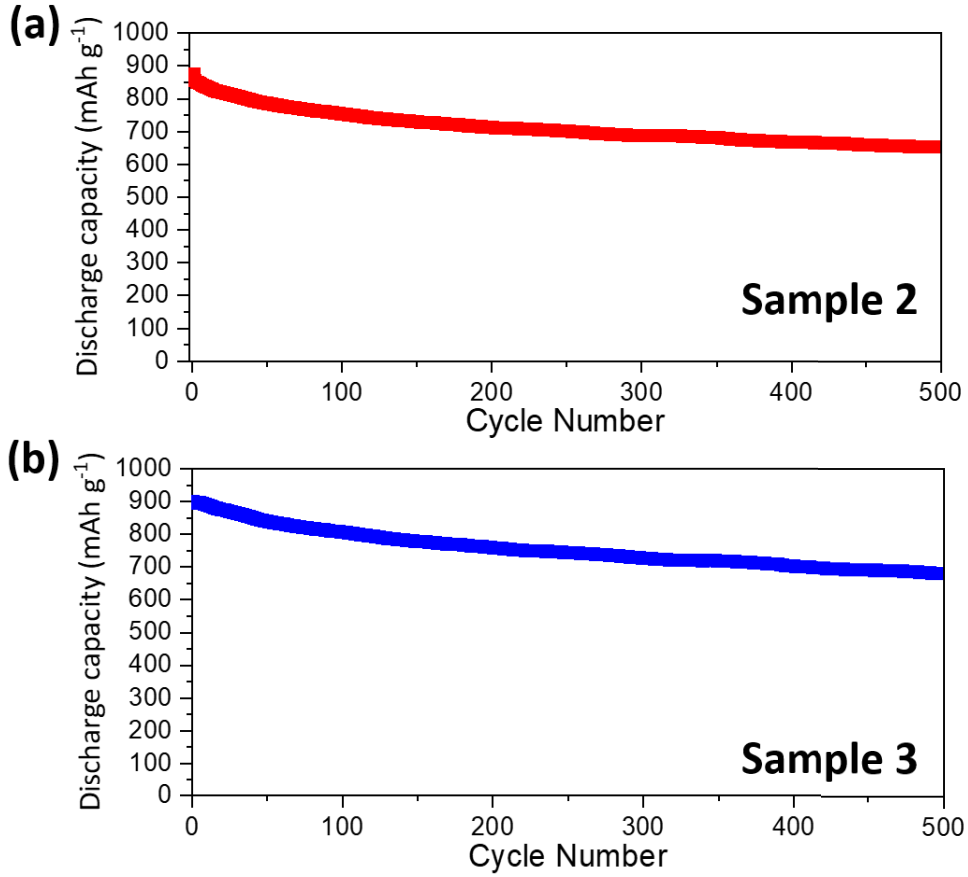

Figure 4.16. The consistency of cycling performances of S/Fe/CeO_2 CNTs (1 : 1) cathodes when cycled at the current density of 1 C.

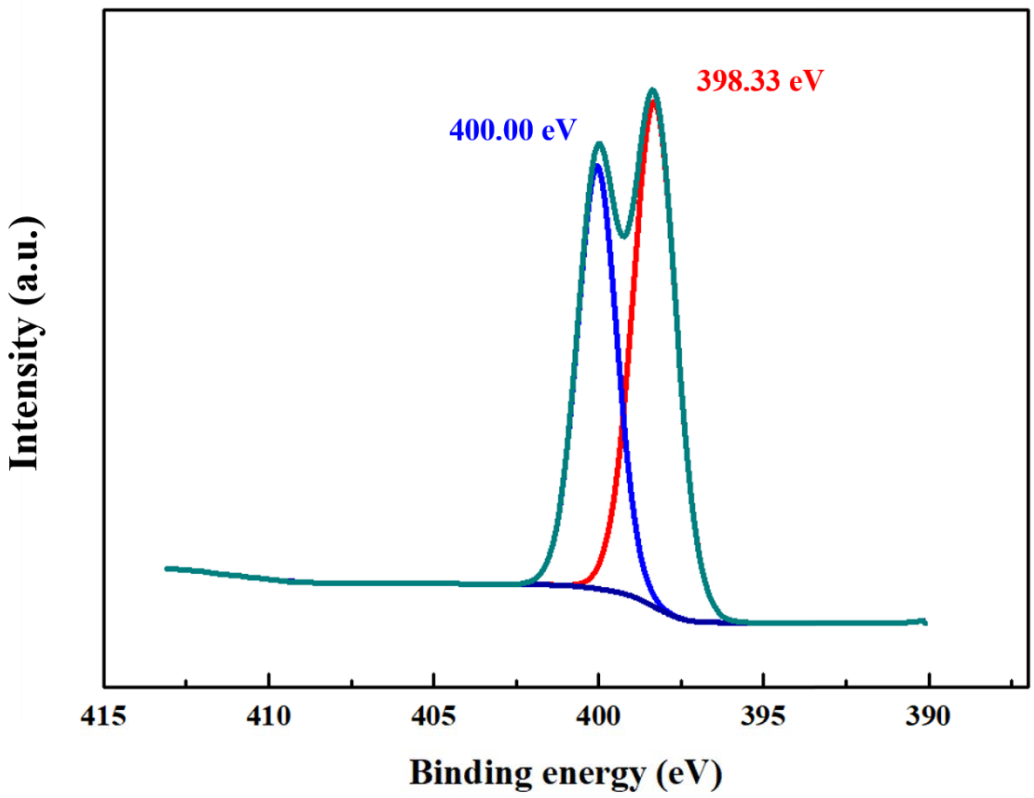

Figure 4.17. *Ex-situ* XPS results of nitrogen of electrode materials after the 100th cycle.

Chapter 5 Immunizing lithium metal anodes against dendrite growth using protein molecules to achieve high energy batteries

5.1 Introduction

Lithium (Li) metal anodes offer the highest theoretical capacity (3,860 mAh g^{-1}) and lowest electrochemical potential (-3.04 V *vs.* standard hydrogen electrode) among all anode materials for lithium batteries [127]. When coupled with high capacity cathode materials such as lithium transition metal oxide (LMO), a Li–LMO battery can achieve specific energy densities of 450 – 500 Wh Kg^{-1}, which is double or even triple the capacity of conventional Li–ion batteries [128]. Li metal anodes are indispensable in lithium–sulfur and lithium–oxygen batteries, which can further promote the practical specific energy densities to ~ 650 Wh Kg^{-1} and ~ 950 Wh Kg^{-1}, respectively [128]. Differing from graphite anodes in Li–ion batteries, Li metal anodes rely on Li stripping and plating, inevitably leading to nucleation and growth of Li dendrites. The growth of Li dendrites causes many severe problems, including low coulombic efficiency, short cycle life, short-circuiting, and safety hazards [129].

Recent studies demonstrate that Li deposition in liquid electrolytes involves two different mechanisms [130]. At low current densities and capacities (e.g., under the Sand's capacity), mossy Li grows from the roots. While, above Sand's capacity, wispy Li dendrites quickly grow at the tips. The growth of wispy Li dendrites is a self-amplification process. The 'tip effect' attracts more Li-ions due to the enhanced electric field at the tips of Li dendrites[131]. The hemispherical shape of the tips enables three-dimensional (3D) Li-ion diffusion, rather than the one-dimensional diffusion on a flat surface of Li anode, leading to faster Li plating onto the tips[131]. Therefore, it is essential to inactivate the mossy Li in the initial stage to prevent them from growing into wispy Li dendrites. Many approaches have been

developed in attempts to suppress dendrite growth, such as employing biomacromolecule interlayer [132], developing 3D porous current collectors [127, 133-134], introducing artificial solid electrolyte interphase (SEI) [135], and optimizing electrolyte formula [136]. Among those strategies, introducing additives in the electrolyte, such as solvents or salts, has been proved to be effective in suppressing Li dendrite formation. So far, there are two types of electrolyte additives reported for Li metal anodes. The first type of additive participates in the formation of SEI, which could significantly enhance the physical property and chemical stability of SEI. The second type of additive absorbs on the tips of the Li protrusions and forms a positively charged electrostatic shield around the tip of the protuberances, which forces further deposition of lithium to adjacent area and suppresses dendrite formation. Despite more than 50 years of research, it remains a significant challenge to achieve 100% dendrite-free Li metal anodes. The ideal solution to completely prevent the formation of wispy Li dendrite would be to automatically inactivate mossy Li as soon as they begin to form, mimicking “early warning” defense responses in biological immunization mechanisms. Nature’s biological systems already show evidence of sophisticated multi-step immunization mechanisms. For example, when faced by invading pathogens, antibodies are quickly produced, migrate to the precise locations, and quickly neutralize, inactivate, or destroy the pathogens [137].

In this work, we discover that protein molecules (e.g., fibroin molecules) can effectively prevent lithium metal anodes from severe dendrite growth in lithium metal batteries, resembling natural immunization. We believe this self-defense mechanism enabled by natural protein molecules will undoubtedly bring inspiration for achieving safe and high-energy-density lithium metal batteries.

5.2 Experiment section

5.2.1 Materials.

The blank ether-based electrolyte is 1 M lithium bis(trifluoromethane sulfonyl)imide (LiTFSI) in a mixed solvent of 1,3-dioxolane (DOL) and 1,2-dimethoxyethane (DME) (1:1 v/v) with 1 wt% lithium nitrate ($LiNO_3$) as additive. The lyophilized silk fibroin flakes with the molecular weight ≥ 1000,000 Daltons were purchased from Simeite company (SF003). To prepare electrolyte with different concentration of fibroin, a certain amount of fibroin is immersed into 10 ml electrolyte. After ultrasonic for 30 minutes, the electrolyte is kept standstill for 48 h to enable fibroin to fully disperse in the electrolyte. For the preparation of electrospun fibroin interlayer, the fibroin solution is prepared by dissolving the commercial fibroin sponges in deionized water under stirring for 1 h. The concentration of fibroin solution for electrospinning is controlled to be 12 wt%. The electrospun fibroin interlayer is collected on a target rotating drum, which is placed opposite to the syringe tip with a distance of 15 cm. A voltage of 25 kV is applied to the collecting target by a high voltage power supply (Chungpa EMT Co., Korea).

5.2.2 Characterization.

Circular dichroism (CD) spectra are collected using a Jasco H-810 spectropolarimeter equipped with a NESLAB RTE-111 slab and purged with N_2 gas at a flow rate of 3 to 5 ml min^{-1}. The fibroin aqueous solution was spotted in 0.10 cm path length cells for detection. CD spectra were recorded from 190 to 250 nm wavelength with a resolution of 0.2 nm and an accumulation of five scans at a scanning rate of 100 nm min^{-1} and the response time of 0.25 s. A blank solution was measured under the same experimental conditions and the blank levels were subtracted from the data. The ratio of α-

helix and β-sheet structure was analyzed by the protein secondary structure estimation software (Protein secondary structure estimation). The Fourier-transform infrared spectroscopy (FT-IR) was used as an effective method to measure fibroin. The adsorption features were recorded using a Nicolet 6700 FT-IR spectrometer in the range of 1800-1200 cm^{-1} and the resolution of 4 cm^{-1}. The fibroin interlayer was retrieved from the Li | Li symmetric cell. After cycling for 50 cycles at a current density of 5 mA cm^{-2}, the fibroin interlayer was removed from coin cell in the Ar-filled glove box and washed by 1 ml DOL to remove the salt. Before FT-IR characterization, the fibroin interlayer was dried under vacuum for 12 hours. To process the protein fluorescence luminescence measurement, the fibroin was firstly dyed by 8-Anilino-1-naphthaleneslfonic acid and dispersed in the electrolyte. After immersed in the electrolyte for 2 h, the Li metal electrode was taken out and washed by DOL solvent for 3 times. To prevent being oxidized in air, the Li foil was sealed in a quartz dish in Ar. The two-photon excitation microscopy (Cari Zeiss, LSM 88-NLO) was employed to monitor the fluorescence phenomenon on Li metal electrode under UV-light. Distribution of fluorescence intensity was analyzed by ZEN 3.2 software. X-ray photoelectron spectroscopy (XPS) measurements were carried out using a ThermoFisher Scientific ESCALAB250Xi with a monochromatic Al Ka X-ray source (3000 eV) at 150 W and 15 kV with a beam spot size of 500 μm. The samples were transferred into the vacuum chamber using a sealed Ar-filled vessel. Depth profiling was conducted using Ar ion sputtering with an accelerating voltage of 0.5 kV over a 2.5×2.5 mm area to 0.5 μm depth. The thickness of the SEI was estimated from the calibrated sputtering rate of 0.3 nm per second in Ta_2O_5 and the sputtering time at which the atomic concentration of Li drops to < 5% (by measurement or extrapolation). The Cu $2p_{3/2}$ peaks arise due to the underlying of Cu foil. Field-emission scanning electron microscopy (FE-SEM, Zeiss Supra 55VP) was used to investigate the morphologies of the as-prepared fibroin interlayer and

the cycled electrodes.

5.2.3 Electrochemical measurements.

For the Li | Li symmetric cell assembling, coin cells (CR2032) are assembled in an Ar-filled glove box (MBraun, H_2O < 0.1 p.p.m, O_2 < 0.1 p.p.m), using two pieces of Li metal disks, two pieces of fibroin interlayers, ether-based electrolyte, and Celgard^{TM} 2325 separator. The ether-based electrolyte is 1 M LiTFSI in DOL/DME (1:1 v/v) containing 1 wt% $LiNO_3$ with or without fibroin. For Li | Cu half-cell assembling, coin cells were assembled using Li foil as the counter electrode and Cu foil as the working electrode. For the Coulombic efficiency testing, in each galvanostatic cycle, Li was deposited on Cu foil at the desired current density and capacity, and stripped away by charging to a cut-off voltage of 1.0 V *vs.* Li^+/Li. The Li plating/stripping study was conducted on Neware battery testers at room temperature. Electrochemical impedances were measured using a CHI660E electrochemical station with a frequency range of 0.1 Hz to 100 kHz. For Li || $Li_4Ti_5O_{12}$ (LTO) full cell test, LTO electrodes are prepared first. The weight ratio of LTO (BTR Co.) material, carbon black (CB) and sodium carbonxymethly cellulose (CMC) in the LTO electrode is 8:1:1. The Li || LTO full cells were assembled using Li metal electrode, fibroin interlayer, 30 μL electrolytes, Celgard^{TM} 2325 separator, and LTO cathode electrode. All cells were assembled in an Ar-filled glove box (H_2O < 0.1 ppm, O_2 < 0.1 ppm). Li || LTO full cells were first activated at 0.2 C for 5 cycles within a voltage window between 1.0 V and 2.5 V. Then, they were cycled at 2 C for long-term cycling stability test.

5.3.4 Cryogenic TEM (Cryo-EM) characterizations.

Cryo-EM characterizations were carried out using an FRI Titan 80-300 environmental scanning

transmission electron microscope with an accelerating voltage of 300 kV. The instrument was equipped with an aberration corrector in the objective lens, which was tuned before each sample analysis. To prepare the cryo-EM sample, coin cells were assembled with the working electrode attached with 300 mesh Cu transmission electron microscopy (TEM) grids. After Li metal was deposited onto the TEM grid, coin cells were immediately disassembled in an Ar-filled glovebox. The TEM grids were washed with DOL to remove Li salts. After drying, the TEM grid with plated Li was placed in an Eppendorf tube and transferred out of the glovebox. A slight positive pressure inside the Ar-filled glovebox (and thus the Eppendorf tube) prevented air from leaking into the tube. The sealed Eppendorf tube was plunged quickly into a bath of liquid nitrogen (LN_2). Then the frozen Eppendorf tube was quickly crushed with a bolt cutter while still immersed in LN_2 to expose the Li metal to the cryogen. The TEM grid was carefully mounted onto a TEM cryo-holder (Gatan 626) using a cryo-transfer station under LN_2 immersion. During transferring TEM cryo-holder into the TEM column (~1 second), a built-in shutter on the holder was closed to prevent Li contacting with air. A LN_2 dewar bottle was attached to the holder to maintain the sample at cryogenic temperature. In this way, the Li metal can be safely transferred from the coin cell to the TEM chamber. Once inside the TEM chamber, the sample was kept at -178 ℃.

5.2.5 COMSOL™ simulation.

The stationary equation of continuity is used to handle the stationary electric currents in conductive media. In a stationary coordinate system, the point form of *Ohm's law* states [138]:

$$J = \sigma E + J_e \qquad \text{Equation (5-1)}$$

Where σ is the electrical conductivity (S m^{-1}), and J_e is an externally generated current density (A m^{-}

^{2}). The static form of the equation of continuity then states [138]:

$$\nabla \cdot \mathrm{J} = -\nabla \cdot (\sigma \nabla \mathrm{V} - \mathrm{J_e}) = 0 \qquad \text{Equation (5-2)}$$

To handle the current sources, we generalize the equation to [138]:

$$-\nabla \cdot (\sigma \nabla \mathrm{V} - \mathrm{J_e}) = \mathrm{Q_j} \qquad \text{Equation (5-3)}$$

In planar two-dimension stimulation, the Electric Currents interface assumes that the model has a symmetry, where the electric potential varies only in the *x* and *y* directions and is constant in the *z* direction. This implies that the electric field, E, is tangential to the *xy*-plane. The Electric Currents interface then follows the following equation, where *d* is the thickness in the *z* direction [138]:

$$-\nabla \cdot d(\sigma \nabla \mathrm{V} - \mathrm{J_e}) = d\mathrm{Q_j} \qquad \text{Equation (5-4)}$$

5.3 Results and discussion

5.3.1 Self-defense mechanism of fibroin.

Fibroin is selected as a model protein molecule owing to its simple secondary structure for easy characterization [139-141]. It is well recognized that biomolecules such as proteins can be intrinsically adsorbed on the surface of inorganic or metallic materials, and this adsorption process can be further enhanced on the tips or sharp edges of the substrates through electrostatic interactions and cooperative binding effect [142]. The pristine fibroin molecule has a simple helix structure with periodic repeats of three types of amino acids, e.g. Alanine residue (ALA), Glycine residue (Gly), and Serine residue (Ser) [as shown in **Figure 5.1 a** (Upper-left panel)] [143], in which the hydrophobic functional groups such as simple methyl groups (–CH_3) are wrapped inside the helix structure and the hydrophilic peptide bonds (-OC-NH-) are exposed externally [144, 145]. A visible Tyndall effect confirms that fibroin can be

dispersed in the ether-based electrolyte (1M LiTFSI in DOL/DME) in the form of micelles (**Figure 5.2**). Furthermore, the fibroin molecules can still be evenly dispersed during the stripping/plating process (**Figure 5.3**). When fibroin molecules interact with lithium metal nuclei, we hypothesize that they undergo a conformational change at the secondary structure level from an α-helix to a β-sheet because the β-sheet structure was found to be more thermodynamically stable than an α-helix [146, 147]. After the structural and spatial conformational change, the β-sheet fibroin molecules could be easily adsorbed on the tips of mossy Li, reducing the electric field intensity on the tips and preventing the growth of the mossy Li into the wispy Li dendrite. In contrast, lithium dendrites continuously grew when fibroin was not present on the Li metal anode (**Figure 5.1 a**).

In order to confirm the above hypothesis, circular dichroic (CD) spectroscopy was employed to analyze the secondary structure transition of protein molecules after cycling. An interlayer of fibroin was prepared by electrospinning and placed on the top of the Li foil in a coin cell. The ether-based electrolyte used in this work is 1 M lithium bis(trifluoromethane sulfonyl)imide (LiTFSI) in a mixed solvent of 1,3-dioxolane (DOL) and 1,2-dimethoxyethane (DME) (1:1 v/v) with 1 wt% lithium nitrate ($LiNO_3$) and 0.5 wt% fibroin as additives. After electrochemical cycling of the coin cell, the interlayer was retrieved from the disassembled coin cell and washed with deionized water. Then, the fibroin solution retrieved from cycled interlayer was analyzed by CD spectroscopy. For comparison, the water solution with pristine fibroin was also prepared for analysis. As shown in **Figure 5.1b**, the CD spectrum of pristine fibroin shows a negative Cotton effect around 198.0 and 202.3 nm, confirming the predominance of the α-helix structure of fibroin molecules [148]. By contrast, we found that the negative Cotton effect moved to 205.8 nm (red curve) in the CD spectrum of cycled fibroin. This unambiguously proves the transformation of protein molecules from α-helices (the result of

intramolecular hydrogen bonds) to β-sheets (the result of intermolecular hydrogen bonds) [149]. Such secondary structural transformation of fibroin molecules was further confirmed by Fourier transform infrared spectroscopy (FT-IR). As shown in **Figure 5.1c**. The broad peak at around 1650 cm^{-1} of the pristine fibroin associated with the amide I band from C=O stretching (~80%) with minor contribution from N-H in-plane blending significantly shifts to 1637 cm^{-1} after cycling. While the original peak at around 1532 cm^{-1} corresponding to amide II from C-N stretching and N-H in-plane blending moves to 1513 cm^{-1}. The shift of the signature FT-IR peaks clearly indicates that the secondary structure of fibroin molecules transformed from the original α-helix to β-sheets after cycling [150, 151]. To exclude the possibility of secondary structure transformation triggered by Li ions or organic solvents, a flake of fibroin was immersed in the electrolyte for 1 month and retrieved for characterization. As shown in **Figure 5.4**, after being immersed in the electrolyte, two peaks in Amide I area in FT-IR curve of fibroin do not change compared with pristine fibroin. Therefore, it clearly confirmed that the transformation of the protein secondary structure is not triggered by electrolyte and Li^+.

According to the previous report [142], the spatial conformation and high affinity of peptide bonds in fibroin molecules can drive fibroin secondary structure change. When protein molecules with the α-helix secondary structure interact with a Li metal surface, the –NH and C=O functional groups of the peptide bonds show a strong affinity with the Li metal anode, triggering the irreversible conformation change from α-helix (high energy) to β-sheet (low energy). Once the initial layers of fibroin molecules conformably bind to the Li metal surface, the adsorption of further protein molecules can be significantly enhanced owing to cooperative binding effects [152]. In addition, nanoscale surface roughness such as local protrusions (e. g. Li buds) can also promote the adhesion of protein molecules

[153, 154]. According to a previous study, fibroin is an insulating material with a high electrical resistivity of 8.5 Ω m [155]. Therefore, the adsorption of fibroin molecules on Li buds can reduce the local electric field intensity and promote the deposition of Li in the surrounding area. We conducted COMSOL™ simulations on the absorption of protein molecules on Li buds, which elucidates the changes in electric field intensity distributions on Li embryos upon the adsorption of protein molecules. As shown in **Figure 5.5 a** the tip of a Li bud exhibits the highest electric field intensity, promoting further non-uniform plating and vertical dendritic growth of Li if there is no influence of protein molecules at the close range. When protein molecules are immobilized at the tip of the Li bud, the electric field intensity at the tip rapidly drops from 20 V m^{-1} to 10 V m^{-1}, while the highest intensity points transfer to the outer border area covered with protein molecules (**Figure 5.5 b**). When the entire Li bud is fully covered by protein molecules, the growth of Li dendrite from the Li bud will completely stop, leading to Li deposition on the adjacent regions around Li bud until a smooth deposition layer is formed (**Figure 5.5 c**). A similar strategy has been reported by Zhang *et al.* to suppress the formation of Na dendrites by changing the electric field distribution through selective Li-ion covering on the tip of Na dendrites [156].

In order to directly observe the adsorption behavior of protein molecules on the edges and defects of Li metal anodes, we employed the protein fluorescence luminescence method. Fibroin molecules were dyed with fluorescent dye and then dispersed in the ether-based electrolyte. After being immersed in the electrolyte, Li metal electrode was retrieved and washed by DOL to remove Li salts and excess fibroin. To deliberately create defects on the surface of lithium metal foil, we used the tip of a needle to create a pin hole as a controlled defect. As shown in **Figure 5.1 d-f**, the adsorbed fibroin molecules emitted clear fluorescence under ultraviolet (UV) light observed by the fluorescence microscope.

Especially, fluorescence intensity is much stronger at the edge and sharp tips on Li metal anode, particularly in the region with large curvature. This result corroborates that fibroin molecules prefer to be adsorbed on sharp edges such as dendrites or other defects rather than the flat region, which is consistent with the COMSOL simulation.

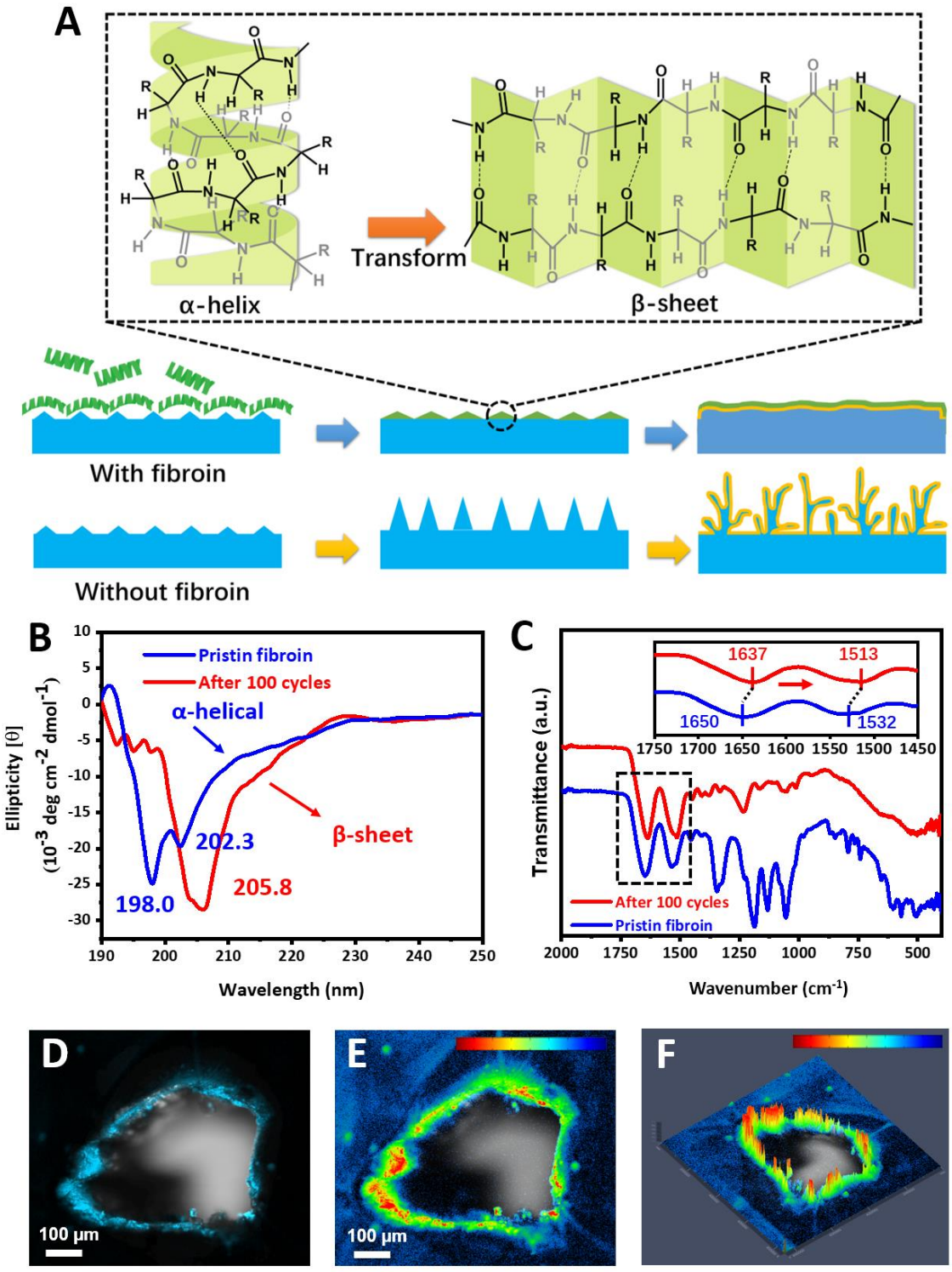

Figure 5.1 Schematic diagram of the self-defense mechanism of fibroin. a Illustration of the secondary structural transformation of fibroin molecules and the self-defense mechanism of immunizing Li metal anode against Li dendrite growth. ("R" groups are known as side chains of amino

acids (-H to Glycine residue, -CH_2OH to Serine residue, and -CH_3 to Alanine residue)). CD spectra (**b**) and ATR-FT-IR spectra (**c**) of pristine fibroin and recovered fibroin from the cycled cell after 100 cycles. (**d)** A fluorescent image of fibroin molecule distribution around the edges and protrusions on a Li metal foil under UV-light. The corresponding 2D (**e**) and 2.5 D (**f**) simulations of fluorescence intensity. The scale bars on the top in (**e**) and (**f**) correspond to the intensity increase from blue to red. Scale bars, (**d**, **e**) 100 μm.

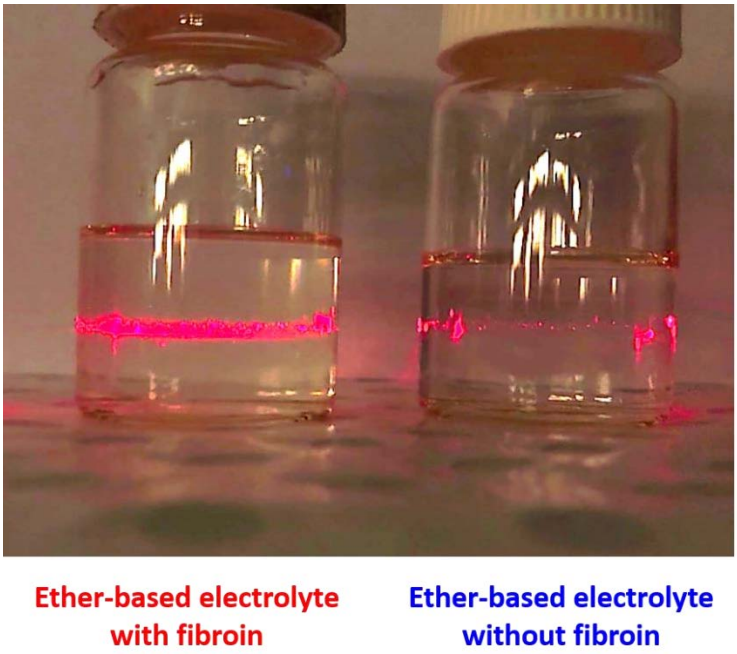

Figure 5.2 Digital photo of Tyndall effect in ether-based electrolytes with and without fibroin.

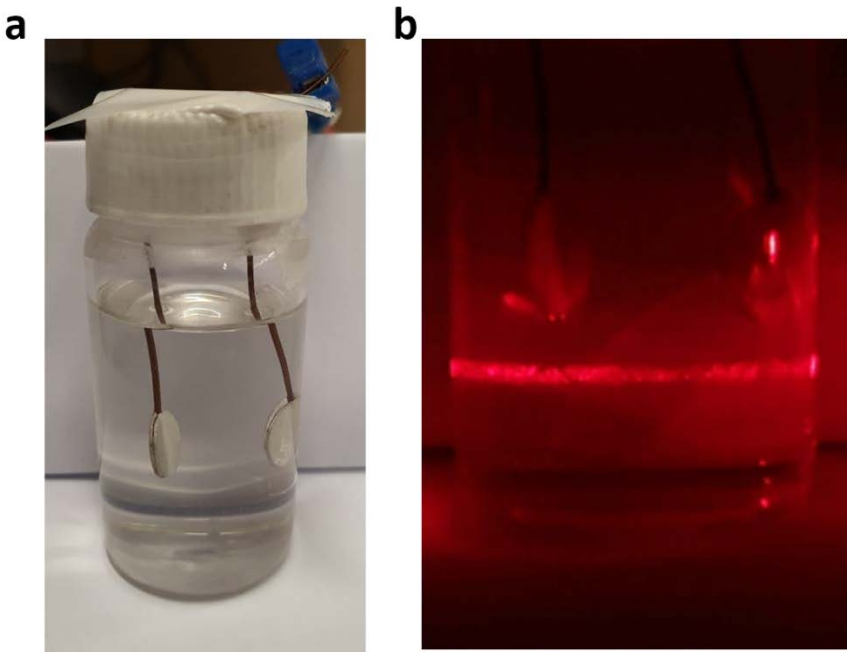

Figure 5.3 Tyndall effect of fibroin dispersed electrolyte during Li | Li plating/stripping process. Tyndall effect can be observed in a transparent Li | Li symmetric cell during plating/stripping process at a current density of 1 mA cm^{-2}, which confirms that fibroin molecules are dispersed homogeneously in the electrolyte during cycling.

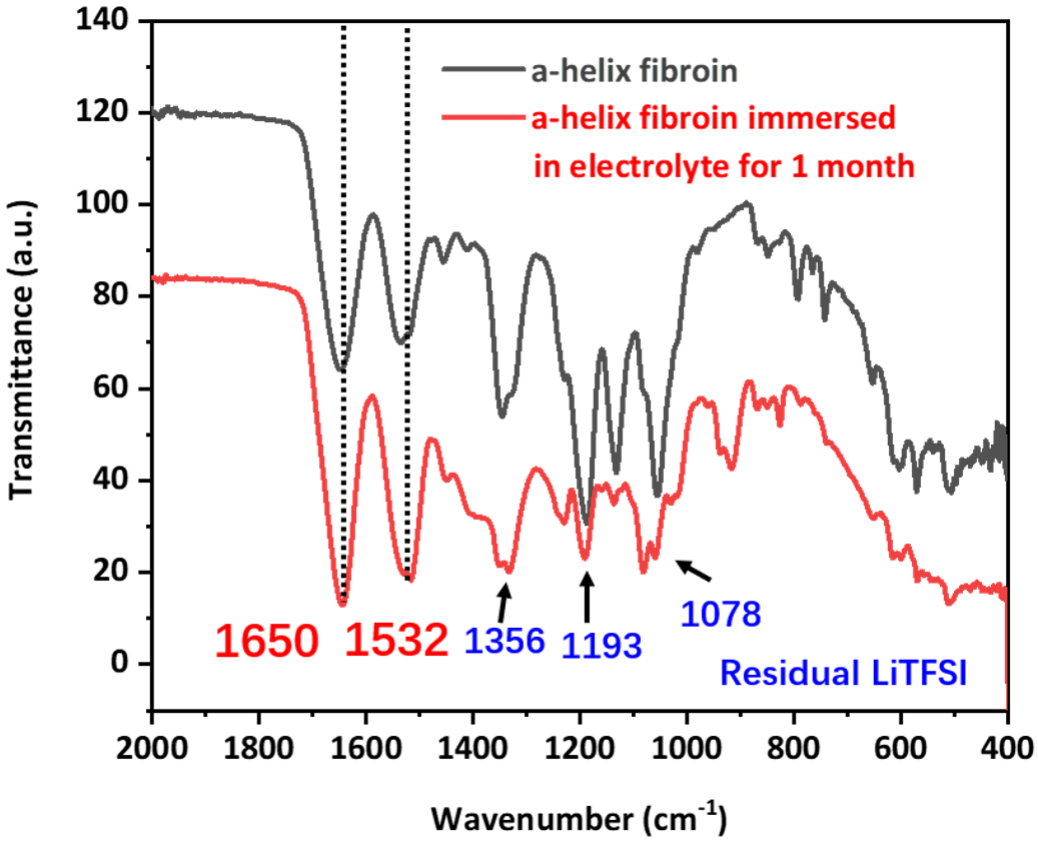

Figure 5.4 Comparison of FT-IR curves of fibroin before and after immersed in the ether-based electrolyte for 1 month.

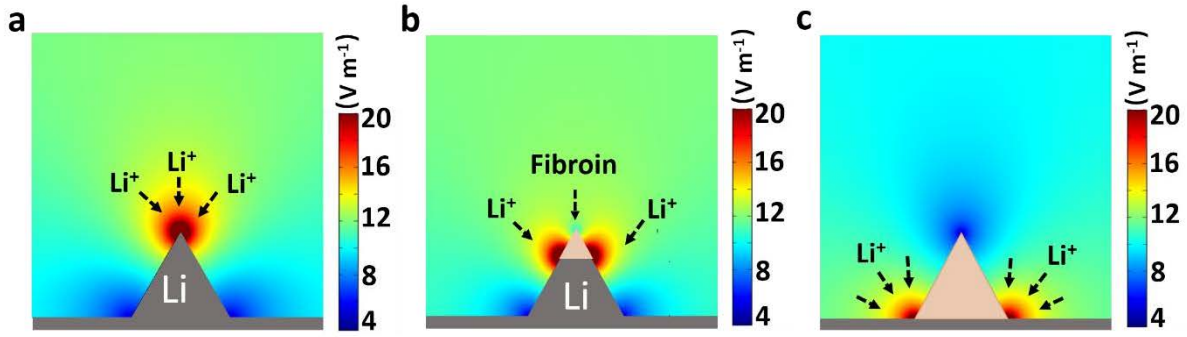

Figure 5.5 COMSOL™ simulation of the change of electric field distribution around Li buds. a before and **b**, **c** after covered by fibroin molecules with the height ratio of (b) 30% and (c) 100%.

5.3.2 Dense Li deposition with fibroin.

We employed scanning electron microscope (SEM) observation to investigate Li deposition after cycling with and without fibroin additives in the ether-based electrolyte at a current density of 1 mA cm^{-2} with a specific areal capacity limitation of 1 mAh cm^{-2}. As shown in **Figure 5.6 a, b**, for the cells without fibroin additives in the electrolyte, the top and cross-section views of a Li metal anode with blank electrolyte (i.e. electrolyte with no added fibroin) after 15 cycles exhibited the typical dendritic morphology [157]. The wispy Li dendrites induce a rapid consumption of the electrolyte and short cycle life of the cells. In a sharp contrast, the Li deposition shows a dense and nodule-like morphology when fibroin is added to the electrolyte (**Figure 5.6 c, d**) [158]. As shown in **Figure 5.7**, even though after 100 cycles, the surface of Li metal anode in the electrolyte with fibroin still maintained a compact surface (**Figure 5.7 a, b**). While the Li metal anode cycled in the blank electrolyte was covered by coral-like Li dendrites (**Figure 5.7 c, d)**. We further characterized the SEI formed in the electrolyte with fibroin using cryogenic electron microscopy (cryo-EM) (**Figure 5.6 e, f**). Li metal was electrochemically deposited on copper grids in a coin cell [159]. **Figure 5.6 e** shows a typical cryo-EM image of Li nuclei

deposited in the electrolyte with fibroin additive. The edge of the Li nuclei with darker contrast corresponds to the SEI region (due to the higher atomic numbers of the SEI components than elemental Li) [157, 160]. In a high-magnification cryo-EM image (**Figure 5.6 f)**, the surface of Li metal shows a bi-layer structure. The outer layer is the absorbed fibroin molecules and the inner layer has been identified as polymeric SEI. According to our previous investigation, the SEI layer formed in blank ether-based electrolyte has a thickness about 17 nm. After we added fibroin molecules in the electrolyte, the thickness of modified SEI has increased from 17 nm to 28 nm [161, 162]. Therefore, this clearly confirmed that the fibroin additive in the electrolyte is involved in the SEI formation.

To in situ monitor the Li deposition behavior, Li | Li symmetric cells are assembled in home-made glass capillaries, as illustrated in **Figure 5.8**. In the initial stage, the mossy Li starts to deposit on the Li metal surface in the blank electrolyte. With the increase of the deposition time, the surface of Li metal is fully covered by mossy Li within 20 min. After then, wispy Li dendrites quickly grow on top of the mossy Li deposition layer. In contrast, we did not observe the formation of a large amount of mossy Li on the Li metal anodes in the electrolyte with fibroin under the same deposition condition. The Li deposition layer is compact and homogenous without the formation of the detrimental wispy Li dendrites. Therefore, the addition of fibroin molecules in the electrolyte effectively deactivates mossy Li at the initial stage, preventing them from growing into wispy Li dendrites.

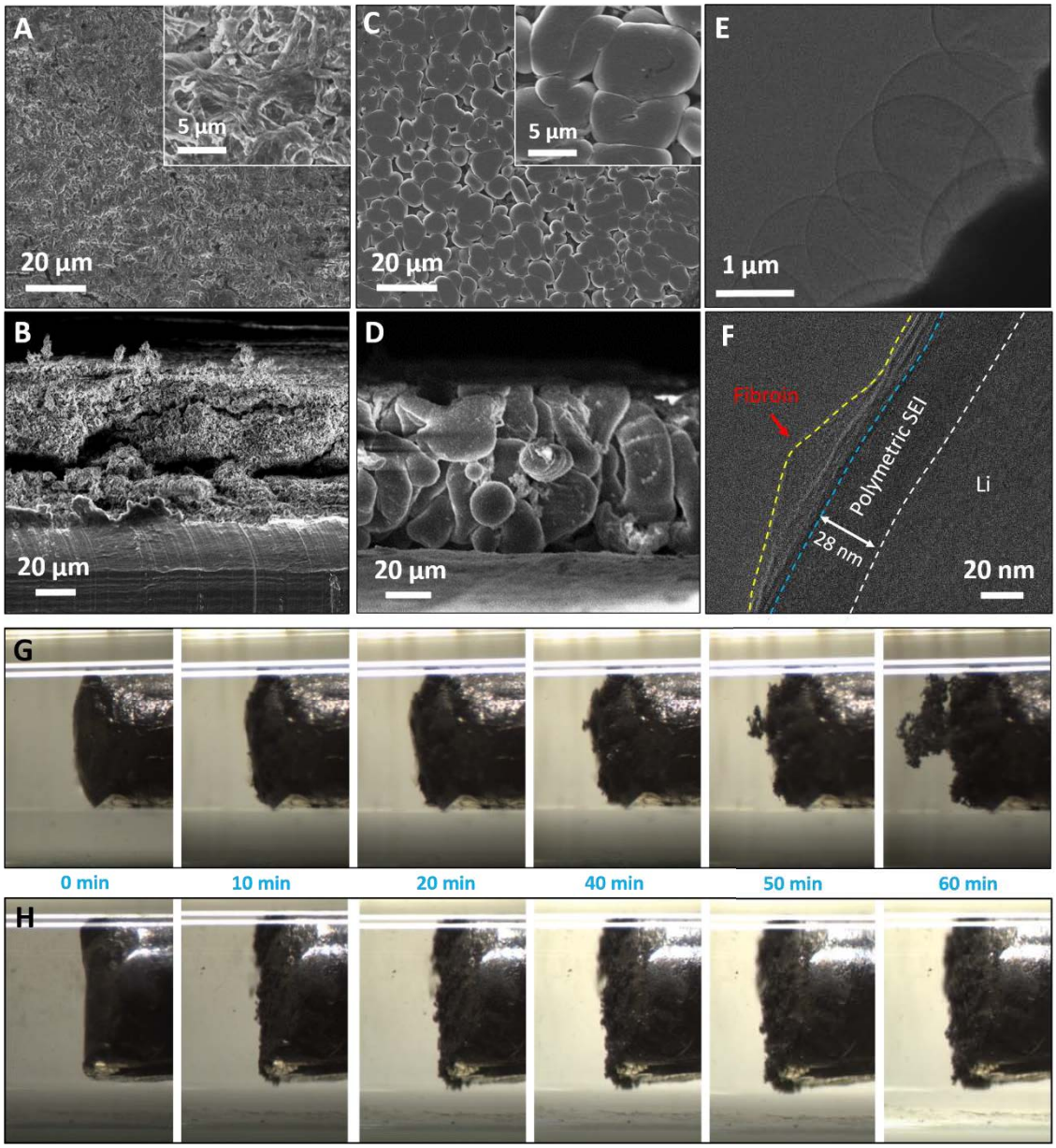

Figure 5.6 Characterization of Li deposition in ether-based electrolyte with fibroin additive. a, b Top-view (a) and cross-section (b) SEM images of Li metal anodes cycling in the cells with blank (i.e. no fibroin) electrolyte. **c, d** Top-view (c) and cross-section (d) SEM images of Li metal anodes cycling in the cells with fibroin additive in the electrolyte. The insets in (a) and (b) are the corresponding high magnification SEM images. Scale bars, (a-d) 20 µm and inserts in (a, c) 5µm. e, f Low-resolution (e) and high-resolution (f) cryo-EM images of Li deposit in the ether-based electrolyte with fibroin. Scale bars, (e) 1 µm and (f) 20 nm. The white line delineates the boundary between metallic Li and SEI. The

blue line delineates the boundary between adsorbed fibroin and SEI. The yellow line delineates the boundary between adsorbed fibroin and electrolyte. g, h *In situ* observations of Li deposition behavior in the glass capillaries filled with the blank electrolyte (g) and the electrolyte with fibroin (h) at a current density of 3 mA cm^{-2}. Scale bars, (g, h) 500 μm.

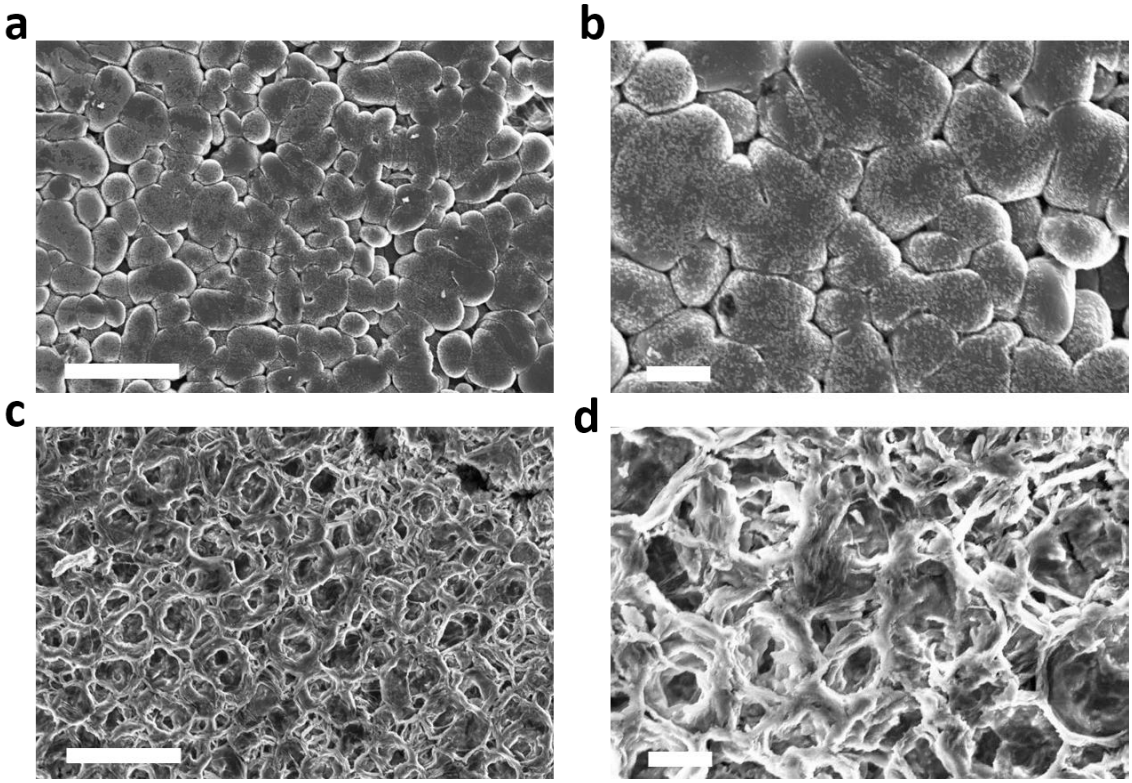

Figure 5.7 SEM images of Li metal surface after 100 cycles. a, b In the electrolyte with fibroin. **c, d** In the electrolyte without fibroin. The current density is 1 mA cm^{-2} and the capacity limitation is 1 mAh cm^{-2}. Scale bar, (a, c) 10 μm and (b, d) 2 μm.

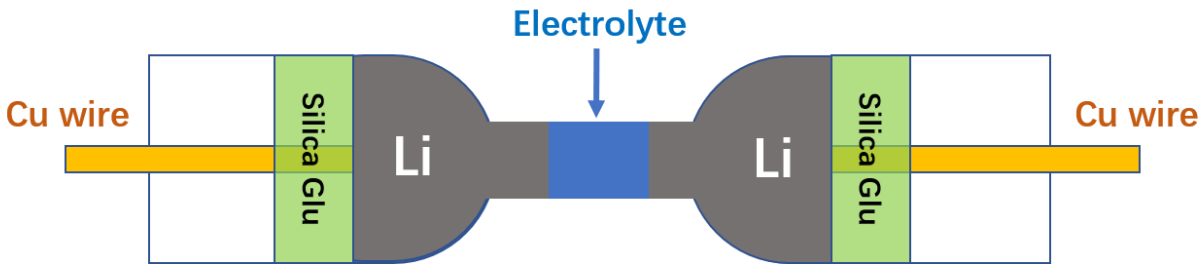

Figure 5.8 Schematic illustration of the configuration of Li | Li symmetric cells assembled in a homemade glass capillary.

5.3.3 Characterization of SEI with fibroin.

The physical and chemical properties of the SEI play a critical role in determining the overall electrochemical performance of Li metal anodes. Therefore, X-ray photoelectron spectroscopy (XPS) depth profiling investigations were conducted to examine the composition of SEI formed in the electrolyte with and without fibroin (**Figure 5.9**). The Li | Cu half cells were disassembled after 10 cycles in the stripped state to analyze the SEI formed on the Cu foil. To avoid the exposure to air, the samples were transferred into the XPS chamber using a sealed argon-filled vessel. In view of the similarity between the XPS spectra of the pristine fibroin **(Figure 5.10)** and SEI formed in the electrolytes with and without fibroin (**Figure 5.9**), it is obvious that the SEI formed in the electrolyte with fibroin additive contains fibroin molecule residue. The adsorbed protein molecules on the SEI layer were detected in the N 1*s* and C 1*s* spectra. As shown in **Figure 3.9 a**, compared with the SEI formed in the blank electrolyte, the N1*s* spectrum of the SEI formed in the electrolyte containing fibroin shows a new peak at 400 eV (colored in blue). This peak is consistent with the XPS N1*s* spectrum of the pristine fibroin (**Figure 5.10 c**). Meanwhile, **Figure 5.9 b** also shows that the intensity of the C 1*s* peak at 288.3 eV (corresponding to C=O) of the SEI formed in the electrolyte with fibroin

additive, is higher and larger. Therefore, we suggest that the enhanced C=O peak also comes from the fibroin molecules adsorbed on the surface of the Li metal anode. To investigate how fibroin additive affects the composition of the SEI, Ar^+ sputtering was employed to probe different depths of the SEI layer (**Figure 5.11**). With the increase of sputtering time, peaks in the N 1*s* spectra of the SEI layer formed in fibroin-saturated electrolyte are higher than those of the SEI formed in blank electrolyte (**Figure 5.9 a**). In particular, an extra peak at 402.8 eV corresponding to α-Li_3N appeared in the N 1*s* spectra. c-Li_3N has been widely observed in the SEI layer formed in ether-based electrolytes with $LiNO_3$ additive [159]. Compared with c-Li_3N, α-Li_3N facilitates the formation of a more mechanically stable SEI with high Li-ion conductivity [163, 164]. Furthermore, at different sputtering times, the peak from C = O bond in **Figure 5.9 b** was only detected in the SEI formed with fibroin additive. Therefore, fibroin and its decomposed products appear to be involved in the SEI formation. The peaks of O 1*s* (**Figure 5.9 c**) and F 1*s* (**Figure 5.9 d**) are similar for the SEI layers formed in the electrolytes with and without fibroin additive. According to the appearance of Cu 2*p* spectra (**Figure 5.12, 5.13**), the thickness of the SEI layer formed in the electrolyte with fibroin is higher than that of the SEI layer formed in the blank electrolyte, which is also consistent with the observation of the cryo-EM analyses.

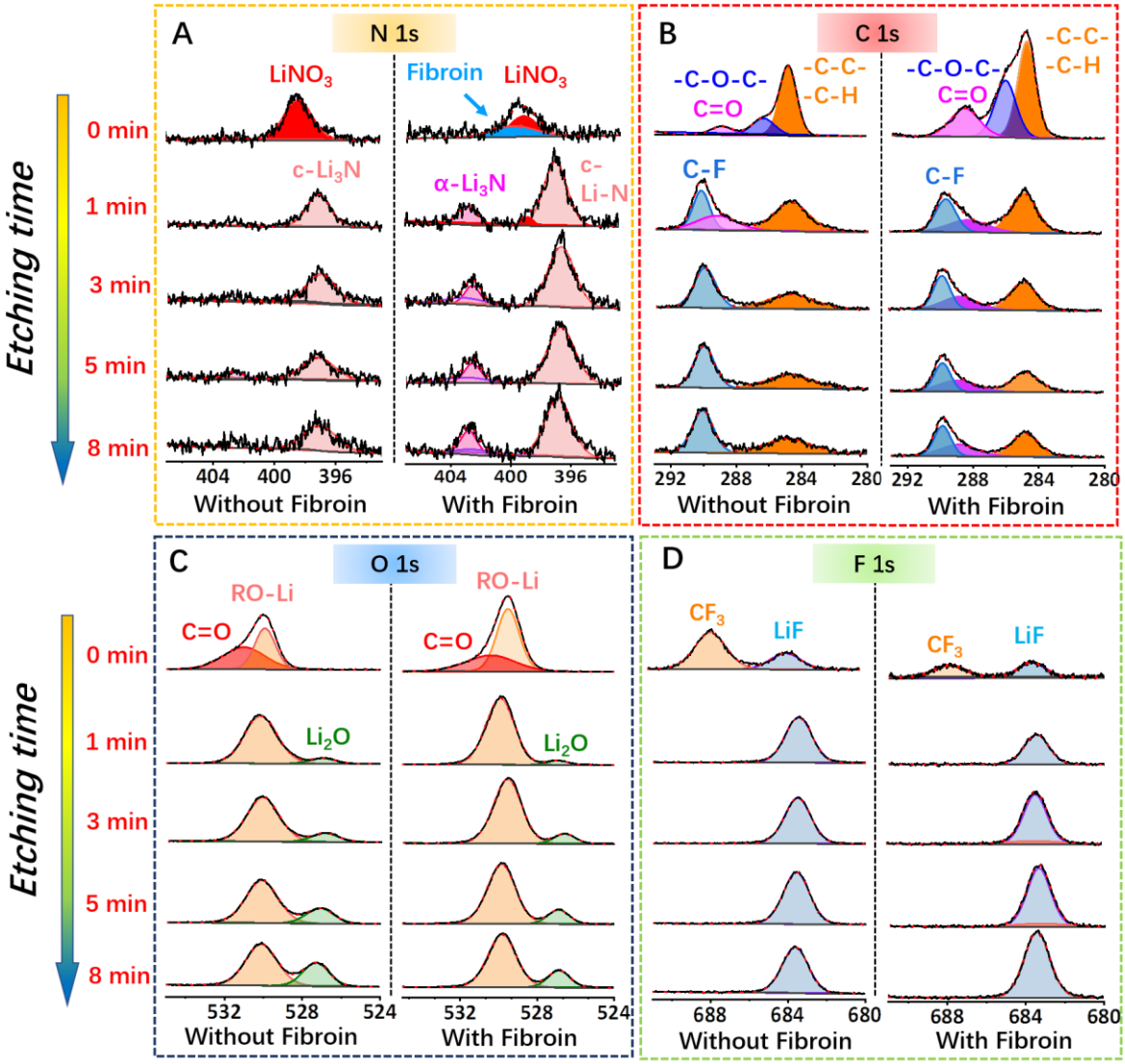

Figure 5.9 X-ray photoelectron spectroscopy (XPS) characterization of SEI formed in ether-based electrolyte with and without fibroin. Li deposition was carried out at a current density of 1mA cm^{-2} and a capacity of 1 mAh cm^{-2} on Cu foil for 10 cycles. (a) N1s spectra, (b) C1s spectra, (c) O1s spectra and (d) F1s spectra.

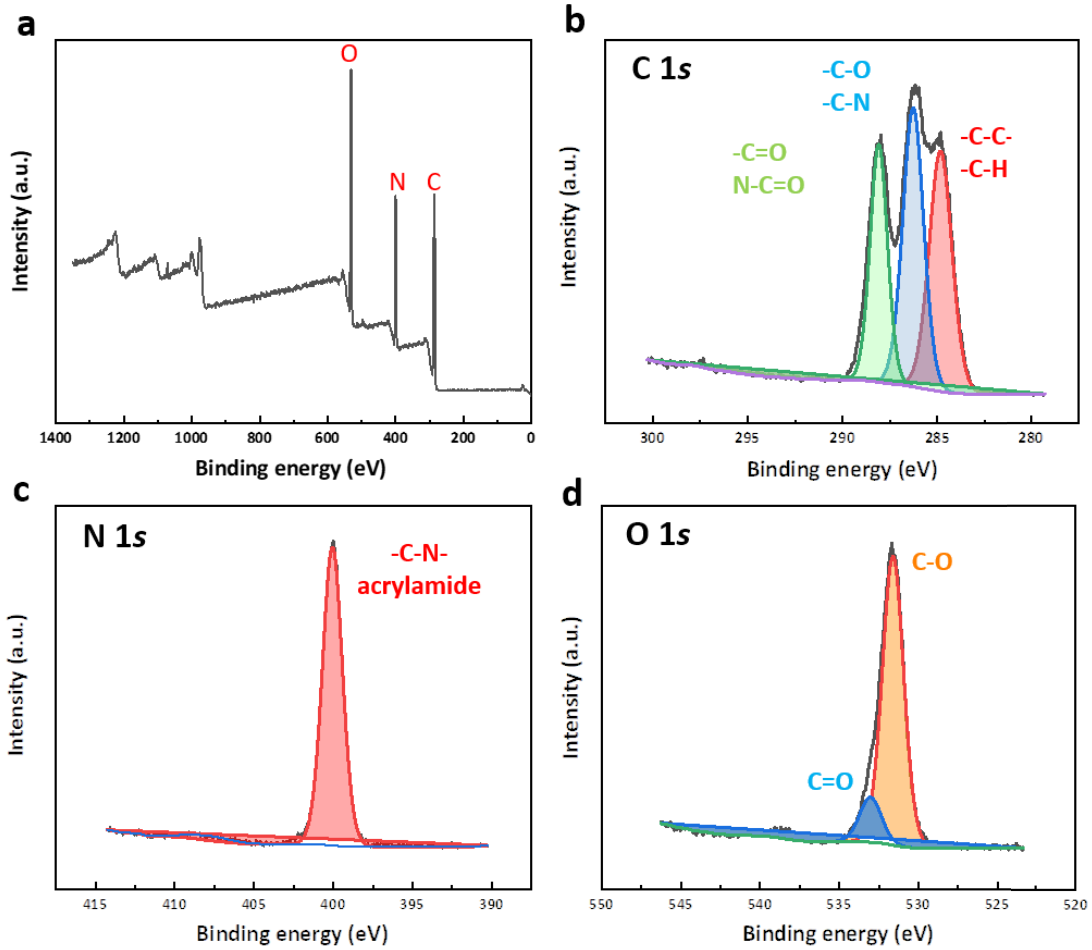

Figure 5.10 XPS spectra of pristine fibroin. (a) Survey spectrum. (b) C1*s* spectra. (c) N1*s* spectra. (d) O1*s* spectra.

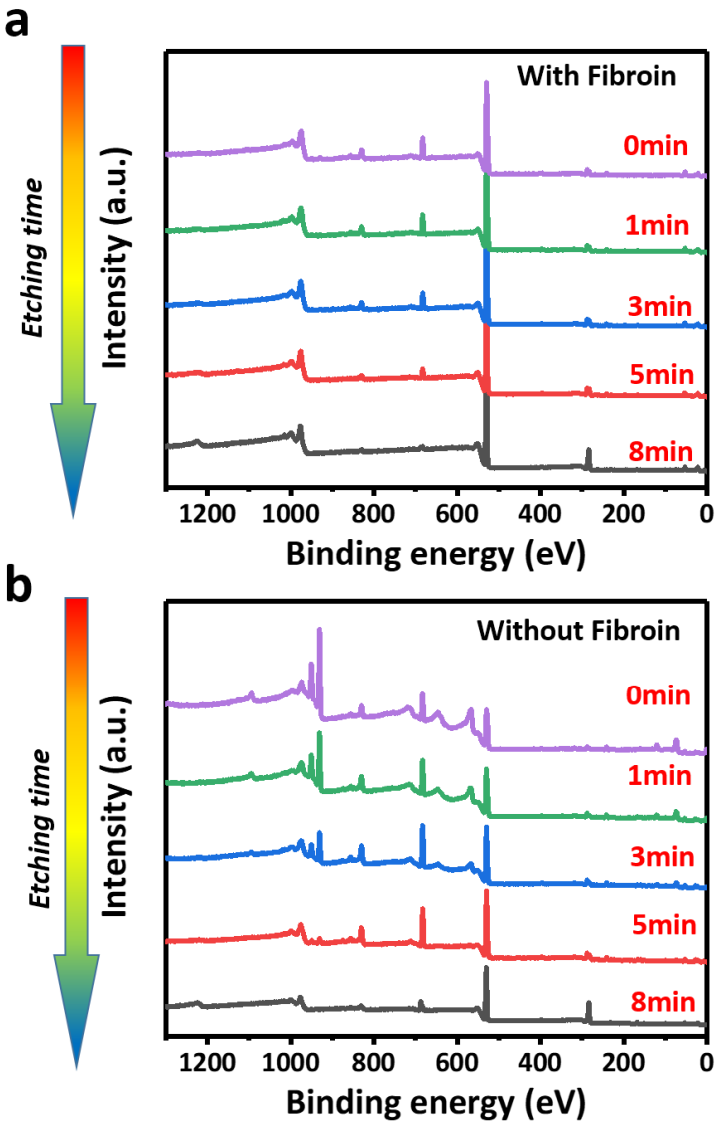

Figure 5.11 XPS spectra of cycled Li metal anode. XPS survey spectra of the SEI after different degrees of etching by Ar-ion sputtering (a) with and (b) without fibroin additive in the ether-based electrolyte.

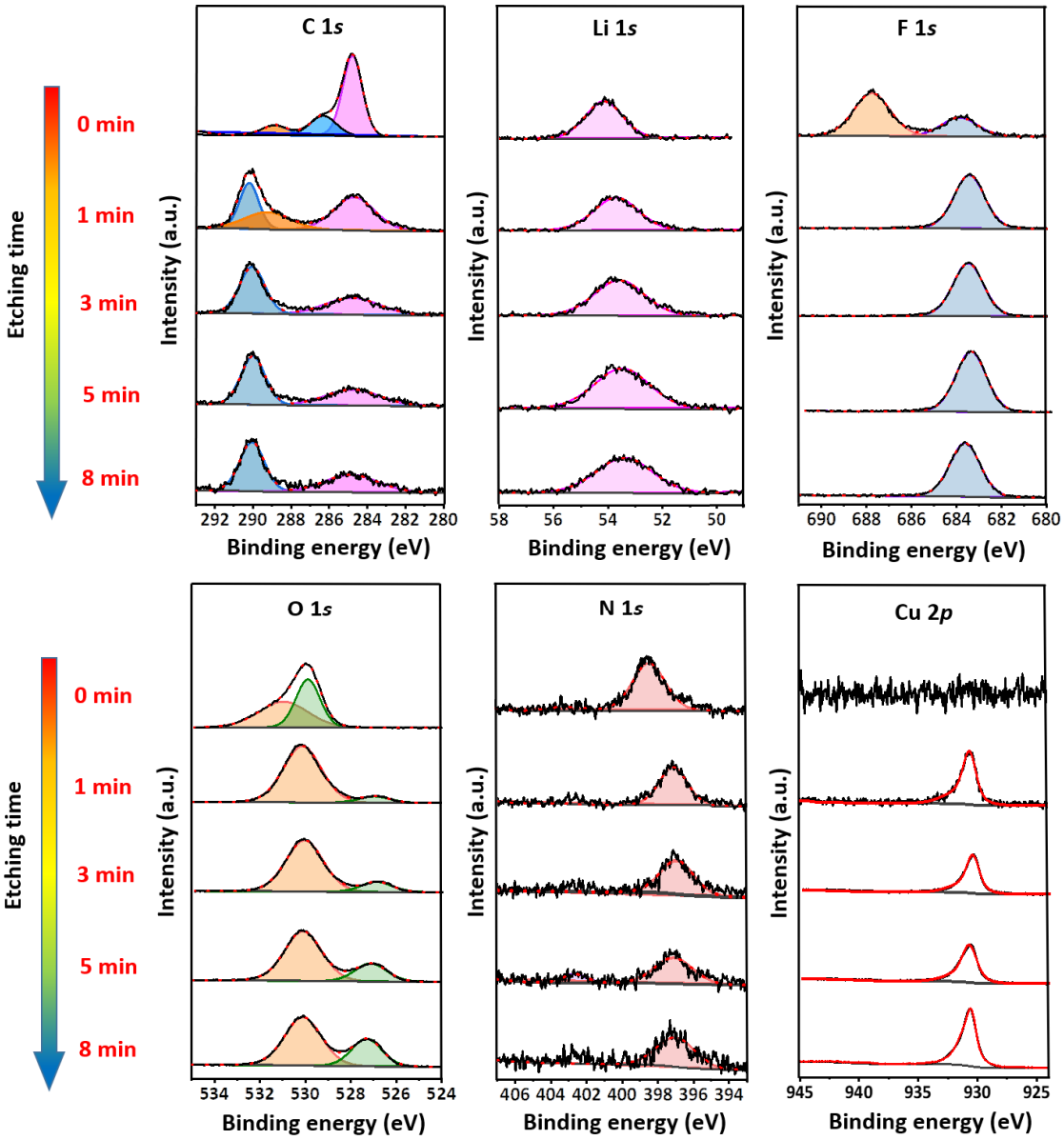

Figure 5.12 In-depth XPS profiles of the SEI formed in ether-based electrolyte without fibroin. Li deposition was carried out at a current density of 1mA cm^{-2} and a capacity of 1 mAh cm^{-2} on Cu foil for 10 cycles.

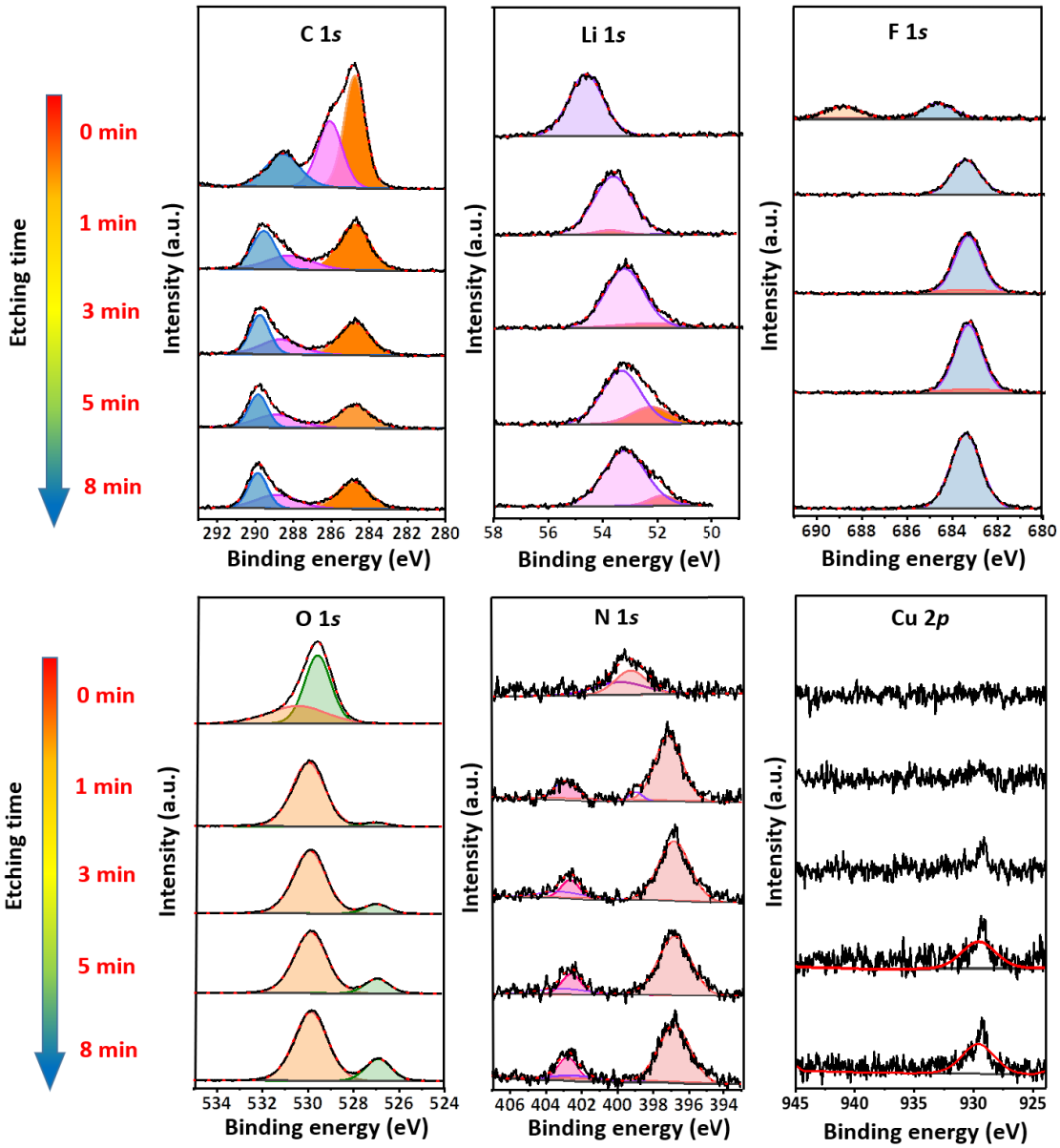

Figure 5.13 In-depth XPS profiles of the SEI formed in ether-based electrolyte with fibroin. Li deposition was carried out at a current density of 1mA cm^{-2} and a capacity of 1 mAh cm^{-2} on Cu foil for 10 cycles.

5.3.4 Electrochemical performance of Li anodes with fibroin.

We first tested Li | Cu cells using electrolytes with different concentrations of fibroin additive. As shown in **Figure 5.14**, after increase the fibroin concentration from 0.1 wt% to 0.5 wt%, the cycling stability of Li | Cu cells significantly improved. However, when we further increased the concentration

of fibroin to 1 wt%, the cycling stability was significantly decreased. The limited dispersibility of fibroin in ether-based electrolyte may be responsible for the degraded cycling performance. When the concentration of fibroin reached to 1 wt%, large amount of fibroin flakes cannot be well dispersed, and many small floccules were observed in the electrolyte. These suspended floccules may unevenly cover the Li metal surface during cell assembling process.

To overcome the dispersibility limitation of fibroin in ether-based electrolyte, we prepared a fibroin interlayer to sustainably release the protein molecules during cycling (**Figure 5.15**). The flexible fibroin interlayer consists of nanofibers with abundant micropores, which are beneficial for the absorption of the electrolyte and the release of fibroin (**Figure 5.16** and **5.17**). After immersed in the electrolyte for 3 days, the fibroin interlayer still maintains a good integrity and mechanical property, as shown in **Figure 5.18** and **Table 5.1**. The gelling process of fibroin nanofibers in the electrolyte can provide a tighter coverage on the Li metal anodes. **Figure 5.19 a** shows the voltage profiles of the symmetric Li | Li cells using ether-based electrolytes with and without fibroin interlayers at 3 mA cm^{-2} with the capacity limitation of 1 mAh cm^{-2}. The cells with fibroin interlayer exhibited stable voltage profiles over 1000 h. In contrast, the cells without a fibroin interlayer displayed a gradual capacity loss over cycling, and finally failed after 220 h. To further study the evolution of the voltage profiles, those of the symmetric cells at 0-2 h, 200-202 h, 800-802h and 1000-1002 h are further enlarged and presented as the inset in **Figure 5.19 a**. For the cells with fibroin interlayer, the flat voltage plateau during both plating and stripping remains steady throughout long-term cycling. As the current density increased to 5 mA cm^{-2} (**Figure 5.20**), a stable cycling beyond 160 h with stable hysteresis was attained, confirming the exceptional impact of the fibroin interlayer. As a sharp contrast, the cells without the fibroin interlayer exhibited a gradual hysteresis offset during plating/stripping processes. When the

capacity limitation was increased to 3 mAh cm^{-2} and 5 mAh cm^{-2}, only a slight increase in plating and stripping voltage hysteresis was observed for the cells with fibroin interlayer [165]. However, the cells without fibroin interlayer showed significant voltage hysteresis increases after cycling for 100h (**Figure 5.21**).

Coulombic efficiency is an important parameter to evaluate the cycling stability of Li metal anodes and is defined as the ratio between the amount of Li that is stripped from the working electrode and the amount of Li that is plated during each cycle. Considering the cycling life of batteries is related to the electrolyte decomposition upon the reaction with Li metal electrodes, a fair comparison of electrode performance was conducted using a controlled amount of electrolytes (~30 µl of electrolyte per coin cell). To investigate the influence of fibroin interlayer on the Coulombic efficiency of Li metal anodes, Li | Cu half-cells were tested. Li was firstly electrochemically deposited at 1 mAh cm^{-2} from the Li metal counter-electrode onto the fibroin interlayer-protected Cu working electrode and then stripped away during the following charge process. Since the Li metal counter-electrode has an excess of Li, the Coulombic efficiency reflects on the Li loss from the Cu working electrode. During cycling, the Li | Cu half cells without fibroin failed rapidly due to the generation of Li dendrites leading to the depletion of the electrolytes cause by the side reaction between the Li metal and the electrolytes. Thus, a gradual decrease in Coulombic efficiency was observed from 95% to lower than 40% after 100 cycles at the current density of 1 mA cm^{-2} (**Figure 5.19 b**, **c** and Supplementary **Figure 5.22 a**) and the voltage hysteresis increased upon cycling, with a large overpotential of ~37 mV after 100 cycles (**Figure 5.19 d**). As a contrary, the half cells with fibroin interlayers maintained the Coulombic efficiency as high as ~98% over 100 cycles at a current density of 1 mA cm^{-2} (**Figure 5.19 b, c** and **Figure 5.22 b**). Furthermore, the hysteresis of Li anodes remained stable at ~30 mV for more than 100 cycles (**Figure**

5.19 d). To study the stability of the SEI layer, we tested the electrochemical impedance spectroscopy (EIS) of Li | Cu half cells at the 1st and 50th cycle. As shown in **Figure 5.23**, the impedance of the cell with fibroin interlayer is much higher than that of the cell with blank electrolyte in the first cycle. After 50 cycles, the impedance of the cell with blank electrolyte significantly increase. In contrast, the impedance of the cell with fibroin interlayer almost unchanged, indicating significantly improved stability of SEI formed on Li metal anodes [166, 167].

5.3.5 Electrochemical performance of Li || $Li_4Ti_5O_{12}$ full cells.

We further evaluated the electrochemical performances of Li || $Li_4Ti_5O_{12}$ (LTO) full cells with or without the fibroin interlayer. To exclude the performance deterioration on cathodes, zero-strain LTO was used as the cathode materials. The full cells with fibroin interlayer consistently exhibited better cycling stability and rate capability than those without a fibroin interlayer (**Figure 5.19 e, f**). As shown in **Figure 5.19 e**, the capacity of the cells with bare Li anodes starts to decay after 800 cycles, indicating the depletion of active Li and liquid electrolyte. In contrast, the full cells with the fibroin interlayer maintained an excellent capacity over 2000 cycles. This discrepancy is further demonstrated by the voltage vs. capacity profiles of Li || LTO full cells (**Figure 5.24**). The voltage polarization of the full cells with bare Li anodes shows an obvious increase after 1000 cycles. However, the voltage polarization of full cells with fibroin interlayer-protected Li anode remains constant for 2000 cycles. Furthermore, as shown in **Figure 5.19**, the Li || LTO full cells with fibroin interlayer protected Li anodes maintain a good high rate capability, with a high specific capacity of ~102 mAh g^{-1} at 5 C and ~69 mAh g^{-1} at 10 C (xC = fully discharged within 1/x hours). By contrast, Li || LTO cells with blank electrolyte delivered a lower specific capacity of ~93 mAh g^{-1} and ~60 mAh g^{-1} at 5 C and 10 C, respectively.

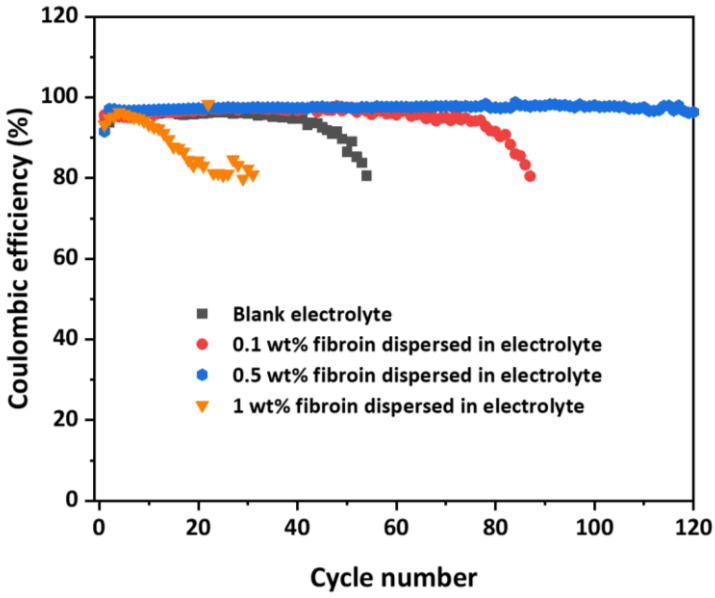

Figure 5.14 Comparison of Coulombic efficiencies of Li | Cu cells using electrolyte containing different concentrations of fibroin.

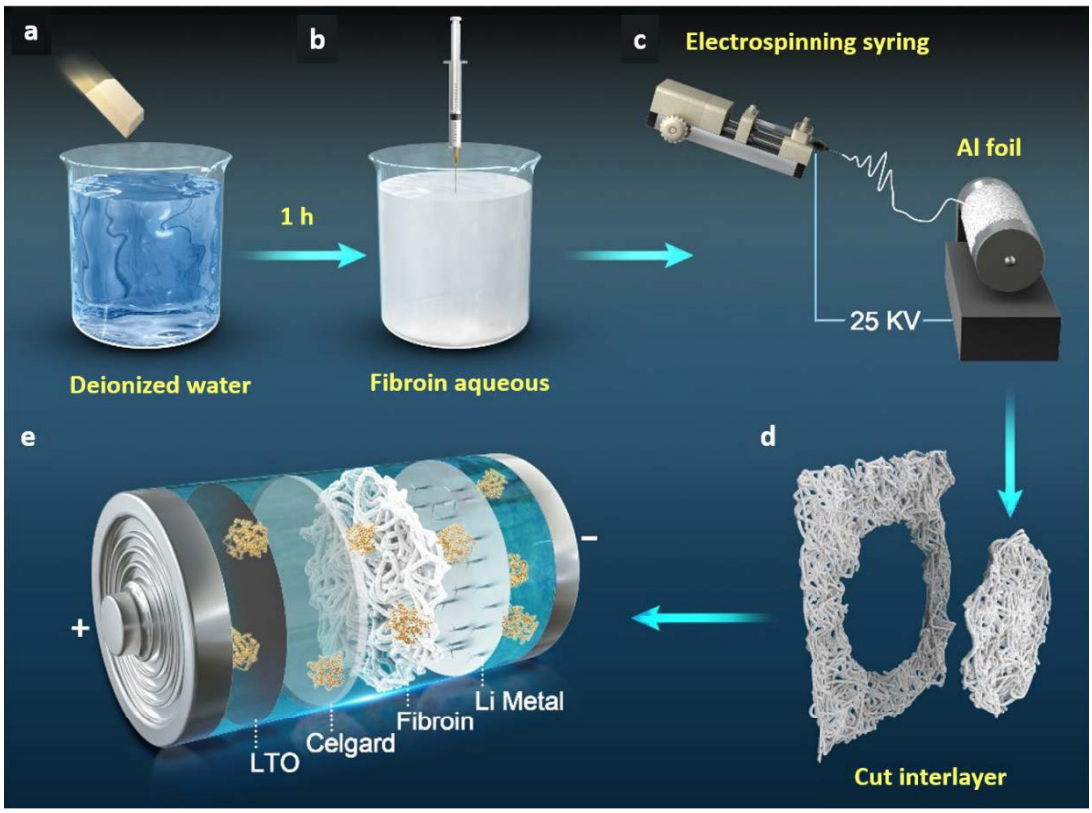

Figure 5.15 Schematic illustration of the synthesis process of fibroin interlayer. (a-d) Schematic illustration of electrospinning system for preparing a non-woven fibroin interlayer. (e) The architecture of Li metal battery using $Li_4Ti_5O_{12}$ (LTO) as cathode, one piece of fibroin interlayer between the Celgard^{TM} separator and Li metal anode.

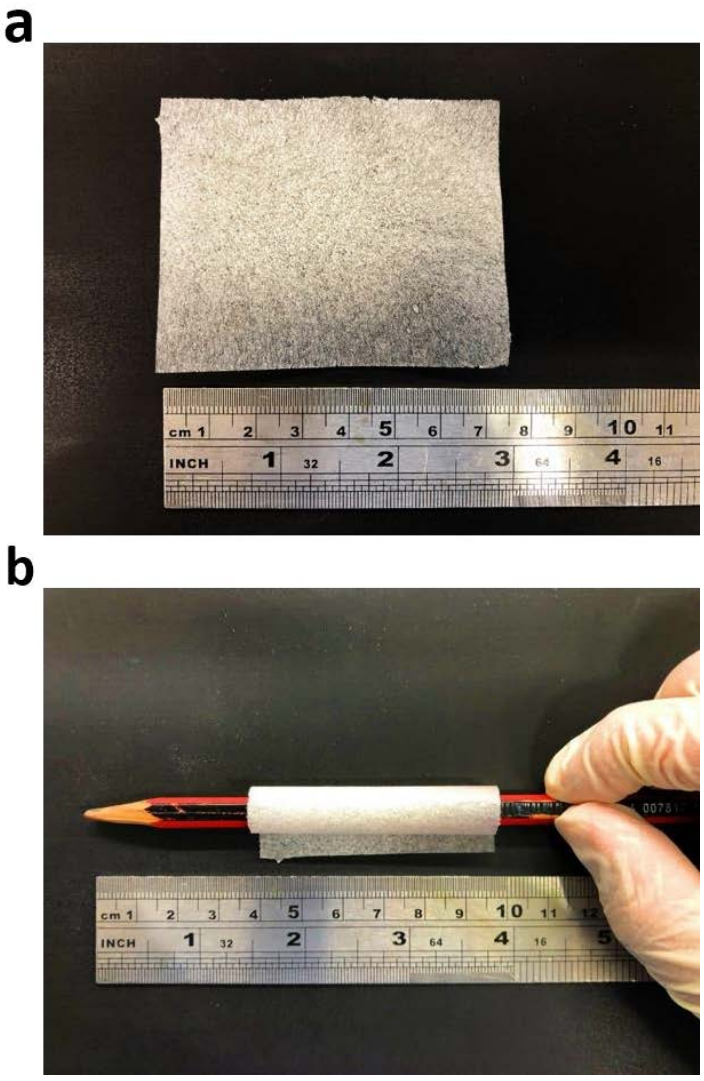

Figure 5.16 Digital photos of fibroin interlayer. (a) A piece of flat fibroin interlayer. (b) A piece of flexible fibroin interlayer wrap around a pencil.

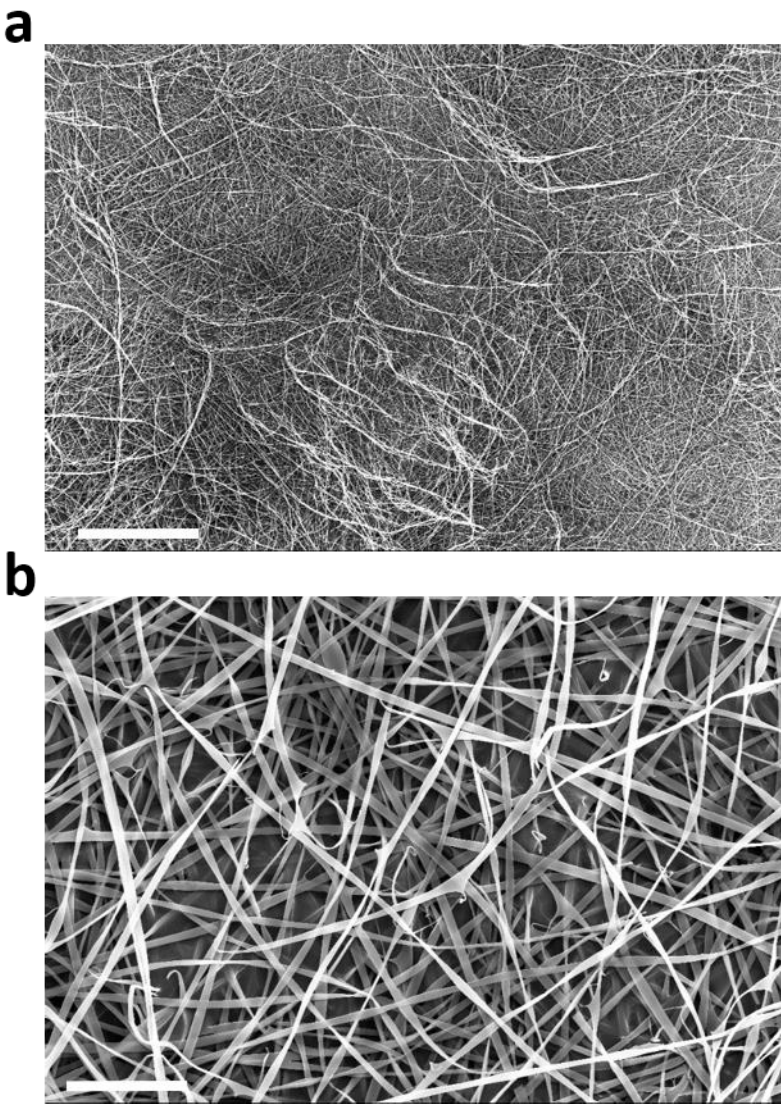

Figure 5.17 SEM observation of fibroin interlays. (a) Low magnification and (b) high magnification SEM images of an electrospun fibroin interlayer. The SEM images of the interconnected structure of fibroin interlayers show rich pore structure, contributing to its excellent flexibility and excellent wettability towards electrolytes. Scale bars, 10 μm.

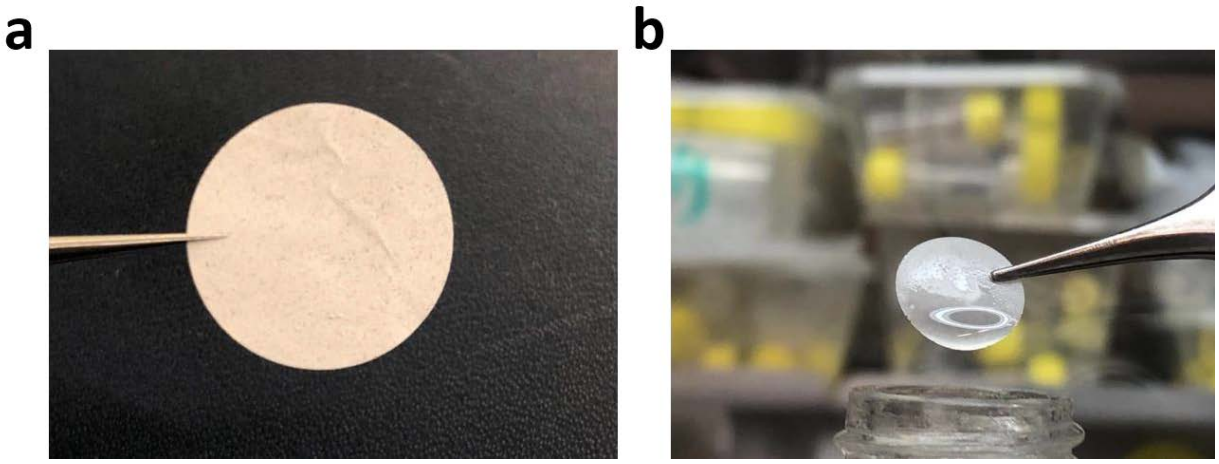

Figure 5.18 Stability test of fibroin interlayer in ether-based electrolyte. (a, b) Digital photos of (a) the pristine fibroin interlayer and (b) the fibroin interlayer retrieved from electrolyte after immersed for 3 days.

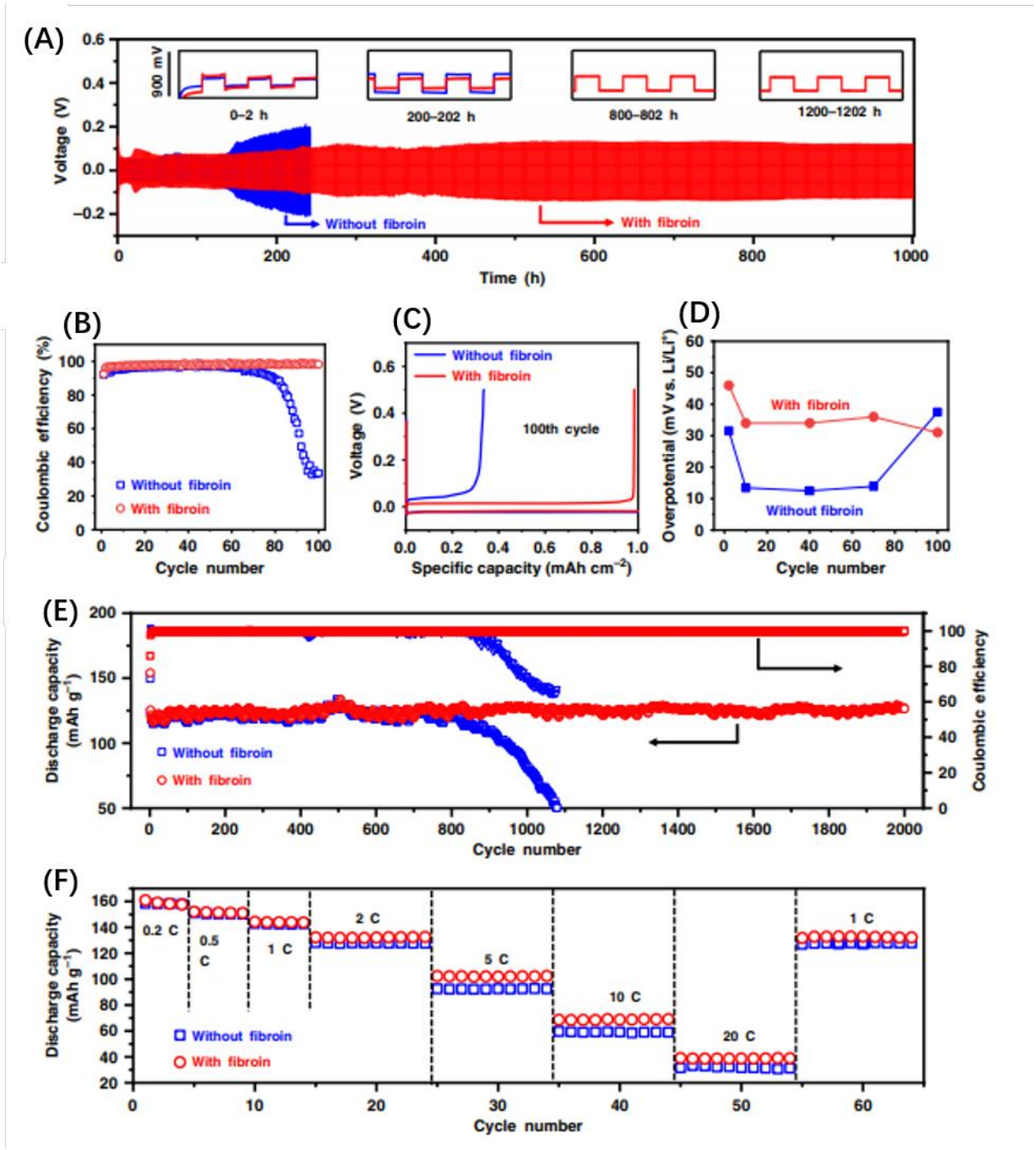

Figure 5.19 The electrochemical performance of Li anode in ether-based electrolyte with or without a fibroin interlayer. (a) Galvanostatic cycling of symmetric Li | Li cells with (blue line) or without (red line) a fibroin interlayer. The current density is fixed at 3 mA cm^{-2} with a plating/stripping capacity of 1 mAh cm^{-2}. Insets: The blow-up of voltage profiles during 0-2 h, 200-202 h, 800-802 h and 1000-1002 h, respectively. The y-axis scale of the insets is shown on the left. (b) Comparison of cycling

performances of Li | Cu half cells with or without a fibroin interlayer between Cu foil and separator. The amount of Li deposited in each cycle is 1 mAh cm^{-2} and the current density is 1 mA cm^{-2}. (c) The corresponding voltage profiles at the 100^{th} cycle of the Li plating/stripping processes on Cu foil with or without a fibroin interlayer. (d) Comparison of the hysteresis of Li plating/stripping for cells with or without interlayers. **e** Long-term cycling stability of the Li || LTO full cells with or without a fibroin interlayer at a current density of 2 C (1C =175 mA g^{-1}). **f** Rate capabilities from 0.2 C to 10 C of the Li | LTO cells with or without fibroin additive in the electrolytes.

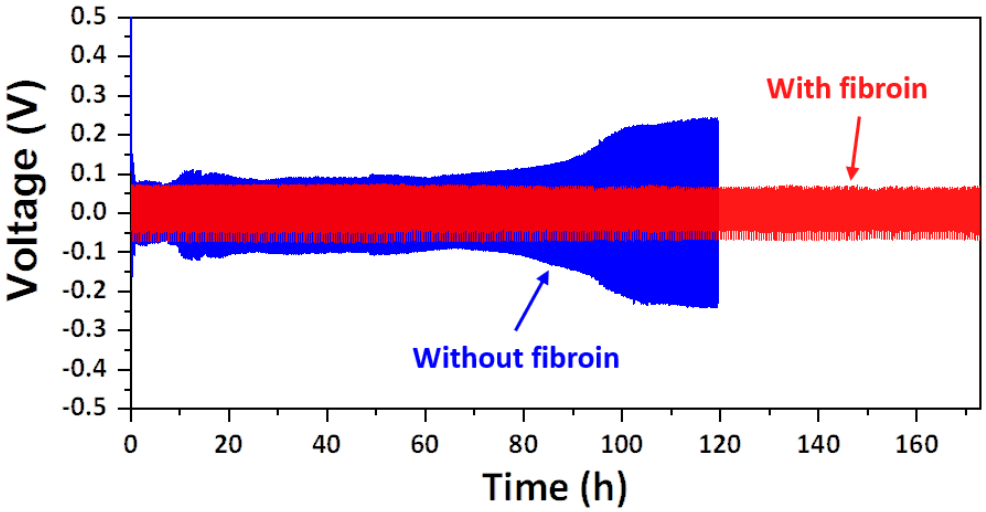

Figure 5.20 The cycling stability of Li | Li symmetrical cells at a high current density. A current density of 5 mA cm^{-2} and a capacity of 1 mAh cm^{-2} were applied.

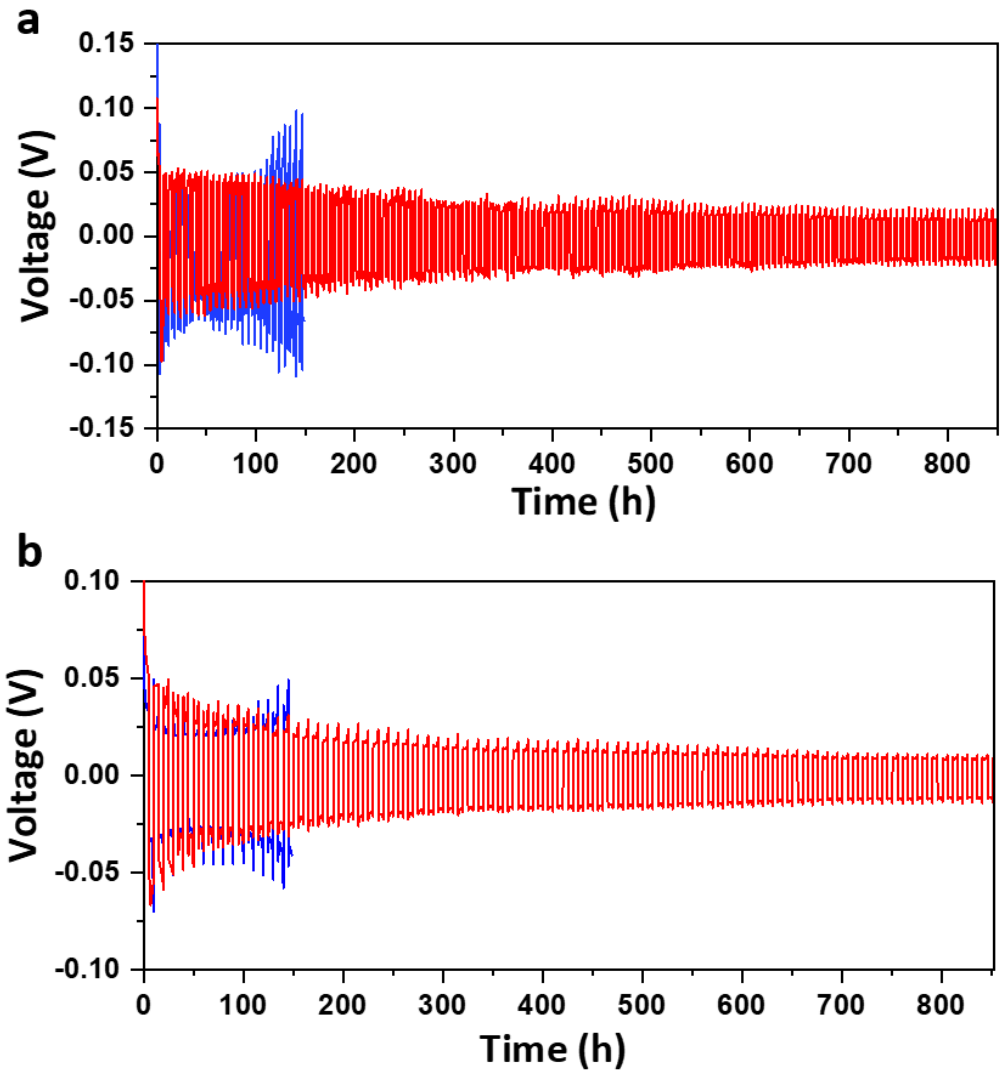

Figure 5.21 Comparison of the cycling stability of Li | Li symmetrical cells at high capacities. (a) The capacity limitation is 3 mAh cm^{-2} and the current density is 1 mA cm^{-2}. (b) The capacity limitation is 5 mAh cm^{-2} and the current density is 1 mA cm^{-2}.

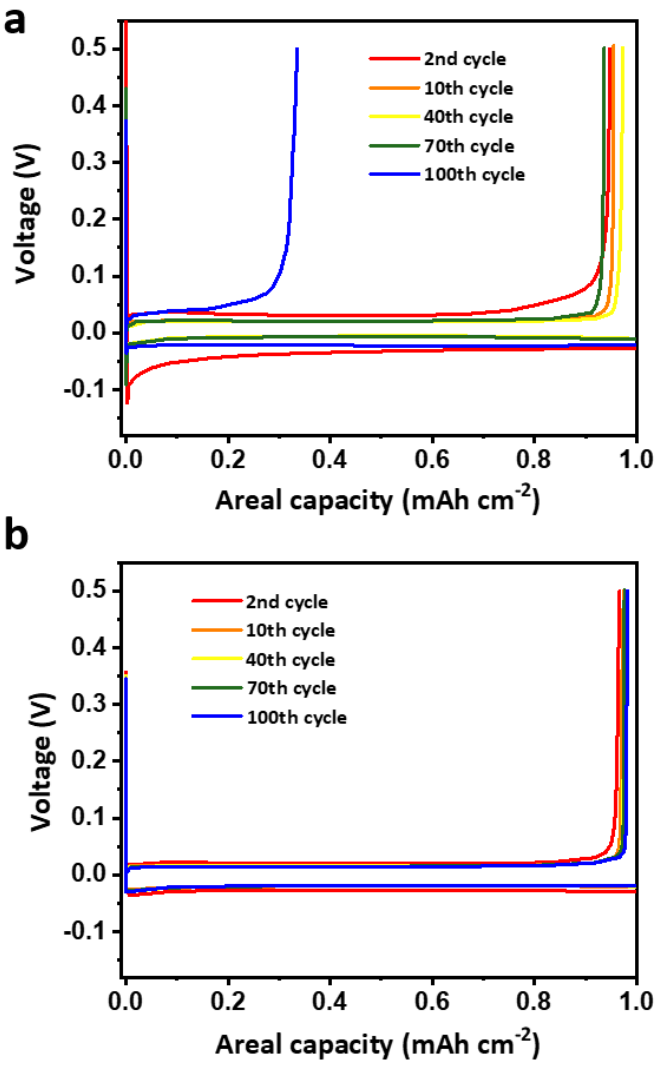

Figure 5.22. Comparison of the cycling performances of Li | Cu half cells. The voltage profiles of Li plating/striping on Cu foils at different cycles (a) without and (b) with fibroin interlayer.

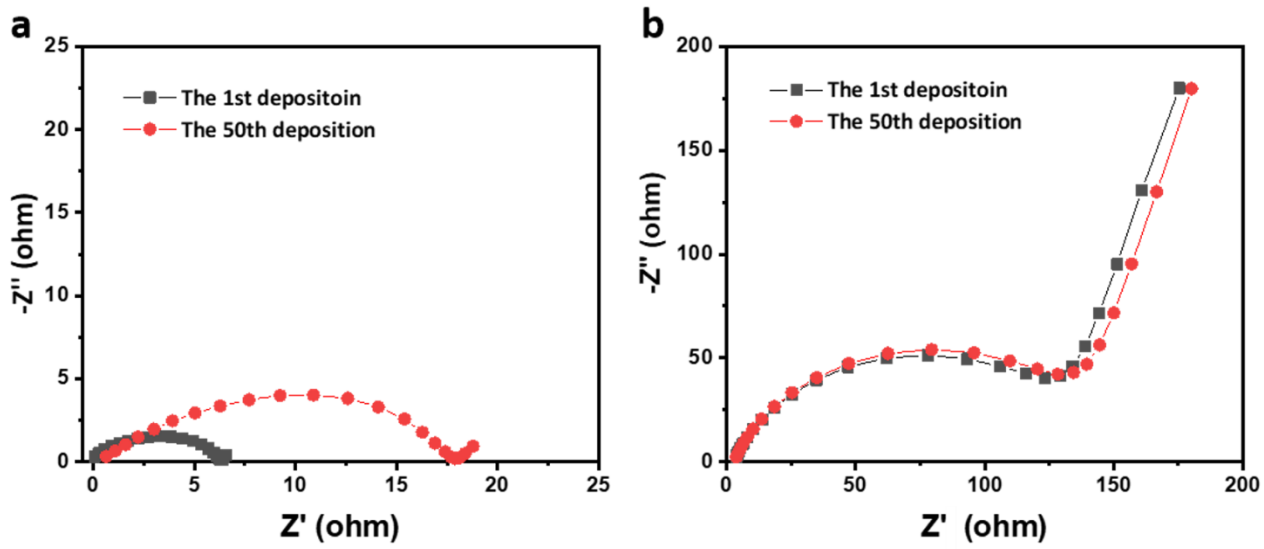

Figure 5.23 The EIS measurement of Li | Cu half cells at different cycles. (a) without and (b) with the fibroin interlayer at the current density of 1 mA cm^{-2} with the capacity imitation of 1 mAh cm^{-2}.

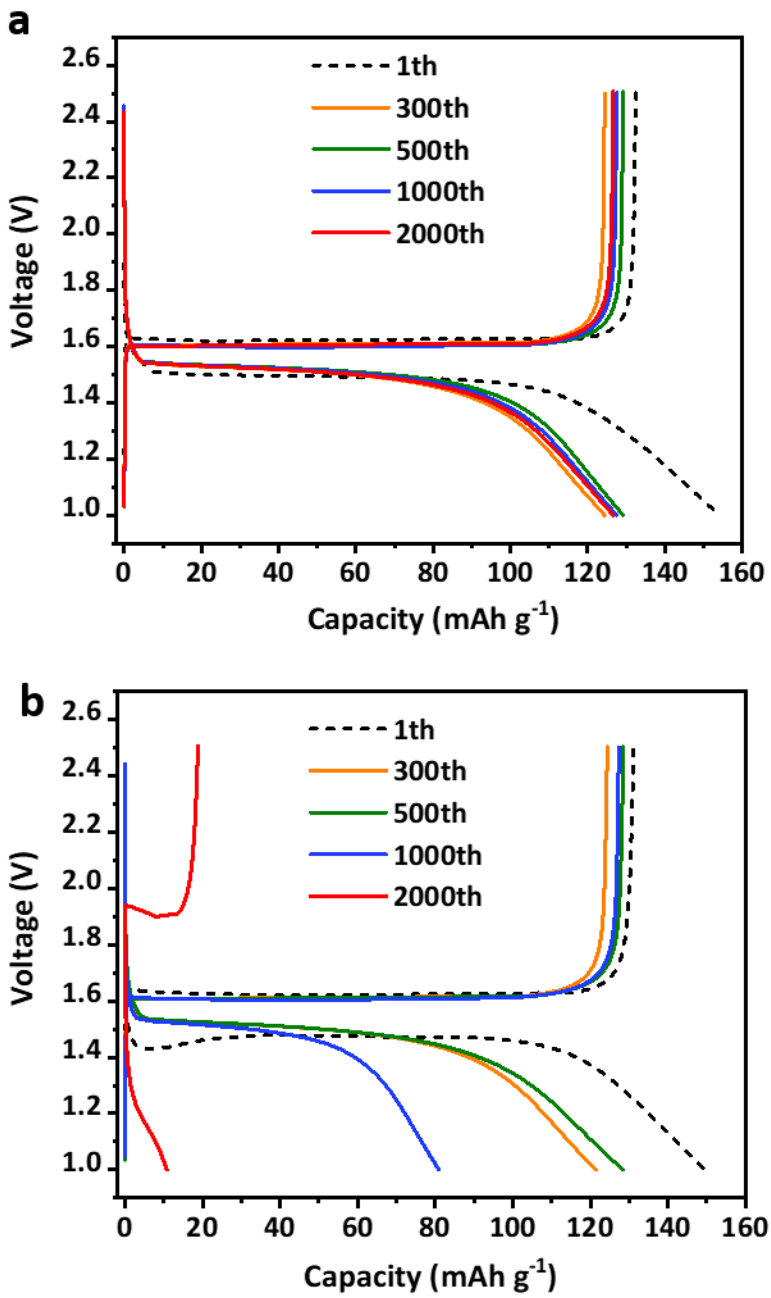

Figure 5.24 Cycling performance of Li || LTO full cells. Galvanostatic charge/discharge curves of Li || LTO full cells (a) with and (b) without fibroin interlayer.

Table 5.1 Comparison of mechanical properties of fibroin interlayer before and after immersed in ether-based electrolyte.

Fibroin interlayer	Tensile strength (Mpa)	Elongation at break (%)	Young's modulus (Mpa)
Dry electrolyte	8.1±2.4	18.1±2.5	167±35
After immersed in electrolyte for 3 days	12.9±3.1	24.2±1.7	115±12

5.4 Conclusion

In conclusion, we have developed an innovative Li anode self-defense strategy inspired by natural immunization mechanisms to eliminate Li dendrite growth and thereby improve the electrochemical performance of Li metal batteries. The natural protein fibroin can effectively prevent Li dendrite nucleation and growth by blocking the evolution of the Li buds in the initial stage. These protein molecules preferably adsorb on Li buds through spatial conformation and secondary structural transformation that significantly affect the local electric field intensity. Therefore, the following Li nuclei will deposit further from the tips of Li buds, leading to a leveling out of Li deposition. Furthermore, to overcome the dispersibility limitation of fibroin in ether-based electrolytes, fibroin interlayers were fabricated to continuously release fibroin in the electrolyte. When applied in a Li||LTO battery, long-term cycling stability is achieved, and high specific capacity is delivered even at high rate. The remarkable advantages of this self-defense mechanism enabled by natural protein molecules open up a new and sustainable avenue to achieve safe and dendrite-free high-energy-density lithium metal batteries.

Chapter 6 Conclusion and future perspective

Currently, accompanied by the large consumption of fossil energy, the research on regenerated sources has been accelerated. However, the development of energy storage technology can not keep up with the rapid development of energy conversion technology, no matter in the domain of energy density, safety problems or working stabilities. The emergence of lithium sulfur battery brings a glimmer of hope to the research of energy storage technology. Be different from commercial Li ion batteries, the mechanism of Li-S batteries makes them have large discharge capacity, higher energy density and environmentally benign. However, the severe “shuttle effect” of cathodes and out of control of growth of Li dendrites on Li metal anode is still limiting the real application of Li-S batteries. In our thesis, nanomaterials were effectively employed to improve electrochemical performances of Li-S batteries, including longer service life, larger charge-discharge capacity, higher energy density and safer service status.

For cathodes, we designed a series of biomimetic 3D CNT scaffold which can be employed as an ideal sulfur holder matrix. According to changing the ratio of precursors and the calcination temperature, we can effectively control the morphology of the matrix and thus prepare a three-dimensional CNT structure with simulated marine morphology. During the calcinating process, Fe and CeO_2 were formed successively in a high temperature, in which Fe acted as the catalyst of CNT and CeO_2 acted as the catalyst which can largely improve the catalyst efficiency of CNT. Not only that, the spacious interspace is an ideal space for storing sulfur. When mixed with sulfur and prepared as cathodes, these cathodes demonstrated higher charge-discharge capacity, better rate performances (especially at high current densities) and better cycling stability. XPS characterization confirms that doped Fe and CeO_2 demonstrated strong adsorption ability to dissolved lithium polysulfides, hence

effectively reduce the “shuttle effect”. The abundant N doping not only greatly improves the conductivity of 3D matrix but also support many active spots for anchoring polysulfides. In particle use, this kind of 3D CNT scaffold can adsorb dissolved polysulfides, which is similar to the predation process of coral or sea cucumber. This research confirms that there is still much potential for the development of biomimetic materials for Li-S batteries.

For anodes, we firstly systematically investigate the utilization of biomacromolecules for the protection of Li metal. We have found that fibroin can effectively protect the surface of Li metal, strengthen the chemical/physical properties of SEI layer, stabilized the electrochemical reaction of Li metal anodes, hence alleviate the growth of Li dendrites. When using the electrospinning method to fabricate a fibroin layer on the surface of Li metal anode, the low solubility of fibroin can be solved. The fibroin interlayer could endlessly release fibroin molecules to keep an ideal concentration in the electrolyte. Furthermore, according to the characterization of the structure of the protein, it can be confirmed that the protein molecules can selectively immobilize on the tips, edges or other defects of Li metal and persuade the flow of Li ions by changing the distribution of the electric field. As a sacrifice, the secondary structure of protein was shift which transformed from α-helix to β-sheet. The shift of secondary structure could extensively reduce the solubility of fibroin, hence furtherly prevent them from returning electrolyte.

To date, nanotechnologies have been undoubtedly widely and deeply used in the field of Li-S battery. Thanks to the unique properties of nanomaterials, some in-born defects of Li-S battery can be greatly overcome. Accompanied by the development of nanomaterials and importance of environmental protection, we believe that the combination of nanomaterials and biology to extract inspiration from nature will be an important direction of Li-S battery development in the future. For

cathodes, future research can be focused on constructing carbonaceous biomimetic nanostructure with different heteroatom doping. For the biomimetic structure or topological structure inspired by the biological field, it is expected to effectively improve the conductivity of Li-S battery cathode and inhibit the volume expansion during the lithiation, so as to improve the discharge capacity and sulfur usage efficiency and improve the cycling stability of Li-S batteries. For anodes, the design of future protection strategies can be inspired by introducing some biomaterials into Li metal batteries as electrolyte additives. These introduced biomaterials should have merits on green, environmental protection, cheap, more importantly, can be integrated into the composition of SEI layer. They can not only improve the mechanical properties, chemical stability but also strengthen the electrochemical performances of SEI layers. It can be predicted that in the future, the link between biopolymers such as protein and energy storage will be more prosperous in the next decade.

REFERENCES

[1] V. Palomares, P. Serras, I. Villaluenga, K. B. Hueso, J. Carretero-González, T. Rojo, *Energy Environ. Sci.,* 2012, ***5***, 5884-5901.

[2] F. Wu, J. Qian, R. Chen, J. Lu, L. Li, H. Wu, J. Chen, T. Zhao, Y. Ye, K. Amine, *ACS Appl. Mater. Interfaces,* 2014, ***6***, 15542-15549.

[3] A. Vizintin, M. U. M. Patel, B. Genorio, R. Dominko, *ChemElectroChem,* 2014, ***1***, 1040-1045.

[4] K. Liu, Y. Lin, J. D. Miller, J. Liu, X. Wang, *J. Electrochem. Soc.,* 2017, ***164***, A447-A452;

[5] E. Peled, H. Yamin, *Power Sources,* 1981, ***8***, 101-115

[6] J. Luo, R.-C. Lee, J.-T. Jin, Y.-T. Weng, C.-C. Fang, N.-L. Wu, *Chem. Commun.,* 2017, ***53***, 963-966.

[7] Z. She, Y. Sun, Q. Zhang, Y. Cui, *Chem. Soc. Rev.,* 2016, ***45***, 5605-5634.

[8] R. Cao, W. Xu, D. Lv, J. Xiao, J.-G. Zhang, *Adv. Energy Mater.,* 2015, ***5***, 1402273.

[9] A. Vizintin, M. Patel, B. Genorio, and R. Dominko. *ChemElectroChem*, 2014, ***1***, 1040–1045.

[10] K. Liu, Y. Lin, J.D. Miller, J. Liu, and X. Wang, *J. Electrochem. Soc.,* 2017, ***164***, A447-A452.

[11] J. Luo, R. Lee, J. Jin, Y. Weng, C. Fang, N. Wu, *Chem. Commun.,* 2017, ***53***, 963–966.

[12] E. Peled, H. Yamin *J. Power Sources,* 1981, ***8***, 101–115.

[13] R. Cao, W. Xu, D. Lv, J. Xiao, and J. Zhang, *Adv. Energy Mater.* 2015, ***5***, 1402273–1402295.

[14] K.A. See, H. Wu, K. Lau, M. Shin, L. Cheng, M. Balasubramanian, K. Gallagher, L. Curtiss, and A. Gewirth, *ACS Appl. Mater. Interfaces.,* 2016, ***8***, 34360–34371.

[15] Z. Zhang, Q. Li, K. Zhang, W. Chen, Y. Lai, and J. Li, *J. Power Sources.,* 2015, ***290***, 159–167.

[16] G. Zhou, D. Wang, F. Li, P. Hou, L. Yin, C. Liu, G. Lu, I. Gentle, and H. Cheng. *Energy Environ. Sci.,* 2012, ***5***, 8901–8906.

[17] L. Zeng, F. Pan, W. Li, Y. Jiang, X. Zhong, and Y. Yu, *Nanoscale,* 2014, ***6***, 9579–9587.

[18] L. Zeng, W. Zeng, Y. Jiang, X. Wei, W. Li, C. Yang, Y. Zhu, and Y. Yu. *Adv. Energy Mater.,* 2015, ***5***, 1401377–1401386.

[19] S. Thieme, J. Brueckner, I. Bauer, M. Oschatz, L. Borchardt, H. Althues, and S. Kaskel. *J. Mater. Chem. A,* 2013, ***1***, 9225–9234.

[20] C. Wang, K. Su, W. Wan, H. Guo, H. Zhou, J. Chen, X. Zhang, and Y. Huang, *J. Mater. Chem. A,* 2014, ***2***, 5018–5023.

[21] H. Wang, W. Zhang, H. Liu, and Z. Guo. *Angew. Chem. Int. Ed.* 2016, ***55***, 3992–3996.

[22] K. Lee, R. Black, T. Yim, X. Ji, and L. Nazar, *Adv. Energy. Mater.* 2012, ***2***, 1490–1496.

[23] D. Li, F. Han, S. Wang, F. Cheng, Q. Sun, and W. Li. *ACS Appl. Mater. Interfaces,* 2013, ***5***, 2208–2213.

[24] Y. Chen, S. Lu, X. Wu, and J. Liu, *J. Phys. Chem. C,* 2015, ***119***, 10288–10294.

[25] Q. Sun, X. Fang, W. Weng, J. Deng, P. Chen, J. Ren, G. Guan, M. Wang, and H. Peng, *Angew. Chem. Int. Ed.,* 2015, ***54***, 10539–10544.

[26] L. Sun, W. Kong, Y. Jiang, H. Wu, K. Jiang, J. Wang, and S. Fan, *J. Mater. Chem. A,* 2015, ***3***, 5305–5312.

[27] C. Wang, X. Wang, Y. Wang, J. Chen, H. Zhou, and Y. Huang, *Nano Energy,* 2015, ***11***, 678–686.

[28] X. Song, S Wang, Y. Bao, G. Liu, W. Sun, L. Ding, H. Liu, H. Wang, *J. Mater. Chem. A,* 2017, ***5***, 6832–6839.

[29] Y. Guo, G. Zhao, N. Wu, Y. Zhang, M. Xiang, B. Wang, H. Liu, and H. Wu, *ACS Appl. Mater. Interfaces,* 2016, ***8***, 34185–34193.

[30] C. Lin, C.J. Niu, X. Xu, K. Li, Z.Y. Cai, Y.L. Zhang, X.P. Wang, L.B. Qu, Y.X. Xu, and L.Q. Mai, *Phys. Chem. Chem. Phys.,* 2016, ***18***, 22146–22153.

[31] Z.A. Ghazi, X. He, A.M. Khattak, NA Khan B. Liang, A. Iqbal, J. Wang, H. Sin, L. Li, and Z. Tang, *Adv. Mater.,* 2017, ***29***, 1606817–1606822.

[32] Y.B. An, Q.Z. Zhu, L.F. Hu, S.K. Yu, Q. Zhao, and B. Xu, *J. Mater. Chem. A,* 2016, ***4***, 15605–15611.

[33] J. Song, Z. Yu, T. Xu, S. Chen, H. Sohn, M. Regula, and D. Wang, *J. Mater. Chem. A,* 2014, ***2***, 8623–8627.

[34] C. Milroy, and A Manthiram, *Adv. Mater.,* 2016, ***28***, 9744–9751.

[35] A. Ghosh, R. Manjunatha, R. Kumar, S. Mitra, *ACS Appl. Mater. Interfaces,* 2016, ***8***, 33775–33785.

[36] C. Wang, X. Wang, Y. Yang, A. Kushima, J. Chen, Y. Huang, and J. Li, *Nano Lett.,* 2015, ***15***,

1796–1802.

[37] J. He, Y. Chen, W. Lv, K. Wen, C. Xu, W. Zhang, W. Qin, and W. He, *ACS Energy Lett.,* 2016, ***1***, 820–826.

[38] J. He, Y. Chen, W. Lv, K. Wen, Z. Wang, W. Zhang, Y. Li, W. Qin, and W. He, *ASC Nano,* 2016, ***10***, 8837–8842.

[39] Y. Huang, M. Zheng, Z. Lin, B. Zhao, S. Zhang, J. Yang, C. Zhu, H. Zhang, D. Sun, and Y. Shi, *J. Mater. Chem. A,* 2015, ***3***, 10910–10918.

[40] M. Armand, and J. Tarascon *Nature,* 2008, ***451***, 652–657.

[41] S. Chen, Y. Xin, Y. Zhou, Y. Ma, H. Zhou, and L. Qi, *Energy Environ. Sci.,* 2014, ***7***, 1924–1930.

[42] R. Khurana, J. Schaefer, L. Archer, and G. Coates, *J. Am. Chem. Soc.,* 2014, ***136***, 7395–7402.

[43] S. Ramesh, and M. Chai, *Mater. Sci. Eng.*, 2007, ***139***, 240–245.

[44] S. Ramesh, T. Winie, and A. Arof, *Eur. Polym. J.*, 2007, ***43***, 1963–1968.

[45] J. Tarascon, and M. Armand, Issues and challenges facing rechargeable lithium batteries. *Nature,* 2001, ***414***, 359–367.

[46] Y. Zhang, Y. Zhao, and Z. Bakenov, *Nanoscale Res. Lett.,* 2014, ***9***, 137–143.

[47] Y. Zhao, Y. Zhang, Z. Bakenov, and P. Chen, *Solid State Ionics,* 2013, ***234***, 40–45.

[48] M. Liu, D. Zhou, Y. He, Y. Fu, X. Qin, C. Miao, H. Du, B. Li, Q. Yang, Z. Lin, *Nano Energy,* 2016, ***22***, 278–289.

[49] C. Barchasz, F. Molton, C. Duboc, J. C. Lepretre, S. Patoux, and F. Alloin, *Anal. Chem.,* 2012, ***84***, 3973–3980.

[50] J. Gao, M. Lowe, Y. Kiya, and H. Abruna, *J. Phys. Chem. C,* 2011, ***115***, 25132–25137.

[51] J. Xu, J. Li, Y. Zhu, K. Zhu, Y. Liu, and J. Liu, *RSC Adv.,* 2016, ***6***, 20343–20348.

[52] F. Croce, G. Appetecchi, L. Persi, and B. Scrosati, *Nature,* 1998, ***394***, 456–458.

[53] Y. Aihara, G. Appetecchi, and B. Scrosati, *J. Electrochem. Soc.,* 2002, 149, A849-A854.

[54] S. Zhang, *J. Electrochem. Soc.,* 2013, ***160***, A1421-A1424.

[55] Y. Lin, X. Wang, J. Liu, and J. Miller, *Nano Energy,* 2017, ***31***, 478–485.

[56] S. Choudhury, R. Mangal, A. Agrawal, and L. Archer, *Nat. Commun.,* 2015, ***6***, 10101–10109.

[57] M.B. Berman, and S. Greenbaum, *Membranes,* 2015, ***5***, 915–923.

[58] X. Ji, S. Evers, R. Black, and L. Nazar, *Nat. Commun.,* 2011, ***2***, 1–7.

[59] Y. Zhao, Y. Zhang, D. Gosselink, T. Doan, M. Sadhu, H. J. Cheang, and P. Chen, *Membranes,* 2012, ***2***, 553–564.

[60] S. Choudhury, T. Saha, K. Naskar, M. Stamm, G. Heinrich, and A. Das, *Polymer,* 2017, ***112***, 447–456.

[61] B. Kurc, and T. Jesionowski, *J. Solid State Electrochem.,* 2015, ***19***, 1427–1435.

[62] S. Park, Y. Lee, and D. Kim, *J. Electrochem. Soc.,* 2015, ***162***, A3071-A3076.

[63] S. Ju, Y. Lee, Y. Sun, and D. Kim, *J. Mater. Chem. A,* 2013, ***1***, 395–401.

[64] L. Jin, H. Wu, and M. Morbidelli, *Nanomaterials,* 2015, ***5***, 1454–1468.

[65] M. Chaimberg, and Y. Cohen, *J. Colloid Interface Sci.,* 1990, ***134***, 576–579.

[66] M. Iijima, M. Kobayakawa, and H. Kamiya, J. *Colloid Interface Sci.,* 2009, ***337***, 61–65.

[67] M. Patel, R. Demir-Cakan, M. Morcrette, J. Tarascon, M. Gaberscek, and R. Dominko, *ChemSusChem,* 2013, ***6***, 1177–1181.

[68] N. Deng, W. Kang, Y. Liu, J. Ju, D. Wu, L. Li, B. Hassan, and B. Cheng, *J. Power Sources,* 2016, ***331***, 132–155.

[69] L. Yang, G. Li, X. Jiang, T. Zhang, H. Lin, and J. Lee, *J. Mater. Chem. A*, 2017, ***5***, 2506-12512.

[70] X. Zhou, Q. Liao, T. Bai, and J. Yang, *J. Electroanal. Chem*., 2017, ***791***, 167–174.

[71] P. Zuo, J. Hua, M. He, H. Zhang, Z. Qian, Y. Ma, C. Du, X. Cheng, Y. Gao, and G. Yin, *J. Mater. Chem. A*, 2017, ***5***, 10936–10945.

[72] Y. Lu, S. Gu, J. Guo, K. Rui, C. Chen, S. Zhang, J. Jin, J. Yang, and Z. Wen, *ACS Appl. Mater. Interfaces,* 2017, ***9***, 14878–14888.

[73] C. Oh, N. Yoon, J. Choi, Y. Choi, S. Ahn, and J. Lee, *J. Mater. Chem. A,* 2017, ***5***, 5750–5760.

[74] G. Zhou, L. Li, D. Wang, X. Shan, S. Pei, F. Li, and H. Cheng, *Adv. Mater.* 2015, ***27***, 641–647.

[75] Y. Jiang, F. Chen, Y. Gao, Y. Wang, S. Wang, Q. Gao, Z. Jiao, B. Zhao, and Z. Chen, *J. Power Sources,* 2017, ***342***, 929–938.

[76] S. Abbas, M. Ibrahem, L. Hu, C. Lin, J. Fang, K. Boopathi, P. Wang, L. Li, and C. Chu *J. Mater. Chem. A,* 2016, ***4***, 9661–9669.

[77] Y. Cui, and Y. Fu, *J. Power Sources,* 2015, ***286***, 557–560.

[78] L. Kong, X. Chen, B.Q. Li, H.J. Peng, J.Q. Huang, J. Xie, Q. Zhang, *Adv. Mate.* 2018, ***30***, 1705219.

[79] Y. Chen, S.H. Choi, D.W. Su, X.C. Gao, G.X. Wang, *Nano Energy* 2018, ***47***, 331.

[80] M. Li, Y.N. Zhang, X.L. Wang, W. Ahn, G.P. Jiang, K. Feng, G. Lui, Z.W. Chen, *Adv. Funct. Mater.* 2016, ***26***, 8408.

[81] X.W. Wang, T. Gao, F.D. Han, Z.H. Ma, Z. Zhang, J. Li, C.S. Wang, *Nano Energy* 2016, ***30***, 700.

[82] H. Pan, Z.B. Cheng, Z.B. Xiao, X.J. Li, R.H. Wang, *Adv. Funct. Mater.* 2017, ***27***, 1703936.

[83] Z.C. Xiao, D.B. Kong, Q. Song, S.K. Zhou, Y.B. Zhang, A. Badshah, J.X. Liang, L.J. Zhi, *Nano Energy,* 2018, ***46***, 365.

[84] L.C. Yin, J. Liang, G.M. Zhou, F. Li, R. Saito, H.M. Cheng, *Nano Energy* 2016, ***25***, 203.

[85] M.W. Xiang, H. Wu, H. Liu, J. Huang, Y.F. Zheng, L. Yang, P. Jing, Y. Zhang, S.X. Dou, H.K.

Liu, *Adv. Funct. Mater.*, 2017, ***27***, 1702573.

[86] E. Cha, M.D. Patel, J. Park, J. Hwang, V. Prasad, K. Cho, W. Choi, *Nat. Nanotechnol.,* 2018 ***13***, 337.

[87] X.Q. Zhang, B. He, W.C. Li, A.H. Lu, *Nano Res.* 2018, ***11***, 1238.

[88] G.X. Li, Q.Q. Huang, X. He, Y. Gao, D.W. Wang, S.H. Kim, D.H. Wang, *ACS Nano* 2018, ***12***, 1500.

[89] G. Li, X.L. Wang, M.H. Seo, M. Li, L. Ma, Y.F. Yuan, T.P. Wu, A.P. Yu, S. Wang, J. Lu, Z.W. Chen, *Nat. Commun.,* 2018, ***9***, 705.

[90] H.W. Du, X.C. Gui, R.L. Yang, Z.Q. Lin, B.H. Liang, W.J. Chen, Y.J. Zheng, H. Zhu, J. Chen, *Nanoscale*, 2018, ***10***, 3877.

[91] J.Y. Wang, J.W. Wan, N.L. Yang, Q. Li, D. Wang, *Nat. Rev. Chem.*, 2020, ***4***, 159.

[92] C. Wang, J.Y. Wang, W.P. Hu, D. Wang, *Chem. Res. Chinese U.* 2020, ***36***, 68.

[93] X. Huang, J.Y. Tang, B. Luo, R. Knibbe, T. Lin, H. Hu, M. Rana, Y. Hu, X. Zhu, Q. Gu, D. Wang, L. Wang, *Adv. Energy Mater.,* 2019, ***9***, 1901872.

[94] J. Wang, J. Wan, D. Wang, *Acc. Chem. Res.,* 2019, ***52***, 2169.

[95] E. Salhabi, J. Zhao, J. Wang, M. Yang, B. Wang, D. Wang, *Angew. Chem. Int. Ed.*, 2019, ***58***, 9078.

[96] D. Mao, J. Wan, J. Wang, D. Wang, *Adv. Mater.,* 2018, ***31***, 1802874.

[97] J. Wang, Y. Cui, D. Wang, *Adv. Mater.,* 2018, ***31***, 1801993.

[98] Y. Liu, G. Li, Z. Chen, X. Peng, *Nanoscale,* 2017, ***5***, 9775.

[99] L. Zhu, H.J. Peng, J. Liang, J.Q. Huang, C.-M. Chen, X. Guo, W. Zhu, P. Li, Q. Zhang, *Nano Energy,* 2015, ***11***, 746.

[100] S.Z. Huang, L.L. Zhang, J.Y. Wang, J.L. Zhu, P.K. Shen, *Nano Res.,* 2018, ***11***, 1731.

[101] Y. Yang, X. Song, X.J. Li, Z.Y. Chen, C. Zhou, Q.F. Zhou, Y. Chen, *Adv. Mater.,* 2018, ***30***, 1706539.

[102] W.L. Wu, J. Pu, J. Wang, Z.H. Shen, H.Y. Tang, Z.T. Deng, X.Y. Tao, F. Pan, H.G. Zhang, *Adv. Energy Mater.,* 2018, 1702373.

[103] G. Ai, Y.L. Dai, W.F. Mao, H. Zhao, Y.B. Fu, X.Y. Song, Y.F. En, V. Battaglia, V. Srinivasan, G. Liu, *Nano Letters*, 2016, ***16***, 5365.

[104] X.Y. Tao, JT. Zhang, Y. Xia, H. Huang, J. Du, H. Xiao, W.K. Zhang, Y.P. Gan, *J. Mater. Chem. A,* 2014, ***2***, 2283.

[105] D. Su, M. Cortie, G. Wang, *Adv. Energy Mater.*, 2017, ***7***, 1602014.

[106] J.L. Wang, Z. Meng, W.T. Yang, *ACS Appl. Mater. Inter.*, 2019, ***11***, 819.

[107] H.L. Wu, Y. Li, R. Ren, D.W. Rao, Q.J. Zheng, L. Zhou, D.M. Lin, *Nano Energy,* 2019, ***55***, 82.

[108] P. Coquay, A. Peigney, E. De Grave, E. Flahaut, R.E. Vandenberghe, C. Laurent, *J. Phys. Chem. B*, 2005, ***109***, 17813.

[109] D.R. Minett, J.P. O'Byrne, S.I. Pascu, P.K. Plucinski, R.E. Owen, M.D. Jones, D. Mattia, *Catal. Sci. Techno.,* 2014, ***4***, 3351.

[110] X. Tuaev, J. Paraknowitsch, R. Illgen, A. Thomas, P. Strasser, *Phys. Chem. Chem. Phys.*, 2012, ***14***, 6444.

[111] H.T. Tang, J.L. Yang, G.X. Zhang, C.K. Liu, H. Wang, Q.H. Zhao, J.T. Hu, Y.D. Duan, F. Pan, *Nanoscale*, 2018, ***10***, 386.

[112] Y. Zhong, X.H. Xia, S.J. Deng, J.Y. Zhan, R.Y. Fang, Y. Xia, X.L. Wang, Q. Zhang, J.P. Tu, *Adv. Energy Mater.,* 2018, ***8***, 1701110.

[113] Y. Luo, T.Y. Yang, Q. Zhao, M.Z. Zhang, *J. Alloy Compd.,* 2017, ***30***, 64.

[114] J.B. Luo, M.J. Wan, J.W. Cui, B.G. Peng, X.Y. Zhang, Y. Zhang, Y. Wang, Y.Q. Qin, H.M. Zheng, Y.C. Wu, *Mater. Lett.,* 2017, ***188***, 275

[115] I. Kosacki, T. Suzuki, H. Anderson, P. Colomban, *Solid State Iionics*, 2002, ***149***, 99.

[116] B. Zhang, S. Zhou, H. Wang, Z. Du, *Chin. Sci. Bull.,* 2008, ***53***, 1639.

[117] D. Xiao, C. Lu, C. Chen, S. Yuan, *Energy Stor. Mate.,* 2018, ***10***, 216.

[118] L. Ma, R. Chen, G. Zhu, Y. Hu, Y. Wang, T. Chen, J. Liu, Z. Jin, *ACS Nano,* 2017, ***11***, 7274.

[119] X. Hong, J. Jin, T. Wu, Y. Lu, S. Zhang, C. Chen, Z. Wen, *J. Mater. Chem., A* 2017, ***5***, 14775.

[120] Y. Lu, S. Gu, X. Hong, K. Rui, X. Huang, J. Jin, C. Chen, J. Yang, Z. Wen, *Energy Stor. Mater.* 2018, **11**, 16.

[121] J. Wang, T. Wu, S. Zhang, S. Gu, J. Jin, Z. Wen, *Chem. Eng. J.,* 2018, ***334***, 2356.

[122] Q. Pang, J. Tang, H. Huang, X. Liang, C. Hart, K.C. Tam, L.F. Nazar, *Adv. Mater.*, 2015, ***27***, 6021.

[123] S. Boursiquot, M. Mullet, J.J. Ehrhardt, *Surf. Interface Anal.*, 2002, ***34***, 293.

[124] M. Lacey, A. Yalamanchili, J. Maibach, C. Tengstedt, K. Edstom, D. Brandell, *RSC Advances*, 2016, ***6***, 3632.

[125] H. Chu, H. Noh, Y. Kim, S. Yuk, J. Lee, J. Lee, H. Kwack, Y. Kim, D. Yang, H. Kim, , *Nat. Commun.*, 2019, ***10***, 188-201.

[126] L.B. Ma, R. Chen, G. Zhu, Y. Hu, Y. Wang, T. Chen, J. Liu, Z. Jin, *ACS Nano*, 2017, ***11***, 7274.

References

[127] C. Yang, Y. Yin, S. Zhang, N. Li, Y. Guo. *Nat. Commun.,* 2015, ***6***, 8058.

[128] D. Lin, Y. Liu, Y. Cui, *Nat. Nanotech.,* 2017, ***12***, 194-206.

[129] C. C. Fang, J.X. Li, M.H. Zhang, Y.H. Zhang, F. Yang, J.Z. Lee, M.H. Lee, J. Alvarado, M. A. Schroeder, Y. Yang, B. Lu, N. Williams, M. Ceja, L. Yang, M. Cai, J. Gu, K. Xu, X. Wang, Y.S. Meng, *Nature,* 2019, ***572***, 511-515.

[130] P. Bai, J. Li, F. Brushett, M. Bazant, *Energy Environ. Sci.,* 2016, ***9***, 3221-3229.

[131] W. Zhang, H. Zhuang, L. Fan, L. Gao, Y. Lu, *Sci. Adv.,* 2018, **4**, eaar4410.

[132] Z. Ju, J. Nai, Y. Wang, T. Liu, J. Zheng, H. Yuan, O. Sheng, C. Jin, W. Zhang, Z. Jin, H. Tian, Y. Liu, X. Tao, *Nat. Commun.,* 2020, ***11***, 488.

[133] G. Zheng, S. Lee, Z. Liang, H. Lee, K. Yan, H. Yao, H. Wang, W. Li, S. Chu, Y. Cui, *Nat. Nanotech.* 2014, ***9***, 618-623.

[134] D. Liu, Y. Liu, Z. Liang, H. Lee, J. Sun, H. Wang, K. Yan, J. Xie, Y. Cui, *Nat. Nanotech.* 2016, ***11***, 626-632.

[135] N. Li, Y. Yin, C. Yang, Y. Guo, *Adv. Mater.* 2016, ***9***, 1853-1858.

[136] X. Cao, X. Ren, L. Zou, M. Engelhard, W. Huang, H. Wang, B. Matthews, H. Lee, C. Niu, B. Arey, Y. Cui, C. Wang, J. Xiao, J. Liu, W. Xu, J. Zhang, *Nat. Energy* 2019, ***4***, 796-805.

[137] R. Zhao, X. Chen, W. Ma, J. Zhang, J. Guo, X. Zhong, J. Yao, J. Sun, J. Rubinfien, X. Zhou, J. Wang, *Nature,* 2020, ***577***, 416-420.

[138] D. Staelin. 6.013 *Electromagnetics and Applications*. Spring 2009. Massachusetts Institute of Technology: MIT OpenCourseWare.

[139] H. Yin, S. Ai, J. Xu, W. Shi, L. Zhu, *J. Electroanal. Chem.* 2009, ***637***, 21-27.

[140] Y. Cheng, L. Koh, D. Li, B. Ji, Y. Zhang, J. Yeo, G. Guan, M. Han, Y. Zhang, *ACS Appl. Mater. Interfaces* 2015, ***7***, 21787-21796.

[141] R. Pereira, R. Pereira, R. Goncalves, M. Silva, C. Costa, M. Silva, V. Bermudez, S. Mendez, Silk

Fibroin Separators: *ACS Appl. Mater. Interfaces* ***10***, 5385-5394 (2018).

[142] M. Mahmoudi, I. Lynch, M. Ejtehadi, M. Monopoli, F. Bombelli and S. Laurent, *Chem. Rev.* 2011, ***111***, 5610-5637.

[143] Y. Yang, Z. Shao, X. Chen, P. Zhou, *Biomacromolecules* 2004, ***5***, 773-779.

[144] A. Matsumoto, J. Chen, A. Collette, U. Kim, G. Atman, P. Cebe, D. Kplan, *J. Phys. Chem*. *B,* 2006, ***110***, 21630-21638.

[145] H. Shulha, C. Foo, D. Kaplan, V. Tsukruk, *Polymer **47***, 5821-5830 2006.

[146] Q. Lu, H. Zhu, C. Zhang, F. Zhang, B. Zhang, D. Kaplan, *Biomacromolecules* 2012, ***13***, 826-832 ().

[147] C. Rusa, C. Bridges, S. Ha, A. Tonelli, *Macromolecules* 2005, **38**, 5640-5646.

[148] N. J. Greenfield, *Nat. Protoc.,* 2006, ***1***, 2876-2890.

[149] G. Wang, J. Yang, J. Park, X. Gou, B. Wang, H. Liu, J. Yao, *J. Phys. Chem. C* 2008, **112**, 8192-8195.

[150] S. Ling, Z. Qi, D. Knight, Z. Shao, X. Chen, *Polym. Chem.* 2013, **4**, 5401-5406.

[151] K. Yamada, Y. Tsuboi, A. Itaya, *Thin Solid Films* 2003, **440**, 208-216.

[152] C. Cheng, Y. Yang, X. Chen, Z. Shao, *Chem. Commun.* 2008, 5511-5513.

[153] A. Nel, L. Madler, D. Velegol, T. Xia, E. Hoek, P. Somasundaran, F. Klaessig, V. Castrasova, M. Thompson, *Nat. Mater.* 2009, ***8***, 543-557.

[154] E. Hoek, G. Agarwal, *J. Colloid Interf. Sci.* 2006, ***298***, 50-58.

[155] R. Ismaiilova, S. Alieva, *Surf. Eng. Appl. Electrochem.* 2007, ***43***, 462-464.

[156] Q. Zhang, Y. Lu, L. Miao, Q. Zhao, K. Zhao, K. Xia, J. Liang, S. Chou, J. Chen, *Ange. Chem. Int. Ed.* 2018, ***57***, 14796-14800.

[157] X. Liang, Q. Pang, I. Kochetkov, M. Sepere, H. Huang, X. Sun, L. Nazar, *Nat. Energy* 2017, ***2***, 17119.

[158] J. Qian, W. Henderson, W. Xu, P. Bhattacharya, M. Engelhard, O. Borodin, J. Zhang, *Nat. Commun.* 2015, **6**, 6362.

[159] Y. Li, Y. Li, A. Pei, K. Yan, Y. Sun, C. Wu, L. Joubert, R. Chin, A. Koh, Y. Yu, J. Perrino, B. Butz, S. Chu, Y. Cui, *Science* 2017, ***358***, 506-510.

[160] W. Huang, J. Wang, M. Braun, Z. Zhang, Y. Li, D. Boyle, P. Mclntyre, Y. Cui, *Matter* 2019, ***1***, 1232-1245.

[161] D. Zhang, S. Wang, B. Li, Y. Gong, S. Yang, *Adv. Mater.* 2019, **31**, 1901820.

[162] K. Yan, J. Wang, S. Zhao, D. Zhou, B. Sun, Y. Cui, G. Wang, *Ange. Chem. Int. Ed.* 2019, ***58***, 11364-11368.

[163] M. Ebadi, M. Lacey, D. Brandell, C. Araujo, *J. Phys. Chem. C,* 2017, ***121***, 23324-23332.

[164] Y. Shen, A. Oganov, G. Qian, J. Zhang, H. Dong, Q. Zhu, Z. Zhou, *Sci. Rep.* 2015, ***5***, 14204.

[165] P. Albertus, S. Babinec, S. Litzelman, A. Newman, *Nat. Energy,* 2018, ***3***, 16-21.

[166] R. Pathak, K. Chen, A. Gurung, K. Reza, B. Bahrami, F. Wu, A. Chaudhary, N. Ghimire, B. Zhou, W. Zhang, Y. Zhou, Q. Qiao, *Adv. Energy Mater.* 2019, ***9***, 1901486.

[167] R. Pathak, K. Chen, A. Gurung, K. Reza, B. Bahrami, J. Pokharel, A. Baniya, W. He, F. Wu, Y. Zhou, K. Xu, Q. Qiao, *Nat. Commun.* 2020, **11**, 93.